ORGANOSILANE ADSORPTION ON LIGHT METAL ALLOYS

by

TAE KYONG JOHN KIM

B.Sc., The University of British Columbia, 2000

A THESIS SUBMITTED IN PARTIAL FULFILLMENT OF
THE REQUIREMENT FOR THE DEGREE OF

DOCTOR OF PHILOSOPHY

in

THE FACULTY OF GRADUATE STUDIES

(Chemistry)

UNIVERSITY OF BRITISH COLUMBIA

April 2006

Abstract

This thesis discusses research on the adhesive bonding of organosilanes to alloys of Al and Mg using surface analysis techniques (especially secondary-ion mass spectrometry (SIMS), X-ray photoelectron spectroscopy (XPS) and scanning electron microscopy (SEM)). One project involved comparing the adsorption of bis-1,2-(triethoxysilyl)ethane (BTSE) on high-purity Al, and on anodized 7075-Al alloy, for different pre-treatments involving chemical and heating procedures, and exposure to a H_2 plasma. The objectives were to assess the effects of these pre-treatments on the direct Al-O-Si covalent bonding and the strength of the adhesive coating.

The separate adsorption of BTSE and γ-glycidoxypropyltrimethoxysilane (γ-GPS) on an air-oxidized mirror-polished 7075-Al surface was studied with an emphasis on the different microstructural regions of the alloy surface with scanning Auger microscopy (SAM). BTSE at its natural pH (4.3) adsorbed on the Al-Cu-Mg and Al-Fe-Zn types of second-phase particles, and on the alloy matrix, while γ-GPS adsorbed on all these regions only after the starting pH was reduced from its natural value (5.7) to 3.2. However, with prior heating of the sample (200°C, 15 min), γ-GPS adsorption occurred on all regions even at pH 5.7. Time-of-flight (TOF)-SIMS was used for the first time to indicate the nature of the metal-O-Si bonding at the different micro-regions.

The Mg-based alloy AZ91 was characterized with regard to its different surface micro-regions both from mirror-polished and fractured surfaces, as well as oxide growth and oxide stability on heating. There is a clear tendency for Mg oxidation, which covers the Al component, while other elements (Zn and Mn) are detected only with bulk

characterization methods, although localized Mn-rich particles (dimensions ~3 µm) are identified by SEM and energy-dispersive X-ray (EDX) spectroscopy. In a coating environment (by 1% solutions of BTSE, γ-GPS, γ-APS at their natural pH values) the Mg oxide is etched, and adsorption occurs on the different regions of the alloy, but the attachment is weak, especially because of the fragile nature of the underlying substrate. However 4% BTSE (at pH 3.9) formed a thicker and denser coating with better prospects for substrate protection.

Table of Contents

List of Tables

List of Figures

List of Acronyms

γ-APS	γ-aminopropyltriethoxysilane
γ-GPS	γ-glycidoxypropyltrimethoxysilane
ADC	analog-to-digital converter
AES	Auger electron spectroscopy
BSD	backscattered electron detector
BTSE	bis-1,2-(triethoxysilyl) ethane
CAE	constant analyzer energy
CHA	concentric hemispherical analyzer
CRR	constant retarding ratio
EDX	energy dispersive X-ray spectroscopy
FPL	Forest Products Laboratory
FWHM	full-width-at-half-maximum
MCP	multichannel plate
SAM	scanning Auger microscopy
SED	secondary electron detector
SEM	scanning electron microscopy
SIMS	secondary ion mass spectrometry
TOF	time-of-flight
UHV	ultrahigh vacuum
XPS	X-ray photoelectron spectroscopy

Acknowledgements

I would like to thank my supervisor, Professor K.A.R. Mitchell, who introduced me to surface science. I am grateful for his advice and guidance throughout the period of the research as well as his time for careful reading of this thesis.

I thank Dr. P.C. Wong and Dr. K.C. Wong for teaching me about SAM and XPS measurements, and for having many helpful discussions with me. As well, I would like to thank Ms. M. Mager for assistance in EDX measurements and interpretation, and Dr. R.N.S Sodhi (University of Toronto) for introducing me to the TOF-SIMS technique. Also I thank Professor J. Metson (University of Auckland) for discussions on the AZ91-Mg alloy.

During my research, I have greatly appreciated interactions with other members of the group (present and former), including Dr. D. Susac, Dr. L. Zhu, Dr. X. Sun, Dr. S. Kulinich, Dr. M. Saidy, Dr. M. Kono, Mr. M. Teo, Ms. A. Ahktar, Ms. R. Li, and Mr. W-H. Kok. I also acknowledge the efforts of staff in the Departmental Mechanical and Electronics shops for keeping the equipments in working order for this research.

Finally, I would like to thank my family and my friends for their support and encouragement during these years of my studies.

Chapter 1 Introduction

1.1 Light Metal Alloys

1.1.1 Al Alloys

Light metals are widely used in our daily lives and examples extend from small items such as cellular phones and packing cans, to much larger-scale products like automobiles and airplanes. Aluminum and magnesium have wide importance, in part because of their natural abundance. Aluminum is extracted from the mineral bauxite (hydrated Al oxide) by an electrolytic process [1, 2]. One of the main advantages is its low density (2.7 gcm^{-3}) compared with the heavier metals like steel (7.8 gcm^{-3}); also aluminum is an excellent conductor of heat and electricity, and is non-toxic. Furthermore, aluminum has resistance to corrosion under moderate service conditions, due to the thin oxide film that forms when it is exposed to the atmosphere [1-3].

High-purity aluminum is a soft material, but its mechanical strength can be increased when additional constituents are added to form an alloy. The chief alloying elements added to aluminum are Cu, Mg, Si, Mn, and Zn [1-3], and there is a basic nomenclature based on the main alloying element added [1-3]. For example, the 7xxx (e.g. 7075-Al) and 2xxx (e.g. 2024-Al) series alloys have Zn and Cu as the main alloying elements respectively. The addition of the alloying constituents in varying amounts is not only important for increasing strength, but also for improving the castability of the metal. Copper is one of the most important additions to aluminum as it provides a substantial strengthening effect through age-hardening, but it also has a deleterious effect on the corrosion resistance. Zinc is added (with magnesium) to produce heat-treatable alloys and

for providing a further strengthening of the aluminum [3]. Magnesium improves strength and weldability, while alloying with silicon lowers the melting point and increases the metal's fluidity.

When the alloying elements are added to aluminum, various phases can be formed depending on the temperature and the amount added. Figure 1.1 shows the phase diagram for the Al-Zn system where the phase with composition of ZnAl is stable at temperatures higher than 550 K, and when the amount of zinc exceeds 32 wt% [4]. Below 550 K, there is a two-phase region with Al-rich and Zn-rich phases, each of which represents a solid solution (e.g. with Al atomic sites occupied by Zn atoms). The phases that precipitate out on cooling are intermetallic compounds (or second-phase particles) and they may be dispersed within the main solid solution (alloy matrix). The addition of a third element, magnesium, to the Al-Zn system will lead to an even greater number of phases. Figure 1.2 shows the Al corner of the Al-Zn-Mg phase diagram where the stable phases are indicated for different temperatures. It shows that $Mg_3Zn_3Al_2$, and other intermetallic compounds can be stable depending on the amounts of zinc and magnesium added to the aluminum.

Although there can be differences depending on the details of the material processing, the second-phase particles contribute to the underlying microstructure of a material. Figure 1.3 shows a scanning electron micrograph of some second-phase particles for a mirror-polished 7075-Al alloy surface. These particles exist in various chemical composition, size and shape. For the 7075-Al alloy, Al_2CuMg, Al_3Fe, Mg_2Al_3 phases have been reported [5-8]. The Al_2CuMg phase has been called the S-phase and the variants of it are designated as the Al-Cu-Mg phase [5-8]. The particle size can vary from
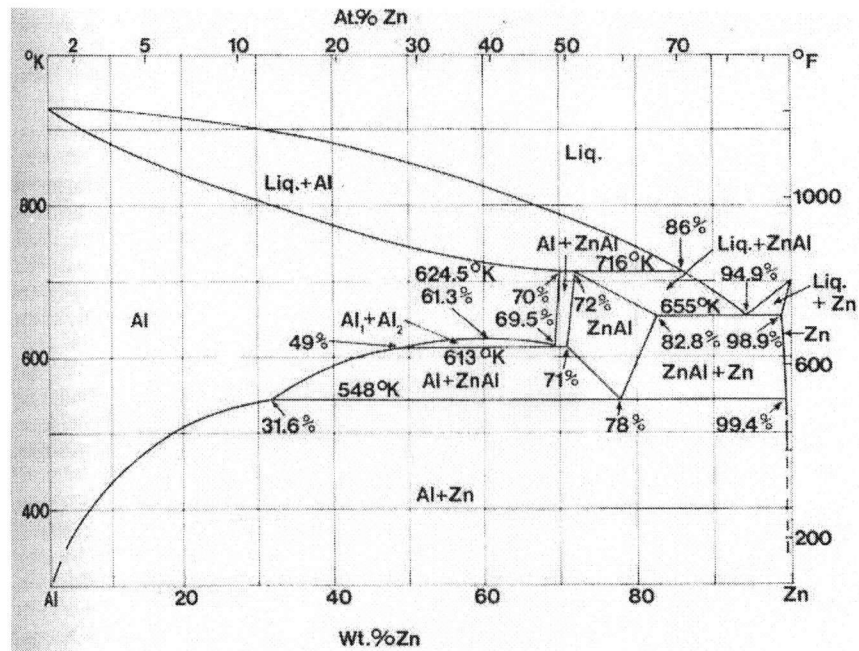
Figure 1.1. The Al-Zn system phase diagram [4].
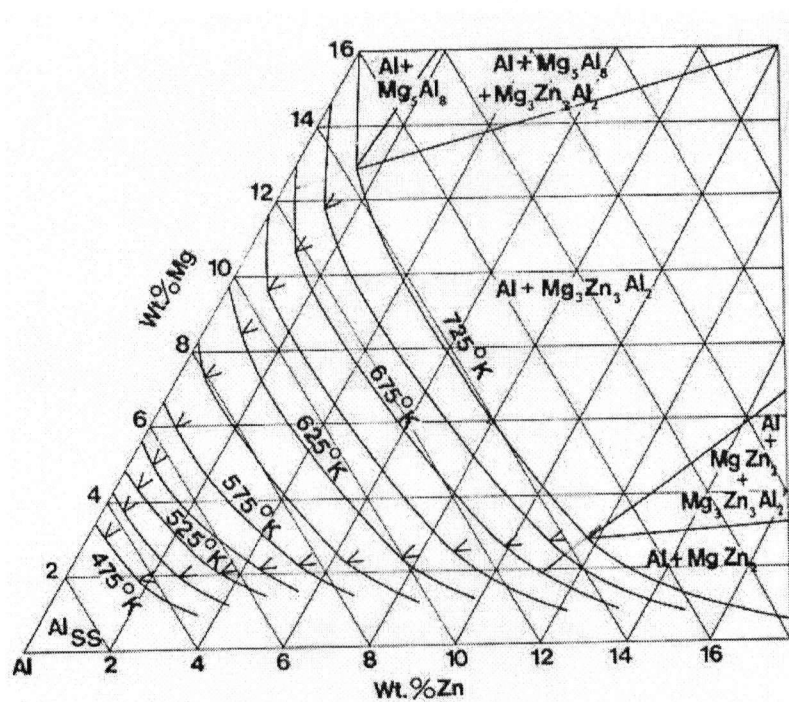
Figure 1.2. Al-Zn-Mg system phase diagram (partial) [4].
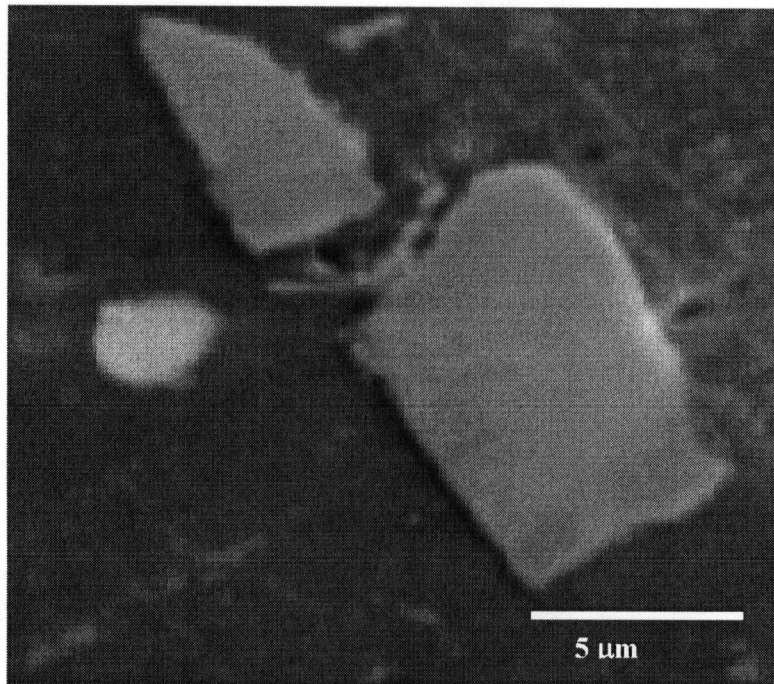
Figure 1.3. Scanning electron micrograph of a mirror-polished 7075-Al alloy surface.

1 to 20 µm; most are irregular-shaped although round-shaped particles can also be present [5, 8, 9, 10]. The material processing aims to control the distribution of the second-phase particles in order to control the mechanical properties of the alloy. This is very useful in practice, but the additions also make the alloy more susceptible to corrosion due to galvanic coupling. Galvanic coupling occurs when two metallic materials are in electrical contact so that the more noble metal becomes cathodic with respect to the other [11]. Thus when aluminum is in contact with a nobler metal such as copper in a conducting environment, corrosion of the former can occur. More generally the second-phase particles lead to chemical heterogeneities for the alloys.

Aluminum alloys are divided into two major categories: cast and wrought. In the casting process, a totally molten metal is poured into a mold cavity having the desired shape and the metal solidifies on cooling. Cast alloys are relatively brittle alloys, and after formation it is not possible to further work them by appreciable deformation. On the other hand, the wrought alloys are relatively ductile and amenable to either cold or hot working during fabrication [1, 11]. Cold working involves altering the shape or the size of the metal by such processes as rolling and drawing, and although no heating is applied, the alloy material may reach temperatures up to 150°C during the process [1]. Hardness and tensile strength are increased with cold working whilst ductility decreases. Hot working involves applying direct heat and Al alloys containing Zn, Cu, and Mg are heat treatable. The heat treatment involves three steps: the first involves heating (typically around 350°C to 530°C for 30 min), then the alloy is quenched to room temperature and this is followed by an aging process (e.g. at 120°C for 24 hours) [12]. The growth of second-phase particles in the aging process contributes to the increase in alloy strength.

In the work presented in this thesis, the 7075-T6 Al alloy has been used. The actual approximate minority components for the Al alloy used are: 6 wt% Zn, 3 wt% Mg, 2 wt% Cu, 0.5 wt% Fe, 0.4 wt% Si, 0.3 wt% Mn and 0.2 wt% Ti. The temper designation, T6, represents an alloy that has been heat treated in solution and then artificially aged [12]. Variations in solution heat treatment time (15 min to 24 hours), as well as temperature (400°C to 500°C) have been reported [5, 9, 13-16]. Among alloys in the 7xxx series, the 7075-Al alloys has been used most extensively and for the longest time [1]. It is used for aerospace and other applications that require the highest strength [2].

1.1.2 Mg Alloys

Magnesium is abundant in the earth's crust and in seawater, and currently, the metal is produced by electrolysis of the fused anhydrous chloride ($MgCl_2$) derived from magnesite ($MgCO_3$) or seawater [17, 18]. Magnesium is one of the competing metals for lightweight construction with aluminum since its density of 1.8 gcm^{-3} is the lowest of all structural materials. This is one advantage that magnesium has over aluminum and the former is especially attractive for the automotive industry. Since the early 1970's, this industry has aimed to minimize vehicle weight in order to reduce operation cost, as well as exhaust emissions. The second advantage of magnesium is that it has an excellent machinability due to its lower resistance to cutting (about half that of Al), and as a result Mg can be machined up to five times faster than Al [19].

However, although Mg and its alloys are potentially attractive, to date they have found limited application due largely to high reactivity in aqueous environment and hence they are susceptible to corrosion. So far, Mg has been limited to applications where

6

it is not exposed to a wet atmosphere (e.g. for internal parts like car seats and dashboards). In addition Mg has other disadvantages when compared to Al, including poor cold workability, lower thermal and electrical conductivities, and lower tensile strength [17, 19].

For Mg, there are bigger restrictions on the possible alloying constituents, particularly since Mg has a low reduction potential, and thus has a high tendency to suffer from galvanic corrosion. Aluminum is the element that gives the most favorable effect when added to magnesium; Al improves strength and hardness, and makes the alloy easier to cast. However, the amount of Al that can be added is limited as the ductility decreases rapidly as the Al content is increased above 8 wt%. Zn is the next most effective element for alloying with magnesium; it is often used in combination with Al to improve the room-temperature strength. The amount of Zn is also limited to the 1 to 3 wt% range especially because it accelerates corrosion [17, 19]. Manganese acts in the opposite way to magnesium by improving the corrosion resistance; the mechanism involves combining with iron and other heavy-metal elements to form relatively harmless intermetallic compounds [17, 19].

Magnesium alloys can also be divided into the casting and wrought forms. To date the manufacturing process for most Mg alloy components are produced by die casting [19], and as a result this form has dominated over the wrought forms [17, 19]. Die casting is a process where the liquid metal is forced into a mold under pressure, and is allowed to solidify while the pressure is maintained [11]. Al alloys can also be die casted, but this process dominates for making Mg alloys because of its lower specific heat per unit volume compared to that of Al. This allows Mg castings to cool quicker, and in turn

allows for faster cycle times and a reduction in die wear. Iron in the dies has very low solubility in liquid Mg alloys and this reduces the sticking tendency encountered with Al. Dies for casting Mg alloys last two to three times longer than those for Al alloys [17, 19].

One of the most widely used Mg alloys is designated AZ91, and this alloy was chosen for a study discussed in this thesis. The "AZ" notation refers to the Mg alloy having Al and Zn contents respectively, and numerals "91" indicate their weight percentages (9% Al and 1% Zn). The AZ91-Mg alloy also contains a minor amount of Mn (0.3%). This alloy is produced at low cost and is used where moderate strength and low operational temperatures are needed. Its applications include in the aircraft controls, transmission housing, automobile parts and portable electronic appliance parts [17, 19]. One of the disadvantages of the AZ91-Mg alloy is that in ambient conditions, it is limited to a maximum service temperature of 120°C, as at higher temperatures the mechanical quality falls rapidly. The AZ91-Mg alloy demonstrates significant phase segregation effects as well, in particular the separation of the β-phase ($Mg_{17}Al_{12}$ sometimes referred to as Mg_4Al_3) [19]. The phase diagram for the Mg-Al system is shown in Figure 1.4 where the $Mg_{17}Al_{12}$ phase is indicated [20], and the scanning electron micrograph of a mirror-polished surface is shown in Figure 1.5 where the β-phase is seen as the lighter regions.

Due to the limitations noted for the AZ91 alloy, other Mg alloys have been produced with reduced amounts of Al and Zn contents. An example of such an alloy is the AM series (Al and Mn contents) which are now used extensively for automotive safety components (e.g. panel supports, steering wheel armatures, and seat parts). AM60 is an example of such alloy, and it has the elemental weight compositions of 6 wt% Al
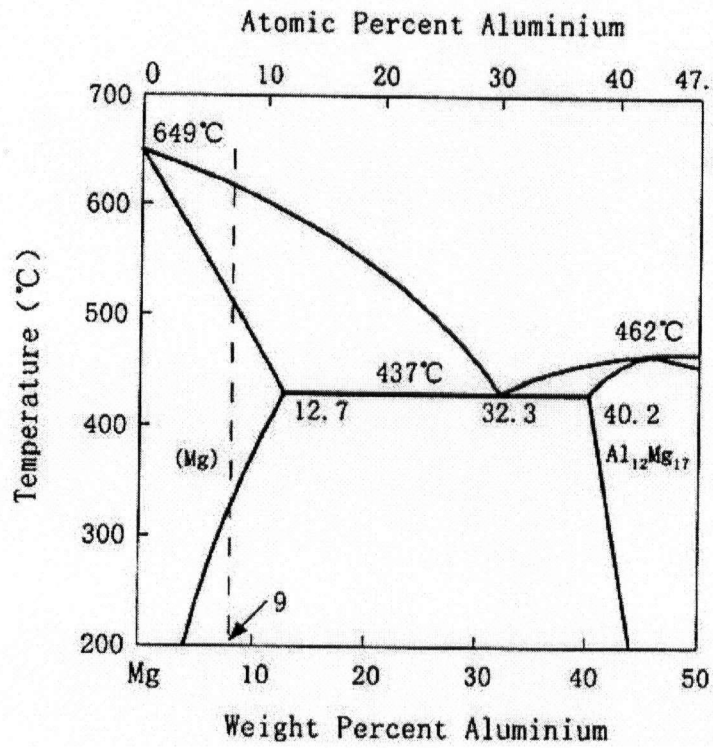
Figure 1.4. Mg-Al system phase diagram (partial) [20].
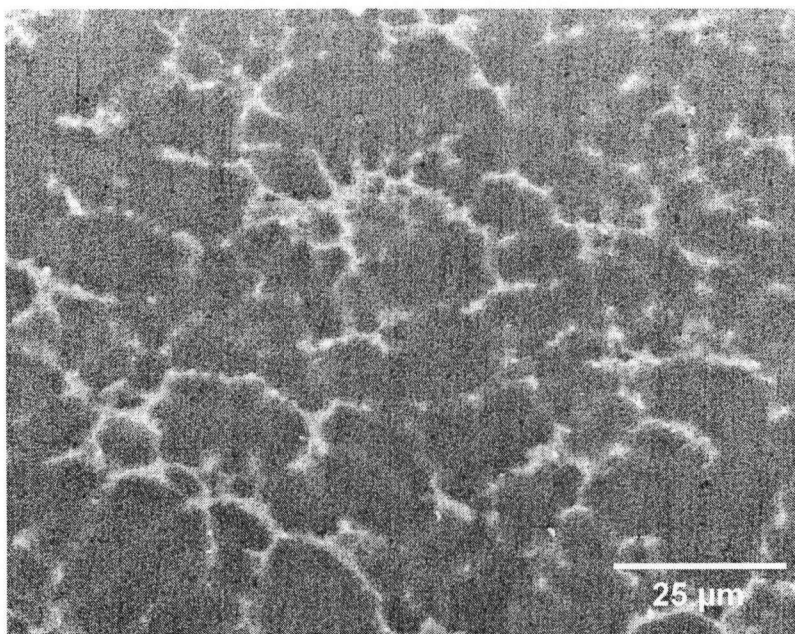
Figure 1.5. SEM micrograph of mirror polished AZ91-Mg alloy surface.

and less than 1 wt% Mn. The AM series alloys also include additions of Ag and Si. They have better characteristics at higher temperature than AZ91-Mg alloy, but have higher production costs. In addition, the castability of the AM alloys diminishes as the Al content reduces [19].

1.1.3 Passivation of Reactive Alloys

Both aluminum and magnesium are reactive metals. In the case of aluminum, it develops an oxide film that protects from corrosion in many environments. This film is quite stable in neutral and many acidic solutions, and even if the oxide is scraped away in air, the exposed metal rapidly forms another oxide layer. Figure 1.6 gives the Pourbaix diagram of Al which shows the range of stability for phases in the water-Al system as a function of pH and electrical potential [21]. The stability range of water in the diagram corresponds to the region between the lines marked as (a) and (b). Below line (a), water reduces to form hydrogen

$$2H_2O + 2e^- \rightarrow H_2 + 2OH^-,$$
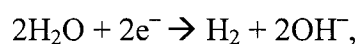
and above line (b), water oxidizes to form oxygen

$$2H_2O \rightarrow O_2 + 4H^+ + 4e^-.$$
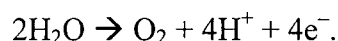
According to the diagram, the hydrated form of Al oxide is observed to be passive in the pH range 4 to 8.5. Beyond the limits of its passive range, Al corrodes in aqueous solutions because its oxides are soluble in acid and base, yielding Al^{3+} and AlO_2^- ions respectively.

Figure 1.7 shows an accepted model for the naturally-formed oxide layer on Al. It consists of two parts: a thin and compact barrier layer (10 Å) and a hydrated upper layer
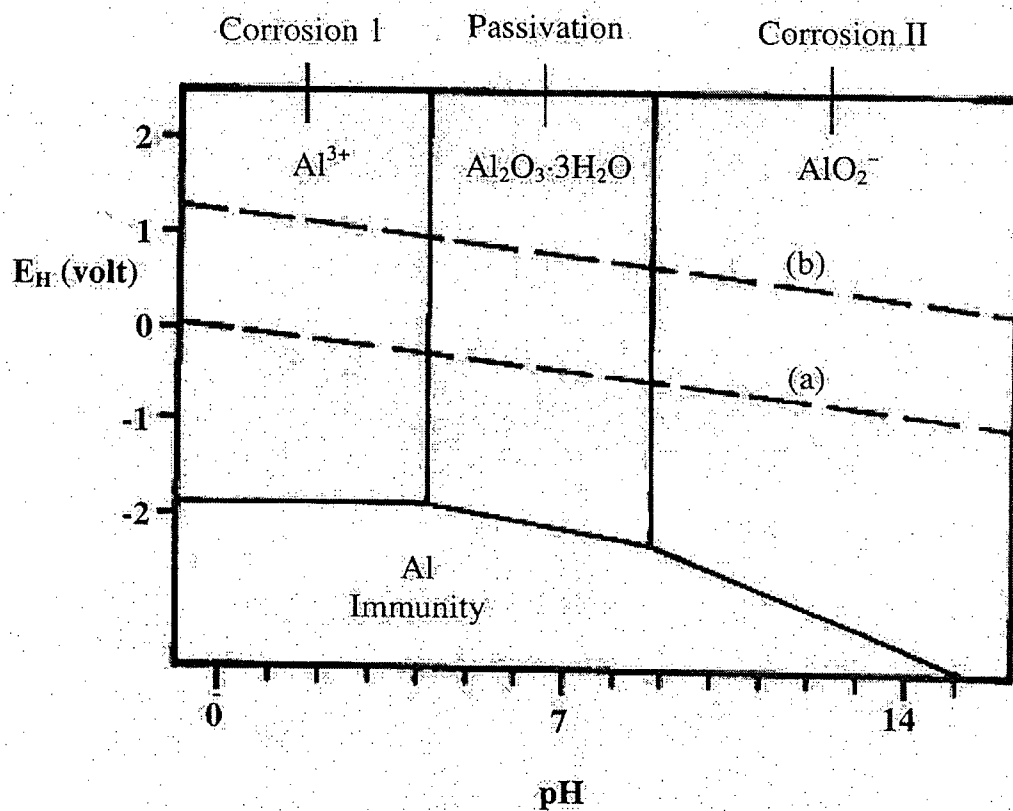
Figure 1.6. Potential-pH (Pourbaix) diagram for Al-water system at 25°C [21].
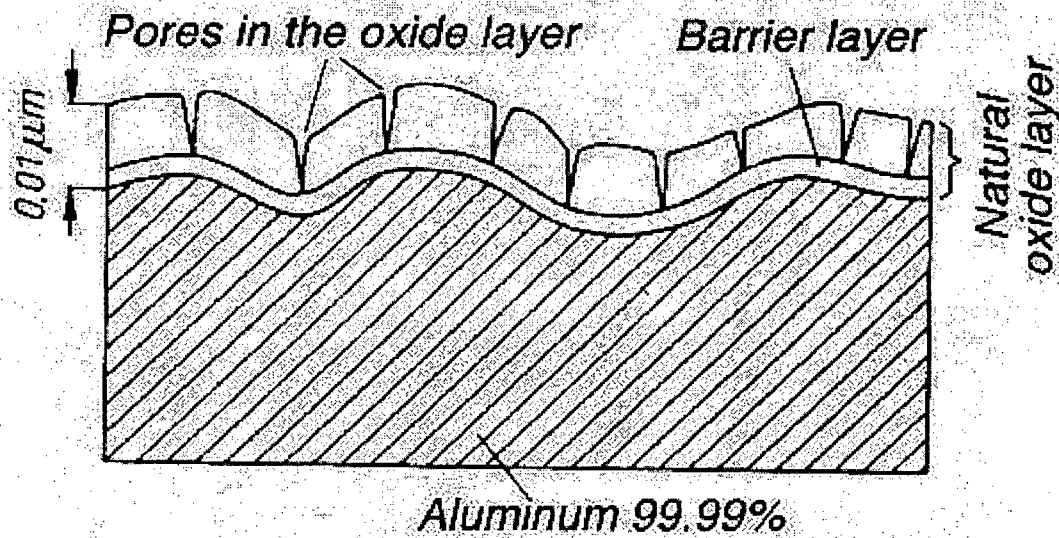
Figure 1.7. Native oxide layer of aluminum [1].

11

of about 90 Å in thickness. The barrier layer is amorphous and the hydrated upper layer is more permeable and porous. This model was proposed by Hunter *et al.* from investigations with combination of electron microscopy, electron diffraction, and conductivity measurements [22]. The oxide that forms on the intermetallic constituents (e.g. $CuAl_2$) have different natures (e.g. electrical characteristics) from those that form on Al.

To improve the corrosion resistance of high-strength Al alloys, surface modifications such as cladding and anodizing are used [2, 23-26]. In the latter case, the oxide film grown helps improve the corrosion protection, but it also provides the substrate on which paint or adhesives are applied. However, when dealing with large Al structures, anodization is too expensive and is not suitable for parts that need further mechanical treatment. Thus other methods such as conversion coatings are frequently used for the protection of Al alloys. Conversion coating is a process where chemical treatment leads to formation of a protective inorganic compound on the metal substrate.

Magnesium in contact with air also forms Mg oxide; however, the situation for Mg differs from that of Al. For example, an air-exposed Mg surface is known to contain MgO, $Mg(OH)_2$, and hydrated Mg-carbonate [27]. Figure 1.8 shows the Pourbaix diagram of Mg where the whole stability domain of Mg is well below that of water. Even though above pH of 12, a passive zone can be obtained due to the protective qualities of $Mg(OH)_2$, that is unstable at pH less than 12. The hydroxide and the carbonate products are unstable in air and salt solutions, and furthermore Mg is anodic to almost all metals. Therefore, galvanic corrosion is a problem for Mg alloys in the presence of the electrolytes.
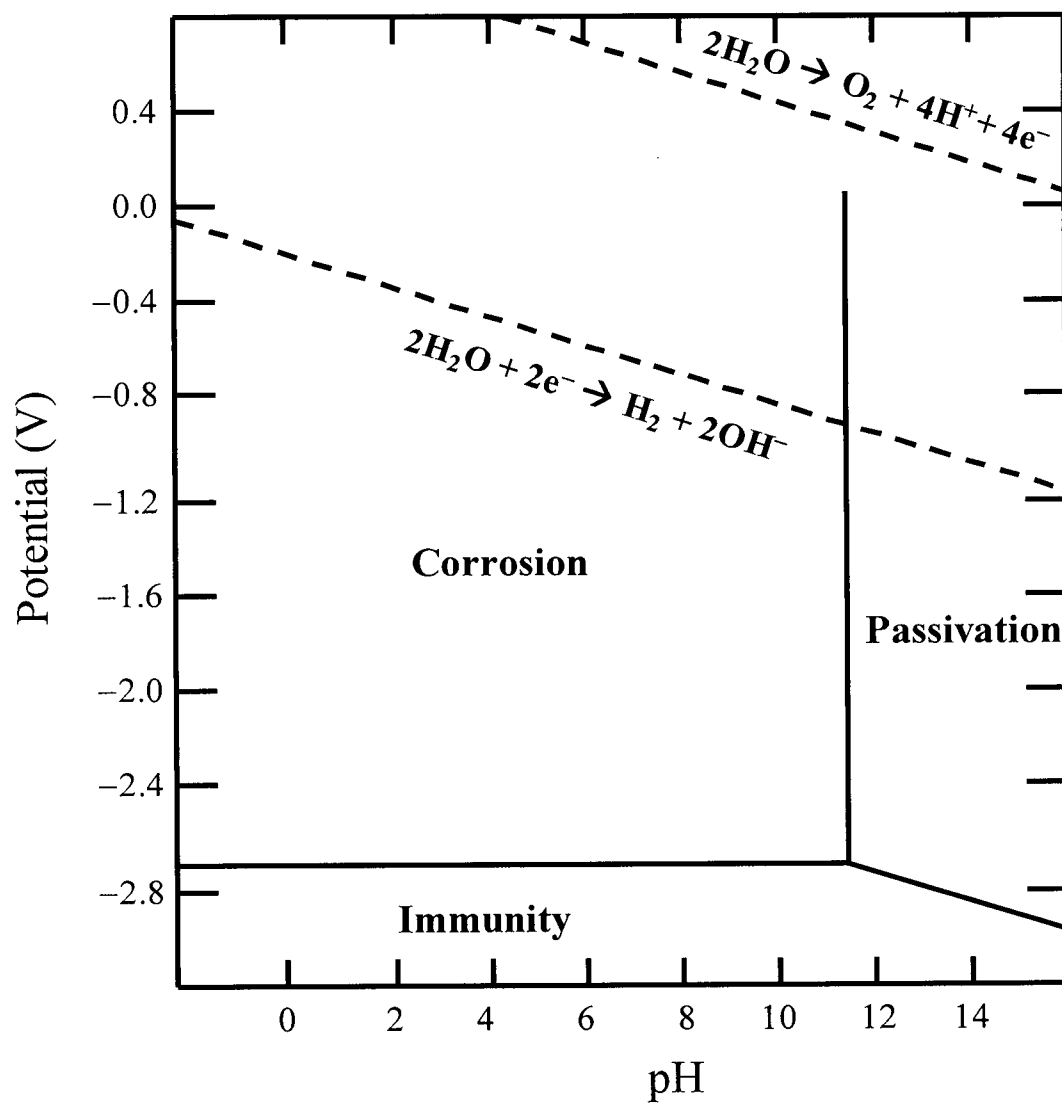
Figure 1.8. Pourbaix diagram for Mg-water system at 25°C (modified from Ref. [17]).

Compared to protecting Al alloys, the protection of Mg alloys is still difficult. To date, a number of coating methods such as electroplating [28, 29] and anodizing [30, 31] have been developed, but they only protect under moderate service conditions. The current recommendation for Mg alloy protection for indoor (and similar non-corrosive environments) consists of surface protection that can be achieved with chromate or phosphate conversion coatings followed by application of a primer or a decorative paint finish [27]. However, for harsh corrosive environments, a multi-step process is required. Initial chromate or anodic pre-treatments are required, followed by a baking seal with high temperature organic resins, where three coats of resin need to be applied. This is followed by application of a low-temperature curing with chromate inhibited primer and a compatible top coat system [27]. Thus, although it appears that protection methods for Mg alloys can be achieved, the process is a complicated multi-layer, multi-step process. Therefore, cheaper and more environmentally friendly processes are needed.

A traditionally-used conversion coating process for metals such as aluminum and magnesium is chromating, where solutions of CrO_3, $Na_2Cr_2O_7$, and NaF are used to form hydrated Cr(III) and Cr(VI) oxides on the metal surface [32, 33]. The chromating process provides excellent corrosion resistance as well as paint adhesion for metals but, because of its health concerns (Cr(VI) is reported to be carcinogenic), alternative methods are now required by legislation [34]. An alternative conversion coating to chromating is phosphating, where solutions containing phosphoric acid and divalent metal ions (e.g. Zn^{2+} or Mn^{2+}) are used to deposit metal phosphate layers on the metal. This method does not work as well as for chromating, and it requires a chromic acid post-rinse. Another possibility is to replace the conversion coating approach by treating with organosilanes.

In principle, this offers a more environmentally-friendly approach but it is still very much in the developmental stage [35-37].

1.2 Organosilanes

1.2.1 Use as Coupling Agents

Coupling agents are chemicals that unite different phases in contact by forming strong water and chemical resistant bonds [37]. Organofunctional silanes are one group of coupling agents that have been studied for the last three decades, starting with work to bond glass fibers to organic polymer system (e.g. paints which include epoxies, polyurethanes, polyesters, acrylics) [38]. Many organosilanes have a formula of the type $X_3Si(CH_2)_nY$, where X represents a hydrolyzable group, such as methoxy or ethoxy (i.e. OR), and n is typically 3. When these groups undergo hydrolysis according to

$$(RO)_3Si(CH_2)_nY + 3H_2O \rightarrow (HO)_3Si(CH_2)_nY + 3ROH,$$
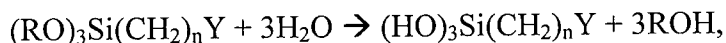
silanol groups (SiOH) are formed which can condense with hydroxyl groups on the substrate surface with elimination of water. In the formula, Y is an organofunctional group (e.g. Cl, NH_2, SH) chosen for compatibility with the organic coating to be subsequently added. In principle, the bonds resulting between the organosilane and substrate are more stable to the ingress of water than the van der Waals' forces which would be the basis of adhesion in the absence of direct covalent bonding.

Table 1.1 indicates some examples of organosilanes used commercially. The cases of γ-glycidoxypropyltrimethoxy silane (γ-GPS) and γ-aminopropyltriethoxy silane (γ-APS) have been used as commercial coupling agents since 1969 [39]. The table also shows a non-functional organosilane, bis-1,2-(triethoxysilyl) ethane (BTSE), which has

received some recent interest as a coating on metal surfaces [35-37]. The non-functional organosilanes have the Y group replaced by additional hydrolyzable groups which then occupy both ends of the hydrocarbon chain.

Table 1.1. Some examples of organosilanes.

Functional organosilane	Acronym	Formula
γ-Aminopropyltriethoxy silane	γ-APS	$H_2N\text{-}(CH_2)_3\text{-}Si\text{-}(OC_2H_5)_3$
γ-Glycidoxypropyltrimethoxy silane	γ-GPS	$CH_2\text{-}CH\text{-}CH_2\text{-}O\text{-}(CH_2)_3\text{-}Si\text{-}(OCH_3)_3$
Vinyltriethoxy silane	VS	$(H_5C_2O)_3\text{-}Si\text{-}CH{=}CH_2$
Non-functional organosilane		
Bis-1,2-(triethoxysilyl) ethane	BTSE	$(H_5C_2O)_3\text{-}Si\text{-}CH_2\text{-}CH_2\text{-}Si\text{-}(OC_2H_5)_3$

The typical process for coating a metal substrate with organosilane starts with a pre-treatment that cleans the oxidized surface mechanically or chemically. Brush cleaning or sand blasting can be used for the former, but those procedures can lead to rough surfaces and may also remove too much of the oxide layer. In the alternative, chemical etching produces a cleaner surface, and the treatment can also lead to formation of a compact new oxide layer. Typically-used etching processes involve alkaline and chromic acid pickling treatments (e.g. that from the Forest Products Laboratory, abbreviated later as FPL), where the combination of the new oxide formed and the surface morphology of the pre-treated surface aid in the organosilane coating process [35, 37, 40-42]. After the pre-treatment, the metal is dipped into the freshly hydrolyzed organosilane solution.

The coating process depends on a number of factors of which most notable are pH and the concentration of organosilane solution. The pH of the hydrolysis reaction should be set so that the hydrolysis is maximized and the direct condensation of the hydrolyzed organosilane molecules is minimized. For most organosilanes, this pH range is between 4 and 6 where acetic acid can be used to enhance the hydrolysis reaction. Acetic acid is chosen because other acids can ultimately lead to corrosion whereas the acetic acid will largely evaporate after coating. For the amino-organosilanes, the pH range for optimal hydrolysis (via base catalysis) is in the range of 8 to 10 due to the presence of the basic amino group [36, 43]. The pH of the coating process is also important with regard to the metal under consideration; ideally a pH region should be used where the metal is stable [37].

Regardless of the organosilane type, the film thickness generally appears proportional to the organosilane solution concentration for a given exposure time [35, 36]. An increase in solution concentration leads to more SiOH groups available for the polymerization reaction. However a thicker film does not necessarily imply a better quality film; films that are too thick become brittle [35-37].

1.2.2 Possibilities for Corrosion Protection

Although in the past organosilanes have been widely used as coupling agents, since the early 1990's studies have been made to test whether this can be taken a stage further to promote the corrosion protection of metals. Investigations have been made on various metal substrates, such as aluminum alloys [35, 37, 44-47], steels [44, 48], and copper [49, 50], which suggest that the organosilane coatings can help protect the metals

against corrosion. This can work in two ways: the organosilanes may bond to the metallic surface via the formation of direct metallo-siloxane bonds; secondly the silanol groups can crosslink to form a Si-O-Si network after polymerization.

In principle, the bonding between an organosilane and an oxidized metal surface can be optimized by the formation of direct metal-O-Si covalent interactions [36]. Plueddemann proposed that hydrolysis of the $Si(OR)_3$ groups by water produces silanol groups (i.e. $Si(OH)_3$), which then condense with OH groups on the oxide surface, and so lead to the formation of direct metal-O-Si bonds after the elimination of H_2O [38]. Figure 1.9 schematically indicates such a coating process on an oxidized metal surface.

In addition, after the coating, the silanol groups not used in the interfacial bonding can be used to form Si-O-Si bonding according to the condensation reaction: SiOH + SiOH → Si-O-Si + H_2O. The Si-O-Si bonding is resistant to water, solvents and acids [37, 43, 44, 51, 52]. Furthermore, the film retards the transport of all corrosive ions (such as chloride) towards the metal [37]. A number of studies have reported that the highly crosslinked or dense interfacial layer that developed between the organosilane film and the metal oxide was the major contribution to the corrosion protection of metal surfaces. As well, the number of silanol groups of the fully hydrolyzed organosilanes had a big influence on the barrier properties of organosilane layer and thus on their corrosion properties [44, 51, 53].

For the corrosion protection, organosilanes are applied on the metal surface and then paint is applied. This is the case for some functional organosilanes (e.g. γ-APS) where, without the paint, the organosilane was found to de-adhere when exposed to water [54, 55]. On the other hand, Van Ooij et al. [36] have reported that the non-functional

a)

CH_3CH_2O \
CH_3CH_2O—Si—C—C—Si—OCH_2CH_3 ⟶ HO—Si—CH_2-CH_2—Si—OH \
CH_3CH_2O H_2 H_2 OCH_2CH_3 H_2O

BTSE: bis-1,2-(triethoxysilyl)ethane

b)

HO—Si—CH_2-CH_2—Si—OH ⟶ HO—Si—CH_2-CH_2—Si—OH

Metal Substrate

H_2O

Metal Substrate

Figure 1.9. Adsorption of BTSE on metal substrate: a) hydrolysis reaction, b) interfacial covalent bond formation.
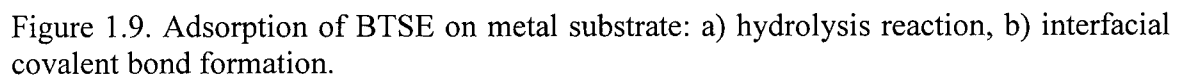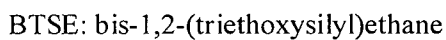
organosilane (BTSE) provides good corrosion protection without the need for a paint layer to protect a metal surface. BTSE has six silanol groups available after its hydrolysis and thus has the possibility to form more metal-O-Si bonding at the interface compared to other organosilanes such as γ-GPS or γ-APS. Furthermore, the greater number of silanol groups also means that there are more chances for Si-O-Si bond formation after the polymerization, so leading to denser films. Additionally, since BTSE is a stronger acid than the other organofunctional silanes, it can react more easily with weakly basic hydroxyl groups on the oxidized metal surfaces. Although BTSE appears to offer good corrosion protection at the first level, the lack of an organofunctional group limits its ability to bond with a subsequent paint coating [36, 37]. Thus, to avoid that problem, a two-step coating process has been proposed, where a successive application of a non-functional organosilane (like BTSE) is followed by an organofunctional silane [36, 37]. Examples of such two step coating processes have been applied to cold-rolled steel, and to the 3003-Al and 2024-Al alloys [35-37], with results for corrosion protection that appear as promising as for other existing systems [36, 37]. In principle, the two-step coating process is not needed for organofunctional silanes such as γ-APS. In that case, the corrosion protection is not as good as for BTSE, apparently because of a smaller number of available SiOH groups for forming the SiOSi units. Also, γ-APS initially forms primarily hydrogen bonds with the metal surface, which are weaker and impart less protection than the covalent bonds believed to form with BTSE [37, 56-58].

A current belief is that a good quality organosilane film is one which is: solidly anchored to the metal by Si-O-metal bonds, ~50-100nm thick, homogenous and cross-

linked via Si-O-Si bonds, has plenty of functional groups that can react with a subsequent coating, and is stable in the atmosphere [36].

Although a number of studies involving organosilane coating on Al alloy surfaces have been reported [51, 54, 59-64], most work in this area has been of a more macroscopic nature. Such testings have used the Boeing wedge test, the peel test, the salt fog test, or anodic polarization [59-61] as well as electrochemical impedance spectroscopy [51, 54, 62, 63]. In addition, the question of the presence of direct metal-O-Si bonding has been a difficult to answer, and has received considerable attention in a variety of studies that have explored the interfacial bonding between organosilanes and metal substrates, using such technique as secondary-ion mass spectrometry (SIMS) [65, 66, 67], vibrational spectroscopy [68-70], and X-ray photoelectron spectroscopy (XPS) [56, 71]. However, recent TOF-SIMS studies have given a very strong support for the presence of AlOSi and ZnOSi bonds at the oxide-silane interfaces [67] where the work has focused more on detecting the presence of metal-O-Si bonding rather than investigating the conditions that optimize the presence of these covalent interactions. In order to strengthen the application of organosilane, more microscopic research is needed for pre-treatments that may enhance the interfacial bonding at the metal-organosilane interface as well as its affect on corrosion protection.

1.3 Objectives of Research

Although considerable effort has been made to demonstrate the effectiveness of organosilane coatings on Al substrates, the mechanistic factors that underline the coating process are still not well understood, especially in relation to the specific chemical

compositions occurring on the alloy surfaces. Studies involving organosilane coatings on Mg alloys are scarce [72] and thus this area is one that needs development. Previous research in our group has studied the adsorption of organosilanes on aluminum and its alloys [56, 65, 71, 73-74]. Investigations have been done to study the effect on the silane coating of various pre-treatments [73], as well as exploring the presence of covalent bonding at the organosilane-metal interface [65, 71]. The first aim of the work presented in this thesis is to investigate the processes involved in coating BTSE on high-purity aluminum surfaces, with attention given to accessing the interfacial bonding. This system allows for studying factors that affect the coating process, without the complications that arise from the chemical heterogeneity of an alloy surface or from organofunctional groups on the silane. This work includes variations in the nature of the oxide layer, and contributes to the microscopic studies that were noted above as being required to better understand the nature of the silane-oxide bonding. Others have shown that the presence of microstructures at Al alloy surfaces can affect the processes that occur upon exposure to corrosive environments [6, 8], but to our knowledge little research has been published with regard to how an organosilane coating is affected by these microstructures. One exception is a recent study from this group that investigated the adsorption of organosilanes on the microstructural regions of a 2024-T3 Al alloy surface [74]. To help build more understanding for the organosilane coatings formed on microstructural regions of Al alloys, this work deals with variations in both the alloy and the nature of the organosilane used.

For the Mg alloys, there also have been reports on the role surface microstructure plays upon exposure to corrosive environments [16, 75-77]. No previous work has been

done on Mg alloys by our group, and thus the first aim of the work involves investigating the chemical compositions of the AZ91-Mg alloy. This is followed by a study of organosilane coatings on this alloy, with the hope it can develop principles for coating chemistry in this type of situation.

This thesis is organized as follows. Chapter 2 describes the techniques used in the research: X-ray photoelectron spectroscopy (XPS), scanning electron microscopy (SEM), energy dispersive X-ray spectroscopy (EDX), scanning Auger microscopy (SAM), and secondary ion mass spectrometry (SIMS), while Chapter 3 reports investigations for interfaces formed between BTSE and some oxidized Al surfaces after different pre-treatments. Chapter 4 describes some studies for adsorption of the organosilanes BTSE and γ-GPS on different microstructural regions of the 7075-T6 Al alloy, and Chapter 5 discusses investigations for the AZ91-Mg alloy, including its native oxide and organosilane adsorption on its surface. Chapter 6 concludes with a summary and suggestions for follow-up research on these topics.

Chapter 2 Experimental Methods

2.1 Electron Spectroscopy

2.1.1 Introduction

Electron spectroscopy is a method for analyzing electrons that are emitted from a sample after it has been irradiated by an excitation source, and two widely used techniques are X-ray photoelectron spectroscopy (XPS) and Auger electron spectroscopy (AES). These methods can provide qualitative and quantitative information of all elements (except H and He) for the surface region (topmost 50 Å or so) of a solid sample [78-80]. In XPS, the sample is irradiated by soft X-rays and the kinetic energies of the photoelectrons ejected from core levels in the sample are measured according to the process shown in Figure 2.1(a). The kinetic energy of the photoelectron (E_k) is

$$E_k = h\nu - E_b, \tag{2.1}$$

where $h\nu$ and E_b are respectively the incident X-ray energy and the binding energy of the electron in the sample. The measurement of the kinetic energies of the photoemitted electrons can provide elemental identification for the sample since different elements have different characteristic sets of electronic binding energies. Also, since there are small variations in E_b values for the same atom in different bonding states, high-resolution measurements can also provide chemical state information.

The irradiation of a sample surface by X-rays can also give rise to Auger electrons produced by the process shown in Figure 2.1(b). This process starts with an initial core vacancy and the system can relax by a two-electron process where one electron fills the vacancy and the other is emitted as an Auger electron. The Auger electron in Figure
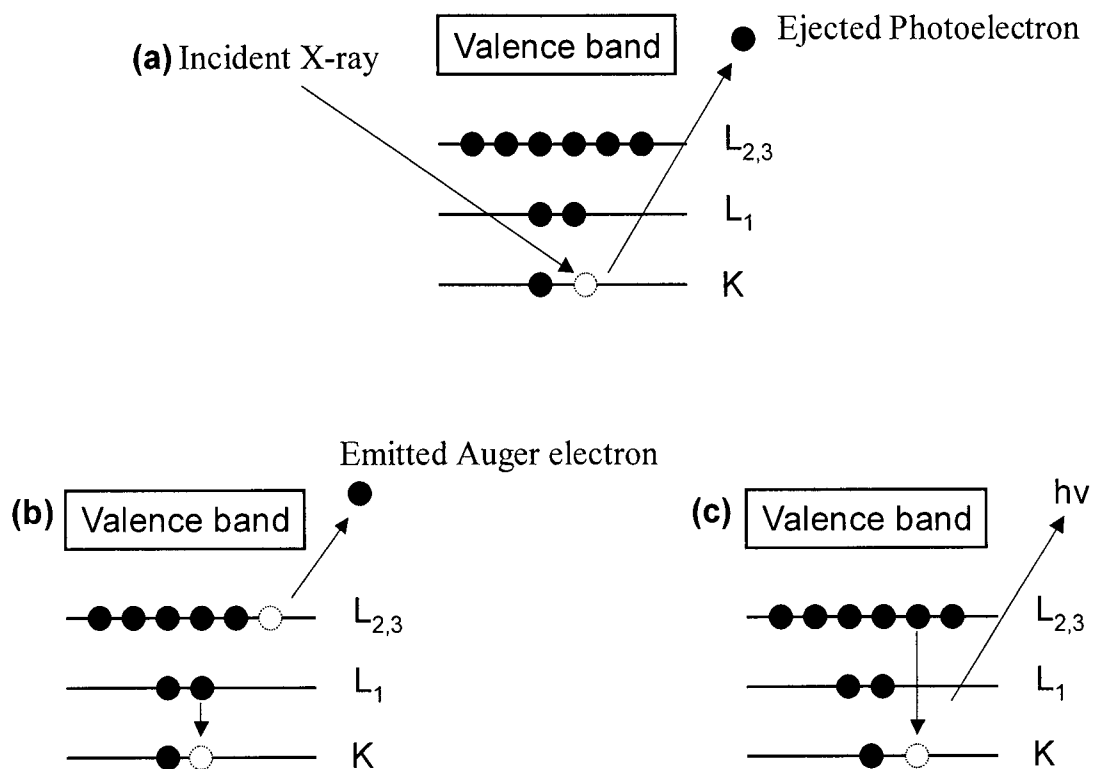
Figure 2.1. Schematic diagram for: (a) photoelectron emission, (b) Auger electron emission, (c) X-ray emission.
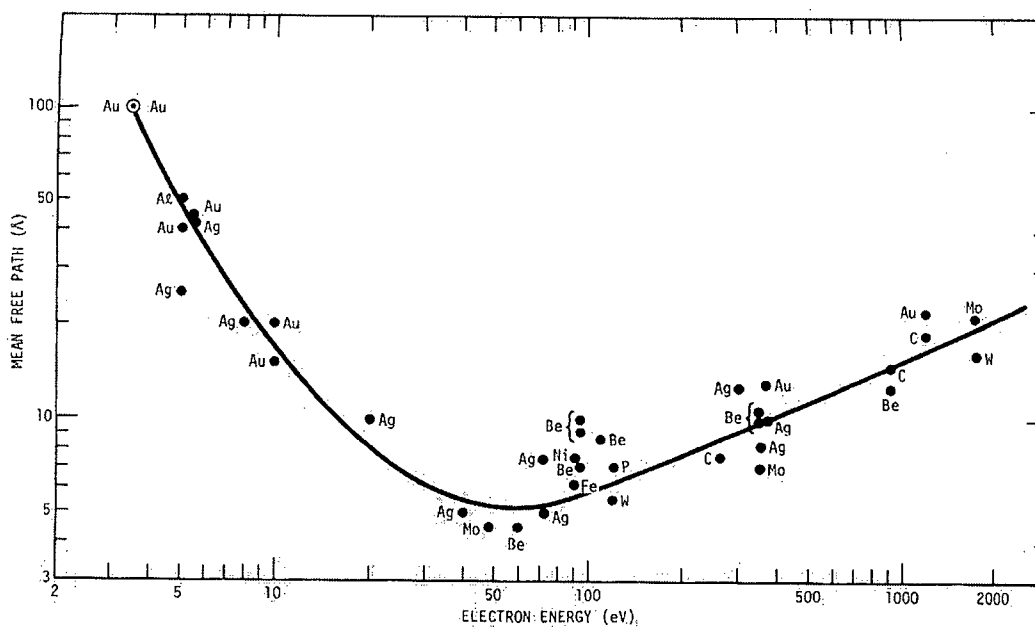
Figure 2.2. Dependence of mean free path on electron energy [1].

2.1(b) is characterized as a $KL_1L_{2,3}$ electron, and its kinetic energy is approximately equal
to

$$E_{KL_1L_{2,3}} = E_K - E_{L_1} - E_{L_{2,3}} , \qquad\qquad (2.2)$$

although a correction is strictly needed since the process starts with a singly charged ion
and finishes with one that is doubly charged [78-81]. However for our purposes, the
kinetic energy is a function of the atomic energy levels involved, and that allows
measured electron energies to give elemental identification. In addition, a change in
chemical state for an atom may also give rise to changes in Auger spectra measured at
high-resolution, again thereby providing chemical state information. Commonly Auger
electron spectroscopy is performed with an incident electron beam of sufficient energy to
ionize core electrons, and in the technique of scanning Auger microscopy (SAM), the
measurements are made with a finely focused electron beam, so that Auger electrons can
be detected from specific local regions of the sample.

Figure 2.1(c) also shows another possible process that can occur from an initial
excitation with X-rays or electrons. This process is called X-ray fluorescence, and it
provides the basis of the X-ray microanalysis, frequently called energy dispersive X-ray
spectroscopy (EDX), a technique which will be discussed later. Auger emission and X-
ray emission are competing processes, but Auger emission dominates if the binding
energy of the initial vacancy is less than about 2 keV. This is generally the case for the
lighter atoms, but X-ray emission dominates when the initial vacancy is in an inner level
for a heavier atom.

XPS and AES are surface sensitive techniques when the emitted electrons have
kinetic energies less than about 2 keV. For this situation, the electrons have a high

probability of experiencing inelastic collisions. The average distance traveled by an electron before losing energy is called the inelastic mean free path, λ, and Figure 2.2 shows λ values for different elements as a function of electron kinetic energy. It can be seen from the Figure that λ values are typically of the order of 10 Å for electrons with kinetic energies in the range from about 20 eV to 2000 eV [78, 80, 82]. This ensures that the electrons detected in sharp peaks in XPS and AES must have originated close to the surface. Strong inelastic scattering therefore gives XPS and AES their surface sensitivity [78, 81].

2.1.2 Qualitative Analyses

Figure 2.3(a) shows a XPS survey spectrum of Al coated with BTSE obtained using a MgKα excitation source where the spectrum is displayed as intensity (number of counts) versus binding energy. A survey scan covers a wide energy range (e.g. up to 1000 eV) and the measurements are made for low energy resolution. Identification of the peaks can be made with the aid of tabulated binding energy values given in Handbooks [83], and this survey spectrum shows the photoelectron peaks arising from direct excitation of core-level electrons which are labeled as Al 2s, Al 2p, Si 2s, Si 2p, C 1s and O 1s. In addition, X-ray induced Auger electron emission is detected for the O KLL and C KLL processes, and the sharp structural features in the spectrum are accompanied by a higher energy background, which corresponds to emitted electrons which have undergone inelastic scattering on their outward paths, and thus are detected with lower kinetic energy. XPS peaks are labeled by regular atomic orbital nomenclature.
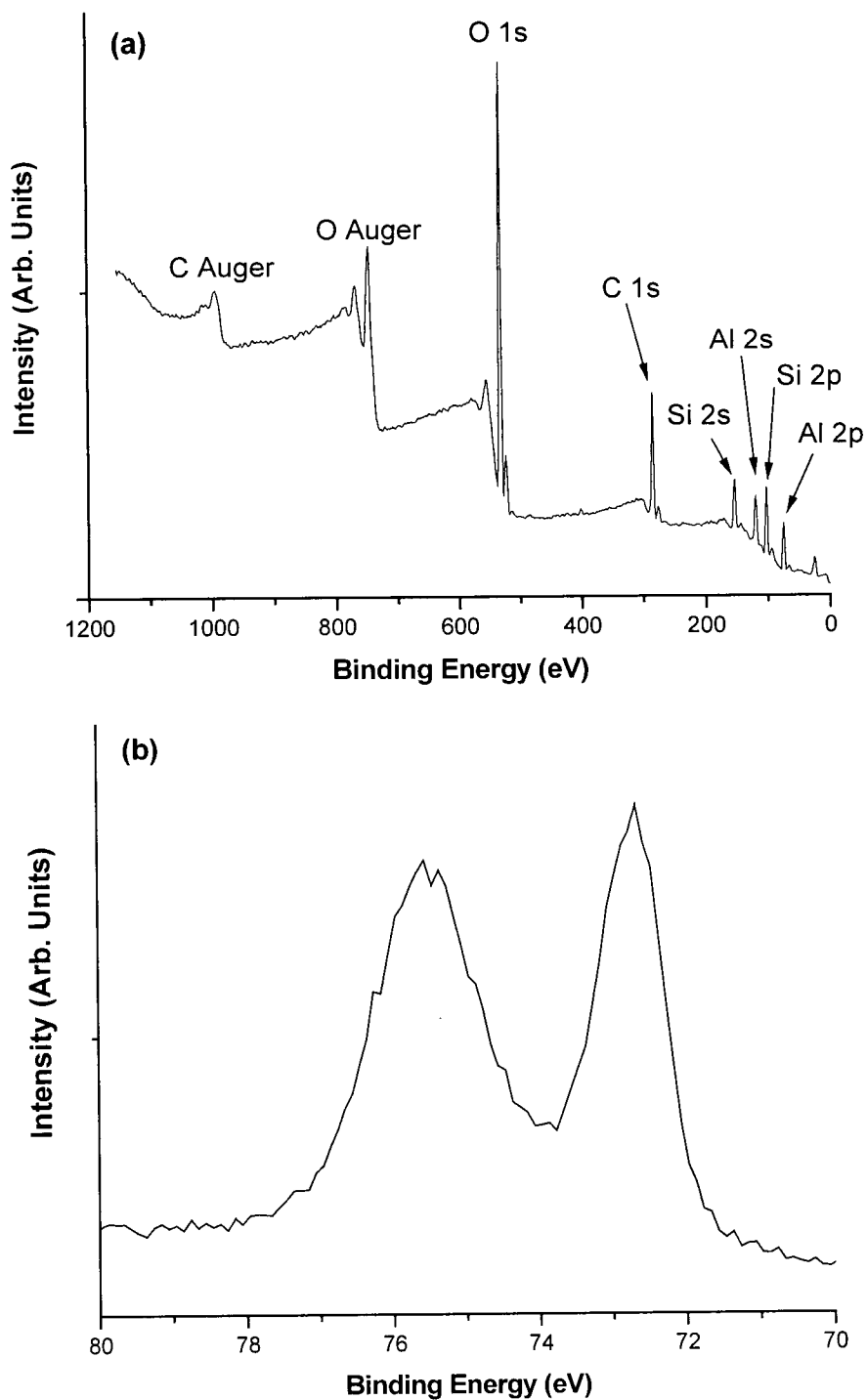
Figure 2.3. Measured XPS spectra: (a) survey scan spectrum for an Al coated with 1% BTSE, and (b) higher resolution Al 2p spectrum for high-purity Al treated with FPL for 60 min.

Higher resolution spectra are typically measured over a restricted energy range (e.g. 10-50 eV) for the element of interest. One example is shown in Figure 2.3(b) which shows a narrow scan spectrum for Al 2p peak structure from a high-purity Al sample. The two Al 2p peaks are shown resulting from two different chemical environments. The first peak at 72.7 eV binding energy is for metallic Al and the second peak at 75.5 eV is for Al oxide. This shift of binding energies gives information on the chemical environment of the atoms (valence state). Generally, the loss of valence charge density will show up as an increase in the binding energy of the core electrons [78, 79]. For heavier atoms, extra structure due to spin-orbit coupling can occur [84].

The nomenclature for Auger peaks also starts with conventional atomic orbital labeling, although because three levels need to be identified, a brief nomenclature based on the K, L, M notation is used (for n = 1, 2, 3, etc.) [78]. The levels are further identified by subscripts; for example L_1 for $2s_{1/2}$, L_2 for $2p_{1/2}$, L_3 for $2p_{3/2}$, and V for the valence band. Figure 2.4 shows an Auger electron survey scan for a AZ91-Mg alloy surface where the KLL peaks for oxygen, magnesium, and aluminum are indicated. Auger peak positions and shapes can also give information on the chemical environment of the element. Higher resolution Mg KLL spectra for metallic Mg and oxidized Mg are shown in Figure 2.5, where a series of peaks at kinetic energies 1186 eV, 1176 eV, 1164 eV, 1154 eV, 1141 eV, and 1130 eV are seen for metallic Mg. For the oxidized form, differences are observed with regards to relative intensities and a new peak appears at 1181 eV. This example shows that Auger spectra can also be used to identify chemical differences in the elemental bonding albeit the situation is more complex for AES than XPS because of the greater number of energy levels involved.
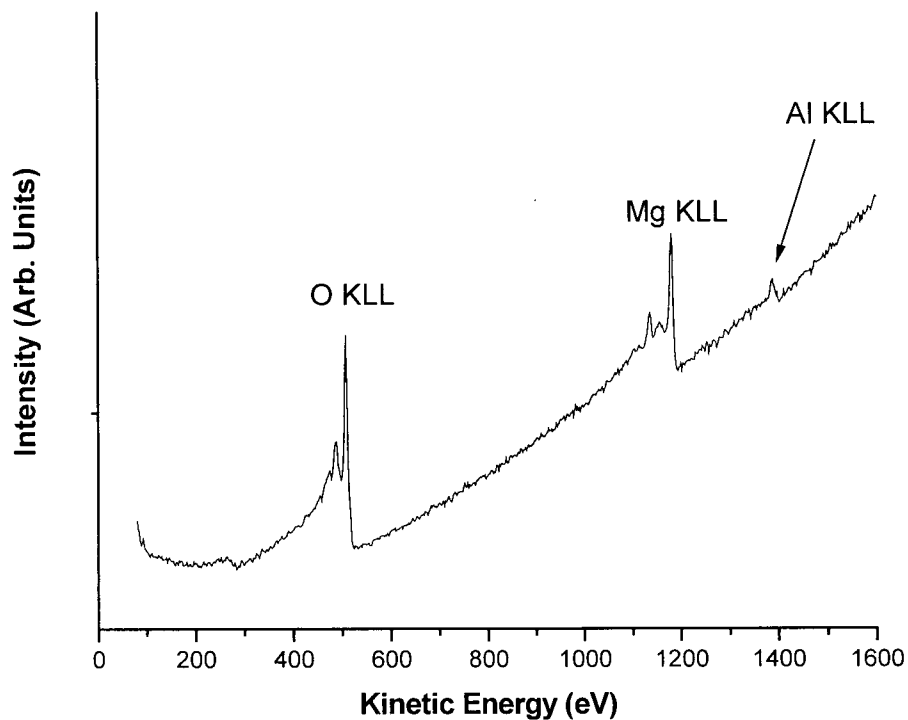
Figure 2.4. Auger survey scan from a mirror-polished AZ91-Mg alloy surface.
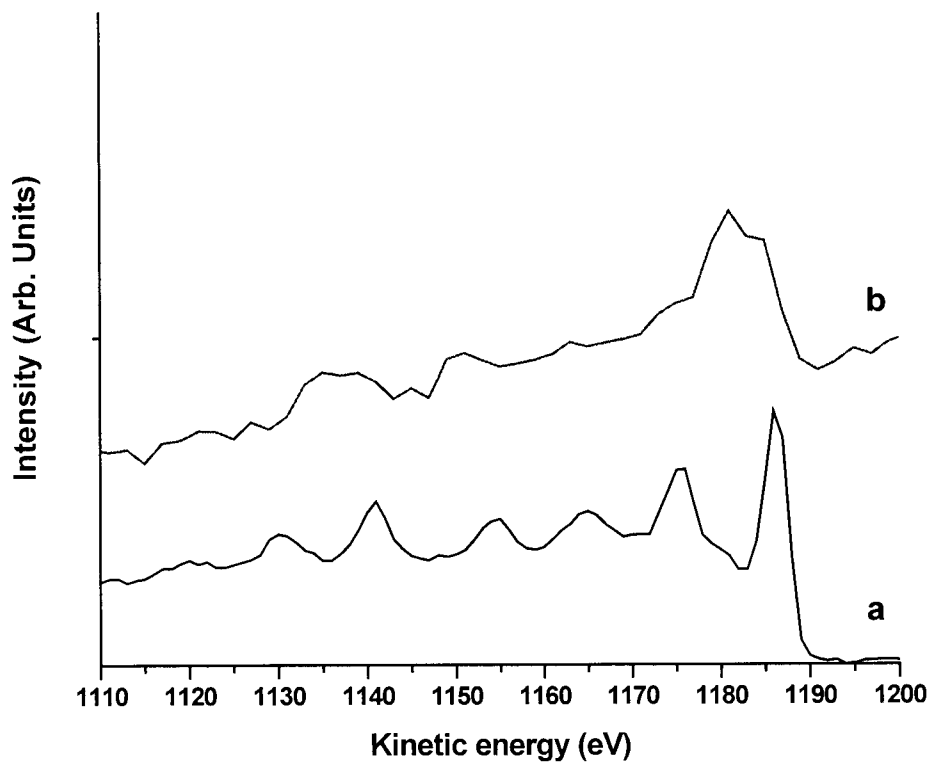
Figure 2.5. Mg KLL spectra for: (a) metallic Mg and (b) oxidized Mg.

30

2.1.3 Quantitative Analyses

The XPS and AES techniques can also provide quantitative information from analysis of measured peak intensities. The intensity contribution (dI) for electrons exiting the sample from an infinitesimal thickness dx at depth x is:

$$dI = n \, f \, \sigma \, A \, T \, \exp(-x/\lambda)dx, \qquad (2.3)$$

where n is the number of appropriate atoms per unit volume of the sample, f is the incident beam flux, σ is the scattering cross-section, A is the area of a sample from which electrons are detected, T is the instrumental transmission function, and λ is the inelastic mean free path. Simple integration for a semi-infinite homogeneous sample gives:

$$I = n \, f \, \sigma \, \lambda \, A \, T, \qquad (2.4)$$

where the contributions f, σ, A and T can all be grouped into an instrumental atomic sensitivity factor S, for given instrumental conditions and a given peak. In principle, the atomic ratio for two elements in the sample (n_1/n_2) can determined using the equation:

$$n_1/n_2 = [(I_1/S_1)/(I_2/S_2)] \, [(\lambda_2)/(\lambda_1)], \qquad (2.5)$$

using tabulated values of λ_1 and λ_2 for the appropriate electron kinetic energies [82]. However, for semi-quantitative work, the λ_2/λ_1 ratio is commonly taken as constant and equal to unity. Then the elemental composition ratio n_1/n_2 for the two elements within the depth probed can be determined directly from measured peak intensities and the ratio of sensitivity factors. This relationship can be further applied to give relative atomic percentages, for example

$$C_1 = n_1 \, / \, \Sigma \, n_i = [(\, I_1 \, / \, S_1 \,) \, / \, (\Sigma \, I_i \, / \, S_i)] \times 100, \qquad (2.6)$$

where i is summed over the various constituents in the sample.

In practice, the measured spectral peaks have to be corrected for background prior to quantification. The non-linear background subtraction method introduced by Shirley [85] has been used for this purpose and is discussed with the spectrum shown in Figure 2.6(a). This method assumes that the number of inelastically scattered electrons at any point in a spectrum is proportional to the number of elastically scattered electrons at higher kinetic energies. The correction for the inelastic contribution over an energy range E_1 to E_2 (chosen by the operator) is given by the iterative algorithm:

$$N'_{K+1}(E) = N(E) - N(E_2) - C \int_{E}^{E_2} N'_K(E)dE, \qquad (2.7)$$

where $N(E)$ is the measured count rate and $N'_K(E)$ is the background corrected count rate (the index K indicates the K-th iteration). The reference background level is provided by $N(E_2)$ and C is fixed by a requirement that $N'_K(E_1) = 0$. The process starts with $N'_1(E) = 0$ and continues until $N'_{K+1} \sim N'_K$; convergence normally takes about four iterations.

To maximize the information extracted from the XPS spectrum, after background subtraction, a curve fitting process is used to identify the overlapping chemical species that may be contributing, and an example is shown in Figure 2.6(b). This approach requires some chemical knowledge of the system to realistically estimate the different chemical species that may be present for the element of interest. Each such species is represented by a mixed Gaussian-Lorentzian function which represents an approximation to the Voigt function (convolution of Lorentzian with Gaussian) [78] incorporating variations in peak position, peak height and peak width expressed as full width at half maximum (FWHM):

$$f(E) = \text{peak height} / [1 + M(E-E_x)^2 / \beta^2] \exp\{(1-M) [\ln2 (E-E_x)^2] / \beta^2\}. \qquad (2.8)$$
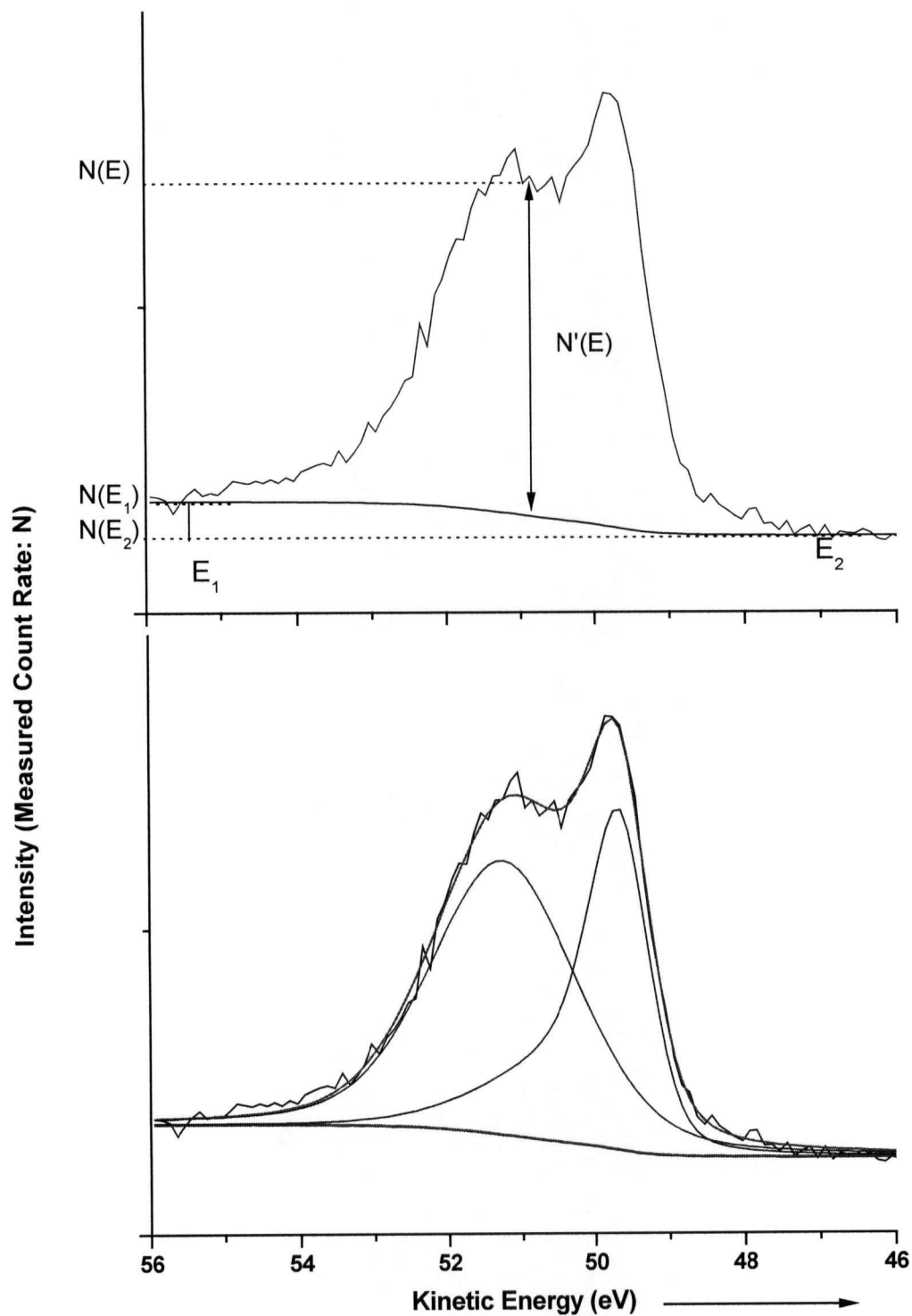
Figure 2.6. Shirley approach applied to Mg 2p spectrum: (a) non-linear background correction, and (b) fitting to oxide and metallic components.

In Equation (2.8), E_x is the maximum of the individual component, β is a parameter that fixes the FWHM (optimized values are often close to 0.5), and M is a mixing ratio (1 for pure Lorentzian function, 0 for pure Gaussian).

A set of functions like that in Equation (2.8), to represent the different components, are iterated to optimize the fit between the measured spectrum and the simulated spectrum. At each stage in the optimization, the quality of the curve fit obtained can be evaluated by using the least-squares function (χ):

$$\chi = \{(1/N_{free})\sum_i (Y_{mea,i} - Y_{fit,i})^2 / Y_{mea,i}\}^{1/2} \qquad i = 1,....N. \qquad (2.9)$$

$Y_{mea,i}$ is the measured count rate at the i-th data point, $Y_{fit,i}$ is the corresponding value of simulated function; N is the number of data points and N_{free} equals $N - N_{fit}$, where N_{fit} is the number of parameters to be fitted. The smaller the χ value, the better the quality of fit between the measured spectrum and the sum of the curve fitted components. However, visual comparisons are still needed to ensure that the curve fitting procedure does not introduce any artifacts of a non-chemical nature.

In a common situation, a sample consists of an overlayer (thickness d) on top of a substrate material. A simple overlayer model, assuming that the overlayer formed is uniform and homogenous, can be adopted to estimate its thickness. For this purpose Equation (2.3) can be integrated for the substrate and overlayer to yield:

$$I_s = n_s\, f\, \sigma_s\, A\, T\, \lambda_s \exp(- d/\lambda_{so}) \qquad (2.10)$$

$$I_o = n_o\, f\, \sigma_o\, A\, T\, \lambda_o\, [1 - \exp(-d/\lambda_o)] \qquad (2.11)$$

for photoelectron intensities from the substrate (I_s) and the overlayer (I_o) respectively. λ_s and λ_o are inelastic mean free paths for photoelectrons originating in, and traveling in, the substrate and overlayer respectively, while λ_{so} is the inelastic mean free path of

photoelectrons from the substrate traveling in the overlayer. In Section 5.3.1, Equations

(2.10) and (2.11) are used to determine the thickness of an oxide film on an AZ91-Mg

alloy.

2.2 MAX 200

The Leybold MAX200 spectrometer was used for the XPS work presented in this

thesis. This instrument operates in the ultrahigh vacuum (UHV) pressure range (10^{-9} to

10^{-11} Torr) and it is equipped with a dual-anode X-ray source, a hemispherical energy

analyzer, an ion gun for sample cleaning, and magnetic coupling transfer rods for sample

movement between the four interlinked chambers shown schematically in Figure 2.7. A

sample can be moved under vacuum between the transfer chamber (sample entry), the

analysis chamber, the metal deposition (gas dosing) chamber, and the plasma chamber.

As indicated, the UHV conditions are achieved by a combination of turbomolecular and

ion pumps where each turbomolecular pump is backed by a rotary pump. In addition, the

analysis chamber can be pumped by an auxiliary titanium sublimation pump. Operation

of the spectrometer requires UHV conditions for several reasons. First, the sample

surface can be kept longer in its original state while picking up less surface contamination

than would occur in a higher pressure environment. This basic requirement follows from

the high surface sensitivity of the electron spectroscopic method used. Second, only for

low pressure conditions can a high proportion of the emitted photoelectrons reach the

energy analyzer without being scattered by the residual gas molecules. Third, a low

pressure condition is needed for effective operation of the X-ray source and other

analysis components.
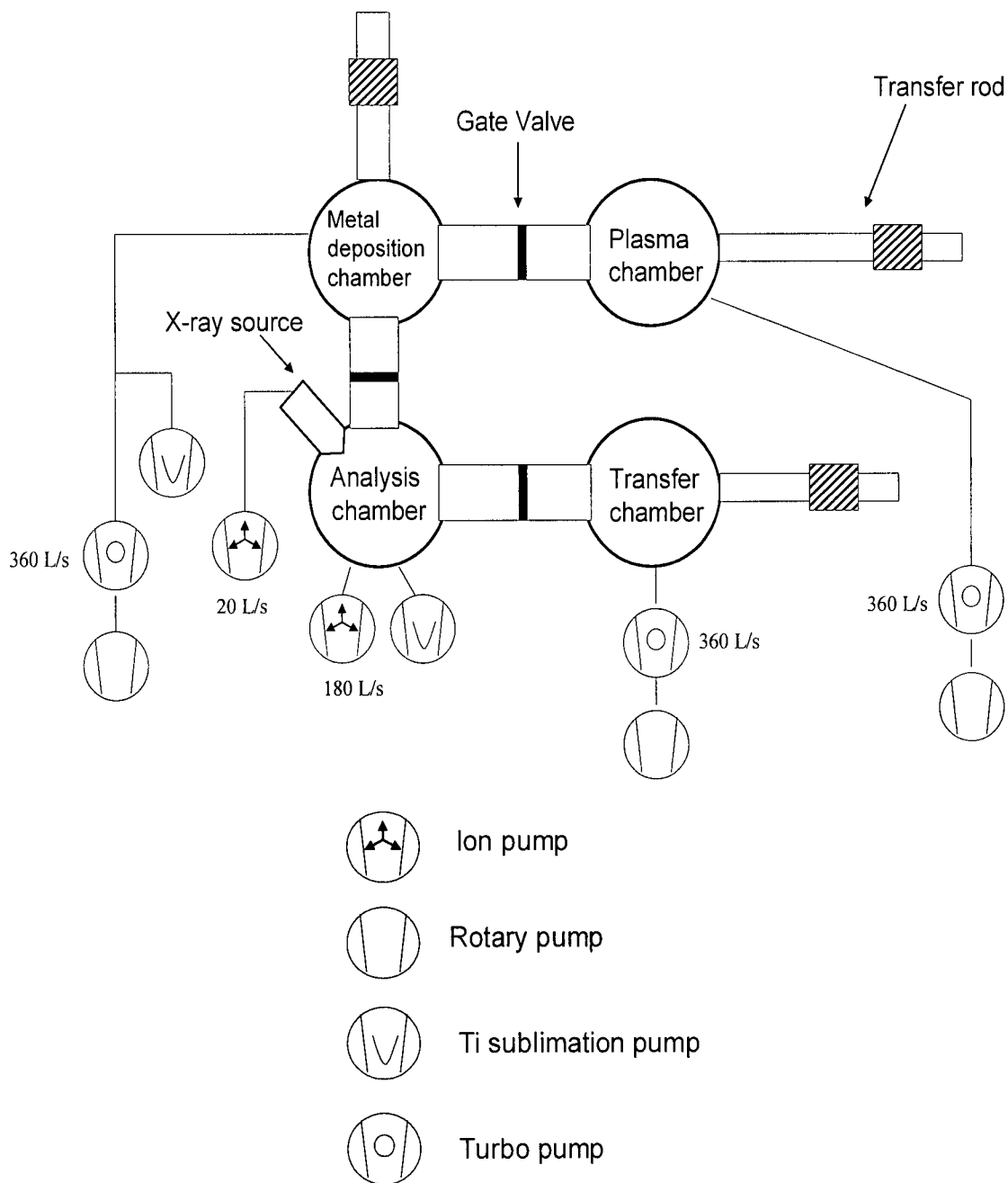
Figure 2.7. Schematic indication of pumping system for the MAX 200.

2.2.1 Excitation Source

X-rays are produced by bombarding an anode with electrons, from a heated filament, which have been accelerated through 10 to 15 kV. The MAX 200 is equipped with a dual anode X-ray source that has Al and Mg deposited on different faces of the anode block and a selection of the anode is accomplished by a simple switch. The anode is cooled by a deionized water system to prevent failure due to heat generation during operation. This dual anode source produces $K\alpha$ lines of Al and Mg, with energies of 1486.6 eV and 1253.6 eV respectively. Their respective line widths are 0.85 eV and 0.70 eV. The Al K_α source is most frequently used since its higher energy allows a wider energy range spectrum to be obtained. If better energy resolution is required, the MgK_α or a monochromatized Al $K\alpha$ source can be used (the MAX200 does have the monochromatized source, although it was not used in the work reported in this thesis). An Al foil window of thickness (2 μm) is positioned between the anode and sample in order to prevent stray electrons and contamination from the anode region reaching the sample. This window also helps reduce the intensity of additional X-ray lines (K_β) that can add satellite structure in an XPS spectrum, and it is sufficiently thin that the X-ray flux reaching the sample is not significantly attenuated [78].

2.2.2 Electron Energy Analyzer

Figure 2.8 outlines the analyzer system of the MAX200 which consists of the collection lens system, the energy analyzer, and the multichannel plate (MCP) detector. The collection lens system functions in two stages where the first stage controls the analysis area (spot size) and collection angle for the electrons coming from the surface.
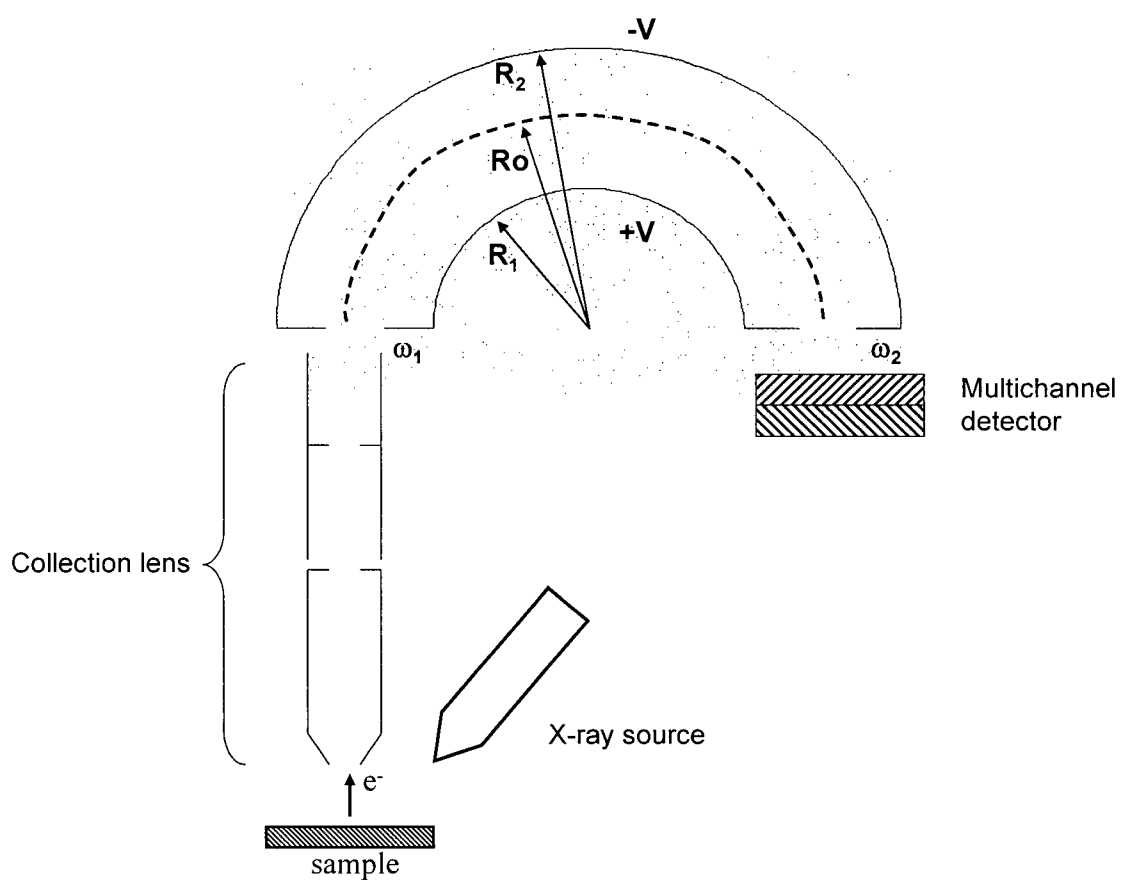
Figure 2.8. Schematic diagram for the lens system and the concentric hemispherical analyzer (CHA) in the MAX 200 (modified from Ref. [1]).

The second stage retards the electrons to a particular pass energy value and controls the angle at which electrons enter the analyzer.

The MAX200 uses a concentric hemispherical analyzer shown schematically in Figure 2.8. This type of analyzer is discussed in more detail in standard accounts [78, 86-88], but in outline it consists of two concentrical hemispheres (inner radius R_1, outer radius R_2). A potential difference (ΔV) is applied across the hemispheres such that the outer one is negative and the inner one is positive. The entrance slit (with width ω_1) and exit slit (with width ω_2) are centered on the mean radius Ro,

$$Ro = (R_1 + R_2) / 2. \qquad (2.12)$$

The trajectory of an electron in the analyzer depends on its kinetic energy and the applied potential difference across the hemispheres. The condition for an electron of kinetic energy E_0 to pass through the analyzer is given by:

$$e\Delta V = E_0 (R_2/R_1 - R_1/R_2). \qquad (2.13)$$

Thus at a given potential, only electrons with kinetic energy E_0 (pass energy) will follow a trajectory which will bring them to the entrance slit of the detector where they are counted [88]. The detector is constructed from two channel plates in a chevron array to give 18 discrete microchannels, which act as individual electron multipliers. The voltage across the plate is set to allow count rates at above $10^7 \, s^{-1}$.

The relative resolution of the concentric hemispherical analyzer (ΔE_{spec}) given by:

$$\Delta E_{spec} / E_0 = (\omega_1 + \omega_2) / 4 \, Ro + \alpha^2 / 4. \qquad (2.14)$$

where α is half the entrance angle to the analyzer. Since ω_1, ω_2, Ro, and α are set by the spectrometer construction, the resolution can be varied only by changing the pass energy E_0. Equation (2.14) makes clear that the smaller E_0, the better the resolution. However, as

the pass energy is reduced, the signal intensity drops, so a balance is needed between requirements of high signal intensity and high analyzer resolution. In the work presented, a pass energy of 192 eV is used for the survey scans while 48 eV is used for measuring the high-resolution narrow scans.

The experimental resolution for a photoelectron peak is defined by its width (FWHM), which depends on the broadening from the X-ray source (ΔE_{source}), the electron energy analyzer (ΔE_{spec}), and the natural width of the core level (ΔE_{line}) according to:

$$\Delta E_{total} = (\Delta E^2_{source} + \Delta E^2_{spec} + \Delta E^2_{line})^{1/2}, \qquad (2.15)$$

provided all contributions have the Gaussian form [79].

The kinetic energy of the photoelectron measured in the spectrometer (E_k') is referenced to the spectrometer's vacuum level, while the binding energy of the electron inside the sample (E_b) is referenced to the Fermi energy of the sample. For a conducting sample in electrical contact with the spectrometer, the Fermi energies of the sample and spectrometer are equal and the measured binding energy can be expressed as [89]:

$$h\nu = E_b + E_k' + W_{sp}, \qquad (2.16)$$

where W_{sp} is the work function of the spectrometer. W_{sp} is determined by calibration with a measurement on a standard gold sample, with the Au $4f_{7/2}$ line referenced to 84.0 eV binding energy [78]. This line is chosen because of its high intensity and accurately known position. Also, because gold is an inert metal, its binding energy should not be influenced by chemical shifts or charging effects. For insulating samples, positive charge can build up on the surface, and hence the energy referencing needs some modification. In this work, for such situations, the C 1s peak associated with adventitious hydrocarbon contamination is set at 285.0 eV binding energy.

2.3 Thermo Electron Microlab 350

The Auger spectra and some scanning electron micrograph (SEM) images presented in this thesis were obtained with a Thermo Electron Microlab 350 system, for which a schematic is shown in Figure 2.9. More detailed information about this system is to be found in the Microlab 350 Operating Manual [90]. The Microlab 350 is equipped with a Schottky field emission electron source used in combination with the hemispherical energy analyzer for Auger electron measurement. In addition, it is also equipped with a number of detectors for measuring secondary electrons (SED), backscattered electrons (BSD), and X-rays (EDX). An Ar^+ ion gun is also available for surface cleaning and depth profiling.

The Microlab 350 system has a transfer chamber for sample entry, a preparation chamber for sample treatment, and an analysis chamber for electron spectroscopy. Sample transfer between the chambers is done with wobble sticks and a rack-pinion transfer rod. The analysis chamber operates under UHV conditions with a base pressure of 1.5 x 10^{-9} Torr, and the pumping arrangement for the whole system is indicated schematically in Figure 2.9.

Figure 2.10 shows a schematic diagram for the field emission electron gun. The field emission tip is made of a single crystal tungsten wire (radius <1 µm) which is coated with zirconium and welded on to a tungsten heater filament used to resistively heat the tip (~1800 K). Application of a potential creates an electric field (10^7 Vcm^{-1}) at the tip which causes electrons to be emitted. As shown in Figure 2.9, the source is differentially pumped by an ion pump in order to avoid contamination and maintain a
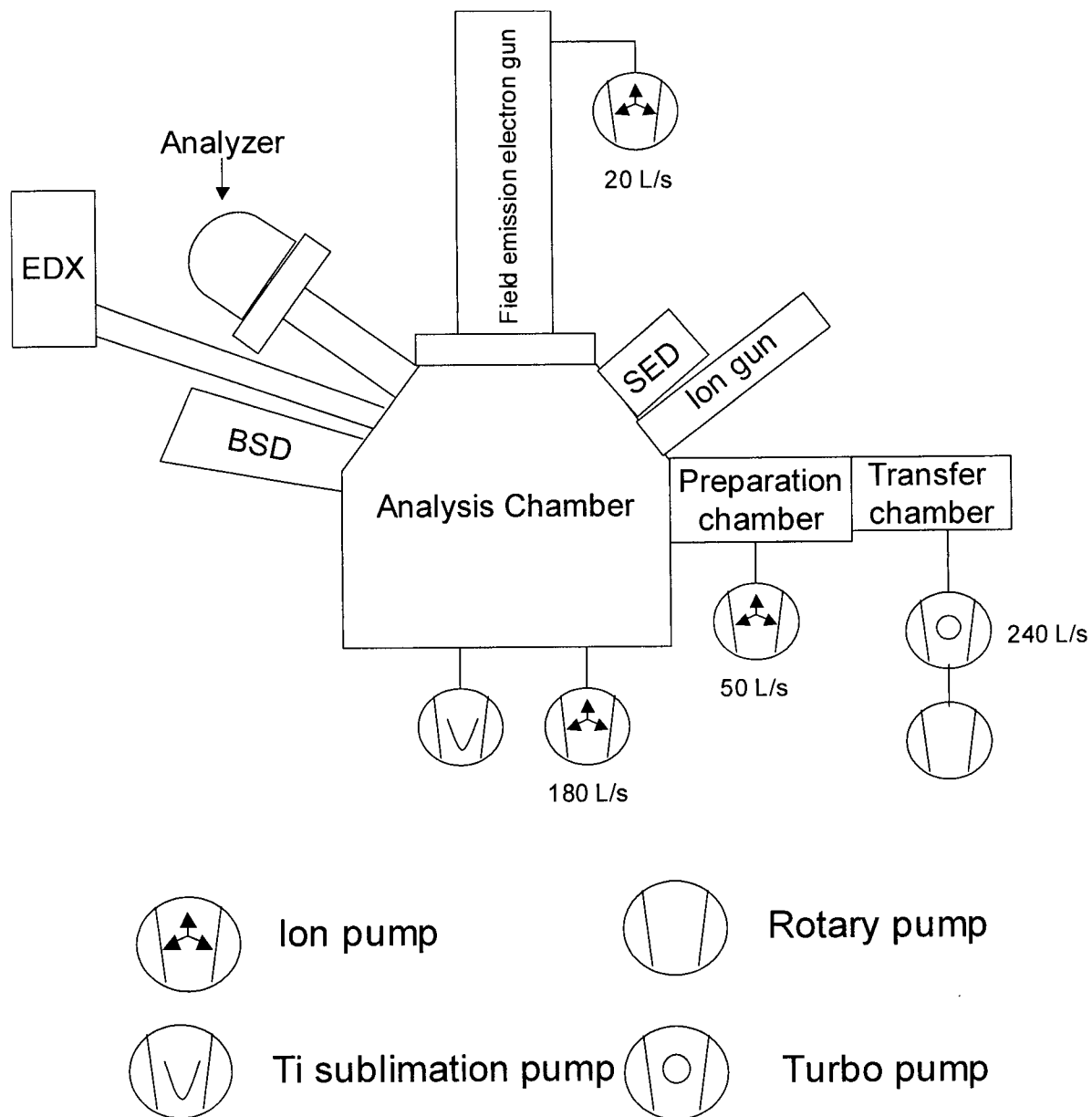
Figure 2.9. Schematic indication of pumping system for Microlab 350.

filament
suppressor
extractor
lens
gun aperture
upper scanning coils
lower scanning coils
stigmator coils
objective coil
objective aperture
sample
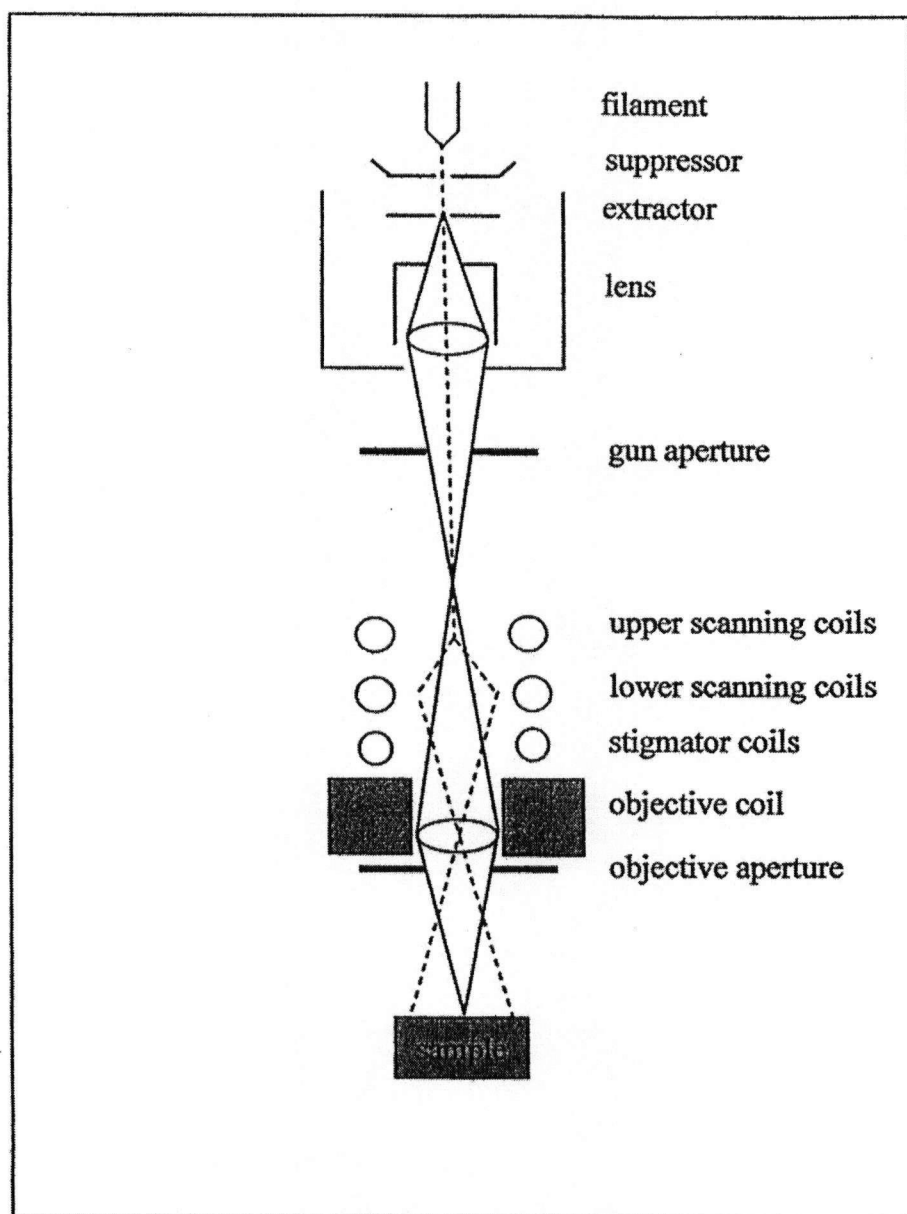
Figure 2.10. Illuminating system in Microlab 350 [13].

stable operation of the beam. When the electrons are extracted from the field emission tip, they are focused ($\leq$10 nm) by a system of electromagnetic lenses and apertures schematically shown in Figure 2.10. This source provides high brightness (5×10^8 A/cm^2 steradian), low energy spread of 0.3 eV, and long life time (~5000 h), when operated under the low-pressure operating condition.

The basic principle of the hemispherical energy analyzer was outlined in Section 2.2.2. The Microlab 350 analyzer is operated in the constant retarding ratio (CRR) mode, in contrast to the constant analyzer energy mode (CAE) used in XPS. In the CRR mode, the pass energy is varied to maintain a constant E / E$_0$ ratio. The advantage of this mode is that it offers good resolution at low kinetic energy, where a number of Auger peaks of interest occur. But, on the other hand, the resolution reduces as the energy increases, a point that is often considered less serious because Auger peaks tend to be broader than photoelectron peaks. The electron detection system in the Microlab 350 consists of six-parallel-connected channeltrons, and the analyzer can be set to detect either a particular element of interest, or programmed for sequential detection of several signals. The electron beam can be focused to one spot for point analysis and this method has been used for analysis of microstructures in Chapters 4 and 5. Although not used in this research, the Microlab 350 also has capabilities to measure line profiles (incident beam is systematically moved along the line), two-dimensional maps (beam is rastered over a surface area), and three-dimensional analysis where two-dimensional images are combined with depth profiling.

The process of Auger analysis consists in first using the focused electron beam to obtain a SEM image for the area of interest. In this process, the electron beam is rastered

across the sample surface to collect secondary electrons (up to 50 eV) by the photomultiplier detector. A SEM image gives topography information (three-dimensional appearance) for the surface, with the brightness of the signal at any point depending on the nature of the surface area and atomic number of the elements. In the absence of surface charging, steep surfaces tend to be brighter than flat surfaces and also higher atomic numbered elements have a greater yield of secondary electrons than those of low atomic number. Once the SEM image is obtained, the incident electron beam is focused on the particular micro-areas of interest and Auger measurements are obtained using the hemispherical analyzer.

2.4 Other Instrument for SEM

Some SEM images were measured in this work before the Microlab 350 became available, and those micrographs were generated by the Hitachi S4100 (in AMPEL) and the Hitachi S3000N (in the Department of Materials Engineering). The Hitachi S4100 SEM has a field emission source with an energy spread 0.2-0.3 eV and brightness of 10^9 A/cm^2 steradian. The Hitachi S3000N instrument is equipped with a tungsten hairpin filament source operated around 2700 K that produces electrons by thermionic emission. This type of source can be operated at higher pressure (10^{-5} Torr) in comparison to the field emission source, but it gives lower brightness (10^6 A/cm^2 steradian), higher energy spread (1.0 eV) and shorter lifetime (e.g. 60-200 h) [91]. In addition, the Hitachi S3000N is equipped with backscattered electron and X-ray detectors, both of which were used for measurements in Chapter 5. Backscattered electrons undergo only a few scattering events to emerge from the specimen at an energy comparable to the primary beam [91]. The

measurement of backscattered electrons can yield information about the distribution of different elements due to atomic number contrast.

2.5 Energy Dispersive X-ray Spectroscopy

2.5.1 Introduction

Energy dispersive X-ray (EDX) spectroscopy measures X-rays emitted from a sample after it has been irradiated with an energetic electron beam, according to the process in Figure 2.1(c). Since each atom type has its own set of core energy levels, a measurement of the photon energies in a EDX spectrum can be used to identify the elements in a sample tested. EDX spectroscopy has been used in this thesis to assess the chemical composition at different micro-areas of uncoated AZ91-Mg alloy samples, and a spectrum is shown in Figure 2.11 where it is displayed as counts per second on the vertical axis and energy (keV) on the horizontal axis. The peaks are labeled according to the core level involved (e.g. Mg_K), with a further distinction when more than one transition can occur for a particular core level (e.g. $Mn_{K\alpha1,2}$, $Mn_{K\beta}$). The peak energies are identified by comparing with an X-ray emission database available in the system.

The background to the use of EDX for quantitative analysis is discussed in basic reviews of the subject [92-95]. The analysis depends on measuring peak area after application of a non-linear background correction, and comparisons are made against standard specimens of known composition with the elements in similar states to the sample being analyzed. The basic expression for the amount of element i present in a sample (C_i) is:

$$C_i = k_i\, I_i/I_{(i)}, \qquad\qquad (2.17)$$
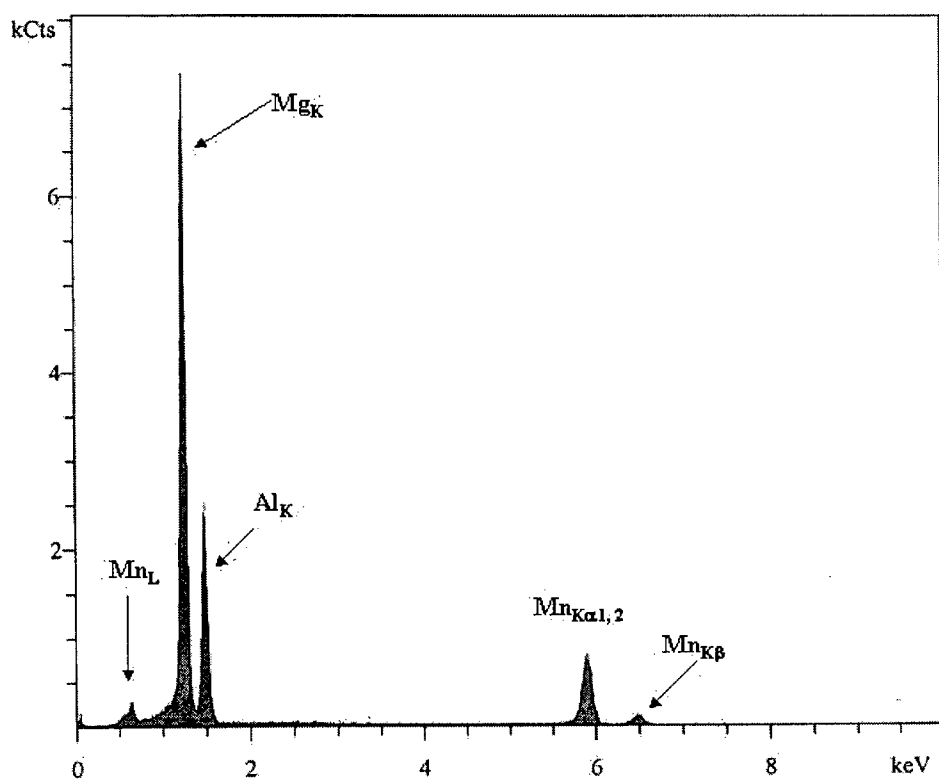
Figure 2.11. EDX spectrum measured from the particle region of an AZ91-Mg alloy.
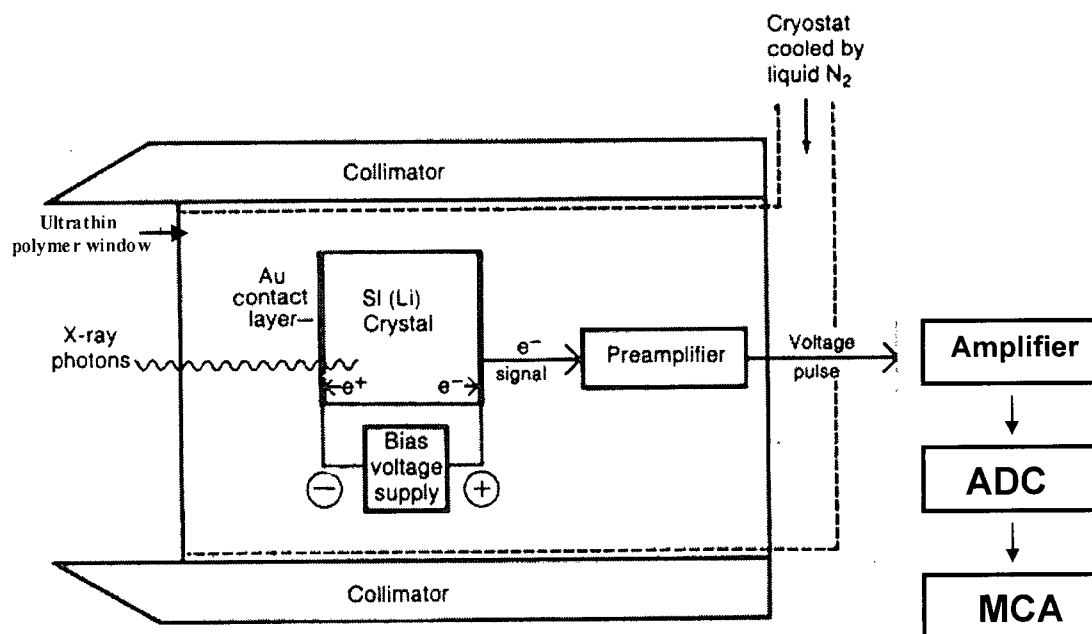
Figure 2.12. Schematic for X-ray detector (modified from Ref. [18]).

where $I_{(i)}$ is the corrected peak area from a standard composed only of element i, I_i is the area measured from the specimen under analysis, and k_i is a correction factor (normally referred to as ZAF factor [94-95]) that corrects for effects of atomic number, self-absorption, and fluorescence probabilities for the different elements. Because energetic electrons (e.g. 20 keV) are used to excite the process, and the photons produced have long mean free paths (compared with electrons), EDX gives elemental composition from depths of several μm. Therefore, compared with XPS and SAM, EDX is a bulk analysis technique.

2.5.2 EDX Instrumentation

Figure 2.12 indicates a schematic for the X-ray detector. The Hitachi S3000N instrument is equipped with a AP3 Ultrathin Polymer X-ray window (Moxtek Inc.) [96] which (unlike the conventional Be window) allows for transmission of photons from light elements (atomic number less than 10). X-rays from the sample pass through this window and strike a lithium-doped silicon diode detector which is biased (1000 V) in order to establish a depletion zone. The number of electron-hole pairs generated for a given photon is proportional to the X-ray energy and the energy selection in the diode is achieved by the difference in drift time for the electrons. The signal corresponding to a specific energy is amplified, converted to digital form by the analog-to-digital converter (ADC), and put into the appropriate channels of the multichannel analyzer (MCA) [92].

2.6 Secondary Ion Mass Spectrometry

2.6.1 Introduction

The process of secondary ion mass spectrometry (SIMS) is shown in Figure 2.13. The process involves a primary ion beam of a known energy (0.5 to 8.0 keV) bombarding the surface and passing energy to target atoms in a series of collisions (a "collision cascade") during which secondary ions (along with neutral species) are sputtered from the surface [97]. The SIMS experiment involves detecting the charged ions by a mass spectrometer, which measures intensity as a function of mass-to-charge (m/z) ratio.

Figure 2.14 shows a typical SIMS spectrum measured in a low-resolution quadrupole instrument from a high-purity Al sample that has been coated with BTSE. In that example, fragments at values 27, 28, 70, and 71 are identified, and that starts some background for work described in Chapter 3. Mass resolution in SIMS is defined in terms of m/Δm where 'm' is the nominal mass and Δm is the peak width at FWHM. The resolution of the $^{28}Si^+$ peak shown in the spectrum in Figure 2.14 is around 140. The main advantages of the quadrupole instrument are low cost and light weight, but it suffers from low mass resolution. Furthermore, this type of analyzer is a scanning instrument so that it only allows the sequential transmission of ions, all other ions being discarded [79, 98]. Higher mass resolution and transmission are obtained using time-of-flight SIMS (TOF-SIMS), which is used in Chapter 4, where the resolution for the $^{28}Si^+$ ion is around 8000. For this instrument, the primary source is pulsed in order for it to be compatible with the time-of-flight detector.

Two main analysis modes used for SIMS measurements are the static and the dynamic modes, and they are distinguished by the ion dose of the primary beam [99-101].
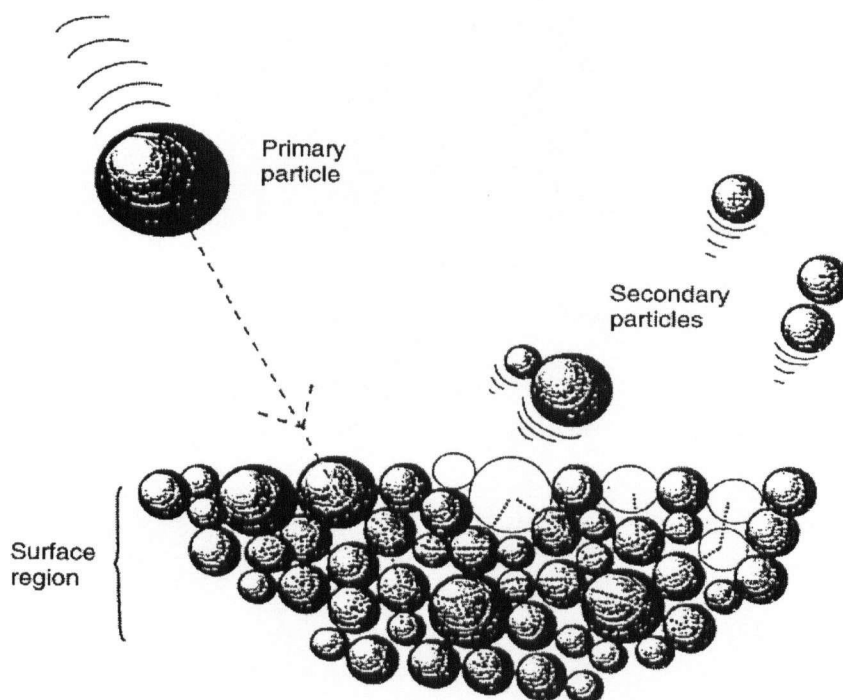
Figure 2.13. Sputtering process in SIMS [2].
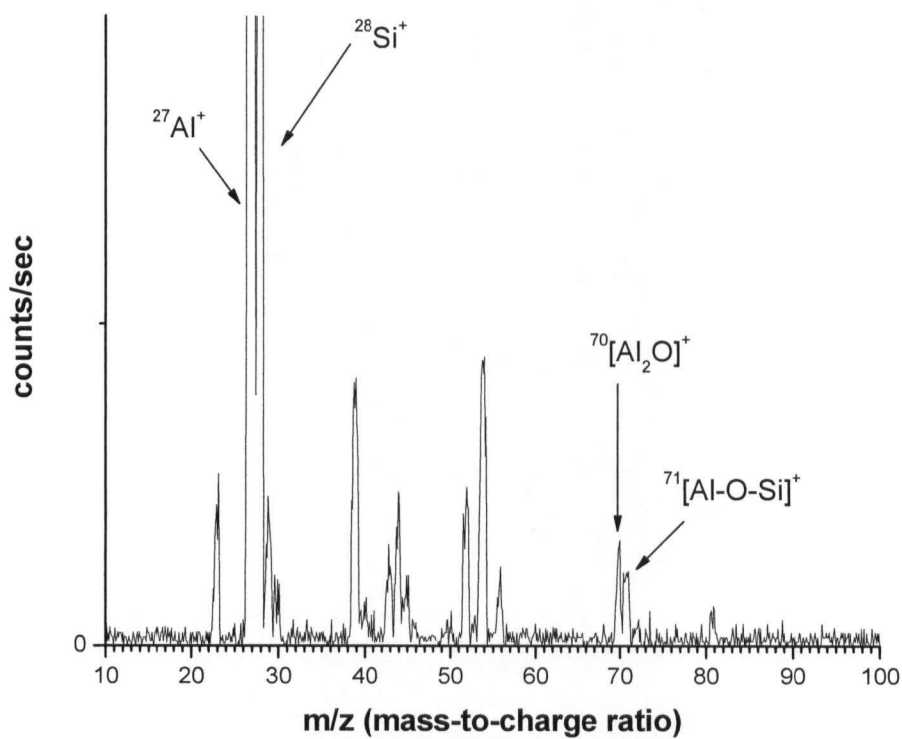
Figure 2.14. Quadrupole positive ion spectrum from a high-purity Al sample which had been acid etched for 10 min and then coated with 1% BTSE.

In static SIMS, a low primary ion dose ($<10^{13}$ cm^{-2}) is used and this allows for the measurement of the surface layer without significant modification. An extension is to measure the distribution of ion species from across a surface to give imaging SIMS. For dynamic SIMS, higher primary ion doses are used ($> 10^{13}$ cm^{-2}) to physically peel off the surface layers to give information on the depth distribution of elements. When combined with the ion imaging capability, dynamic SIMS can provide three-dimensional analysis for a sample.

One major challenge in SIMS is to convert secondary ion signals to concentrations within the sample. Care is needed because the secondary ion yield can vary with the chemical state of the element being analyzed [79, 101, 102]. For example, the positive ion yield for Al increases by a factor of 10^2 after oxidation [103]. Such considerations of matrix effects must be included in the design of experiments which aim to give semi-quantitative information.

2.6.2 VG MM12-12S

Figure 2.15(a) gives a schematic indication of the VG Scientific MM12-12S instrument used for the SIMS work in Chapter 3. The main chamber and the transfer chamber are separated by a gate valve. After loading a sample, the transfer chamber is pumped down to 10^{-8} Torr before the gate value is opened for transfer into the analysis chamber using a wobble stick. The sample position during the transfer process is controlled by a manipulator located in the analysis chamber. The pumping system is shown in Figure 2.15(b). Base pressures for the analysis chamber, transfer chamber, and the duoplasmatron ion source are 5 x 10^{-10}, 7 x 10^{-9}, and 2 x 10^{-7} Torr respectively.

(a)

Quadrupole mass filter

Ar gun

Duoplasmatron ion gun

Ga gun

Transfer chamber

Stage manipulator

Transfer rod

Photomultiplier and scintillator

Wobble stick

Analysis chamber

Ti sublimation pump

(b)

Duo gun

Analysis Chamber

Transfer Chamber

Gas Manifold

150 L/s

600 L/s

150 L/s

Rotatory pump

Ti sublimation pump

Diffusion pump

Valve
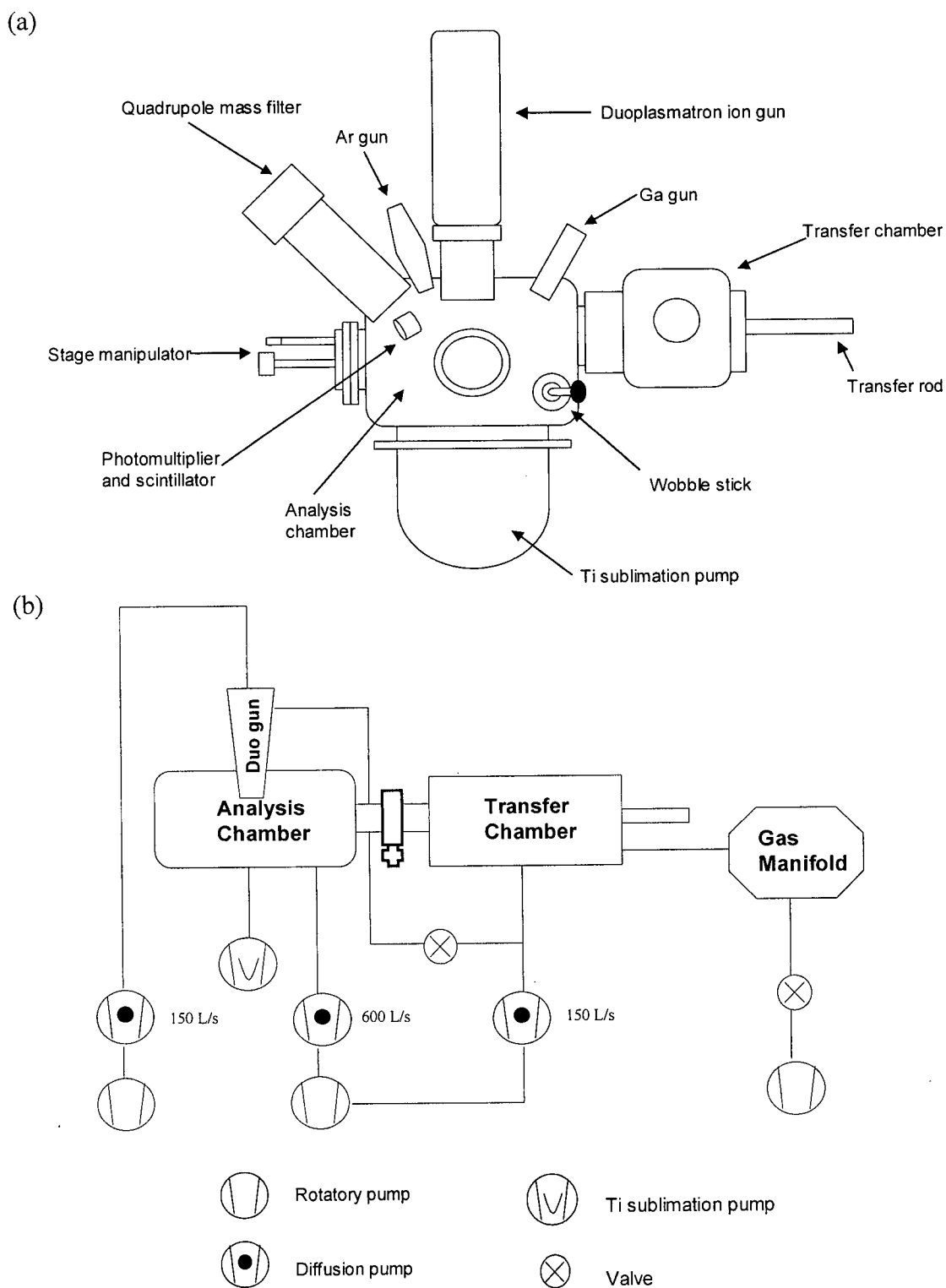
Figure 2.15. VG quadrupole SIMS system: (a) analysis chamber with facilities, (b) schematic of pumping system.

This instrument has three ion sources: the gallium liquid ion source (MIG100), the duoplasmatron ion source (DP5B), and the argon ion source (AG61). The duoplasmatron source (with argon gas) was used for the work presented in Chapter 3; it produces primary ions by plasma arc discharge (300-600 V applied between the cathode and anode), and an opening in the anode allows ions to be extracted, and then accelerated to 5 kV [104, 105]. The ion beam is transmitted through a mass filter (Wien filter) in order to filter out impurities; the beam diameter can range from 1 to 100 μm.

The first step after sputtering from the sample is to suppress fast ion/neutrals and photons by an ion energy filter. The quadrupole mass analyzer acts as a mass filter in the range 1 to 800 amu. It has two pairs of molybdenum rods (diameter 12 mm), where opposite pairs of rods are connected electrically (Figure 2.16): the sinusoidal potentials applied to each set of rods are equivalent, but of opposite sign:

$$\phi(t) = U + V\cos(2\pi ft) \qquad (2.18)$$

$$\phi(t) = U - V\cos(2\pi ft). \qquad (2.19)$$

For a given set of voltages, only ions with a particular mass-to-charge ratio can pass through the analyzer to be detected; the other ions strike the rods and are neutralized [106]. Mass scanning is achieved by keeping both the V/U ratio and f (e.g. 2 MHz) constant while varying U and V (in typical ranges to 100 V and 1500 V respectively). The ion detector is a single channeltron multiplier (with a gain of 10^8).

2.6.3 ION TOF IV

The ION TOF IV instrument at the University of Toronto is equipped with multiple ion sources: gallium gun, cesium gun, and electron impact gas ion source (for
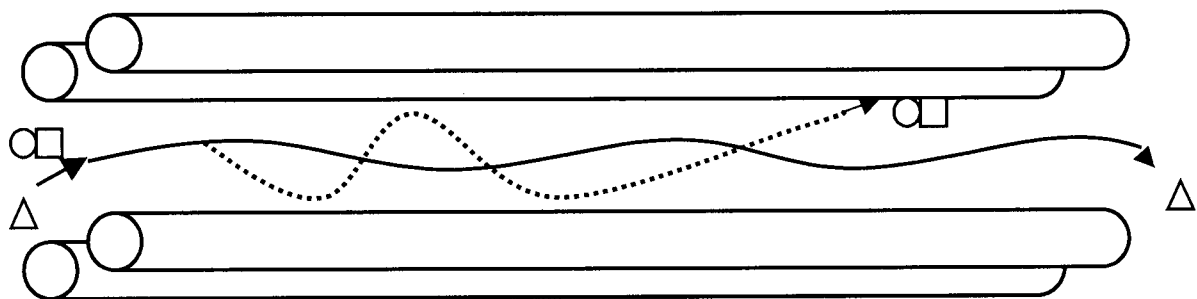
Figure 2.16. A schematic of the quadrupole mass analyzer.

Ar, O_2 and SF_6). For the work presented in Chapter 4, the gallium source was used for measurements in conjunction with the SF_6 source that was used for sputtering.

A schematic of the TOF-SIMS instrument is shown in Figure 2.17 where the gallium liquid metal ion gun is the main analytical gun. This gun supplies good spatial resolution, where the ion beam size width is typically 0.5 μm [98]. The main components of the gun are the Ga source (Ga reservoir and needle), the heater, the extractor and the optical lenses (Figure 2.18). The Ga metal melts at 38°C, and when the reservoir is heated with a current of 1 A for ~15 min, the metal melts and wets the needle. With a potential difference of 4 kV applied between the source and extractor, ion emission occurs from the edge of the needle, and the beam is focused and adjusted by the optical lenses. The pulsing of the gun is achieved by rapid deflection of the primary ion beam by an applied electric field.

This Ga gun can be operated in different modes depending on whether the objective is to obtain high mass resolution or imaging resolution, and a compromise must be reached between them. The bunched mode in TOF-SIMS uses a short pulse of about 600 ps for high mass resolution, whereas the imaging mode requires longer pulse times (e.g. 20-100 ns) for good spatial resolution (but nominal mass resolution). In principle, a balance is reached in the burst mode [107], which uses a pulse time of 1.5 ns, but we were not able to get it to work satisfactorily for the experiment described in Chapter 4.

After the ions have been sputtered from the sample, they are accelerated by the extractor (Figure 2.17) to a fixed potential (in the range 3 to 8 keV) such that all ions possess the same kinetic energy zV [79]:

$$\frac{1}{2}mv^2 = zV, \tag{2.20}$$
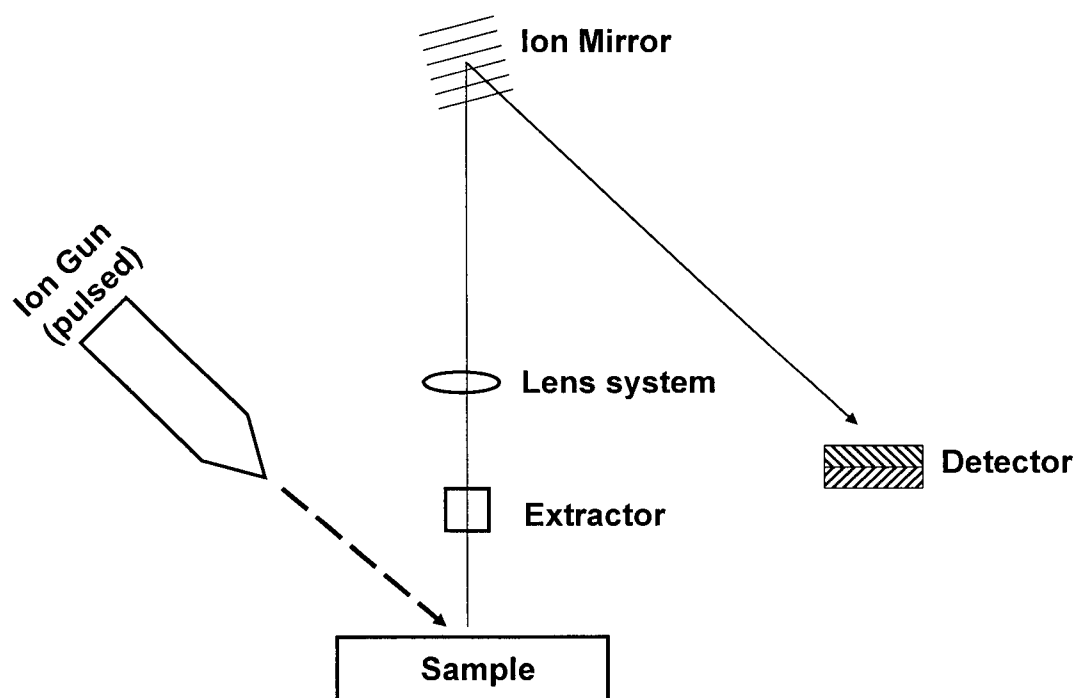
Figure 2.17. A schematic diagram of a TOF-SIMS instrument.
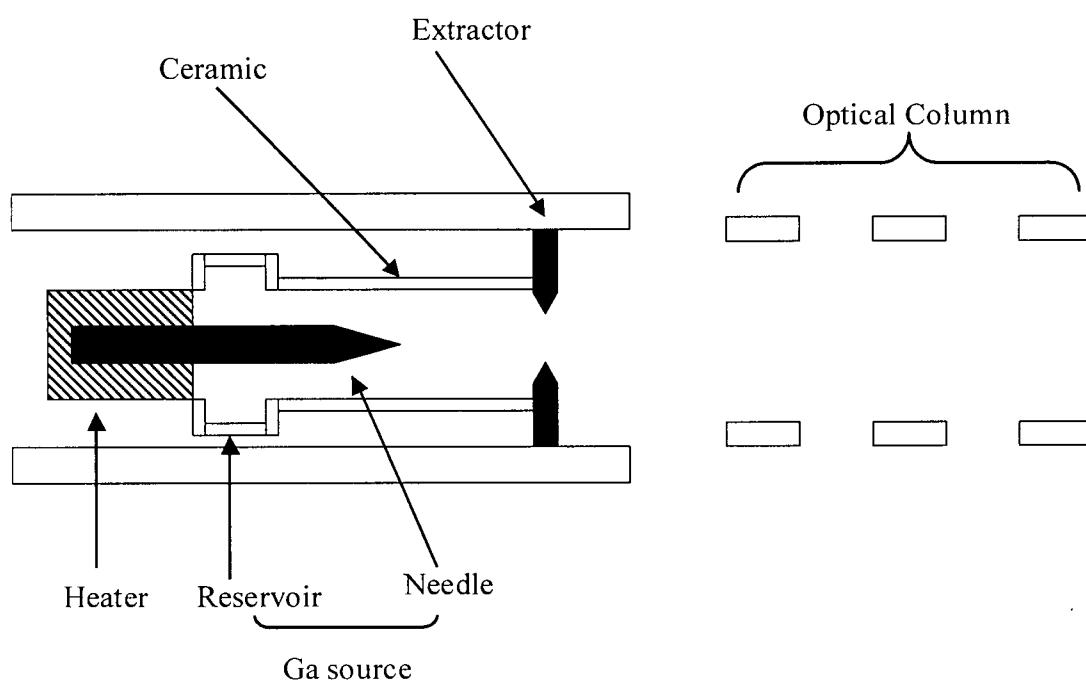
Figure 2.18. Ga source in ION TOF IV.

where m is the mass, v is the velocity, z is the charge and V is the acceleration voltage. Ions of different masses have different velocities at a given kinetic energy. For example, heavier ions have slower speed and hence longer flight times. Thus the measurement of flight times of ions can be converted to their masses, and that is accomplished in the time-of-flight analyzer by timing ion paths from the extractor to the detector. On this path, the ions are focused by the lens system and travel to the ion mirror where they are reflected to the microchannel detector system.

The cycle of measuring the flight times is repeated at a rate set by the flight time for the highest mass to be recorded. The pulsing of the gun is timed with the extractor such that they are both switched off during the drift time of the ions being measured. The next pulse of primary ions does not start until the secondary ions from the previous pulse have cleared the analyzer. This drift time for the secondary ions provides an interval during which the low energy ion beam (e.g. SF_6) can be used for sputtering, so that analysis and sputtering can in effect be done simultaneously (the dual beam mode).

Chapter 3 Interfaces Between Organosilanes and Oxidized Al [†]

3.1 Introduction

The discussion in Chapter 1 has suggested that organosilanes have potential applications to protect metals against corrosion, with BTSE (Table 1.1) of special interest. Surfaces of aluminum and its alloys require initial modification in order to optimize their structures and compositions to aid the coating process. The sulphuric-chromic acid (FPL –Forest Products Laboratory) surface pre-treatment has been widely used in industry to prepare such surfaces [42, 59]. It is believed that the FPL process prepares the aluminum surface for silane adsorption chemically, by etching away the looser native oxide layer, followed by oxidation of the subsurface aluminum to form a more compact oxide layer on the surface. Meanwhile, this new-born aluminum oxide can be protonated to produce the hydroxyl groups (Al-OH) which can in principle react with silanol groups (Si-OH), from the hydrolyzed silane, to form Al-O-Si interfacial bonding via a condensation process [36, 38]. The FPL treatment produces an oxide morphology that consists of a "whisker" like structure, roughly 400 Å in diameter and 400 Å high, which is believed to enhance the silane adhesion by the interlocking mechanism [59, 108, 109].

In principle, the optimal coating conditions may vary with the underlying microstructure, and in general it should be useful to have a methodology for choosing an

---

[†] The content in this chapter using the 7075-Al alloy has been published as J. Kim, M. Teo, P.C. Wong, K.C. Wong, K.A.R. Mitchell, Pre-treatments applied to oxidized aluminum surfaces to modify the interfacial bonding with bis-1,2-(triethoxysilyl)ethane (BTSE) Part II. Anodized 7075-T6 Al alloy, Appl. Surf. Sci. 252 (2005) 1305. The material involving high-purity Al was done in collaboration with M. Teo and has been published as M. Teo, J. Kim, P.C. Wong, K.C. Wong, K.A.R. Mitchell, Pre-treatments applied to oxidized aluminum surfaces to modify the interfacial bonding with bis-1,2-(triethoxysilyl)ethane (BTSE) Part I. High-purity Al with native oxide, Appl. Surf. Sci. 252 (2005) 1293.

appropriate pre-treatment according to the nature of the particular surface at hand. The work described in this Chapter is part of an exploration to meet this objective. It uses several surface analytical techniques in an attempt to help strengthen our understanding of the processes involved in the FPL pre-treatment and subsequent coating. Such information should help shape the design of improved coating procedures for different surfaces. Two samples are considered in this study: a high-purity Al sample and an anodized 7075-Al alloy. The high-purity Al sample is chosen in order to gain an initial understanding of the factors that affect the BTSE coating process without the complications of chemical heterogeneity at an alloy surface. The 7075-Al sample was chosen as it was likely to contrast with the high-purity sample in two main respects: (i) the nature of the oxide is different, being both thicker and probably more porous [23], and (ii) there may be differences resulting from the chemical heterogeneity at the alloy-to-oxide interface. The objective is to identify pre-treatment conditions that help maximize the adhesive bonding of BTSE for these two types of Al surfaces.

BTSE is chosen for this work because it is a non-functional silane with up to six silanol groups per molecule after hydrolysis, and this increases the probability of Al-O-Si bond formation when compared to organofunctional silanes such as γ-APS and γ-GPS. In addition, use of the non-functional silane simplifies the coating process due to the absence of "upside down" bonding that may occur with organofunctional groups [35].

The key characterization methods used in this work are secondary-ion mass spectrometry (SIMS) to identify the Al–O–Si bonding, X-ray photoelectron spectroscopy (XPS) and scanning electron microscopy (SEM) to analyze chemical and topographical

changes to the surfaces, and an ultrasonic rinse test is used to give an initial assessment of the strength of the adhesive bonding.

3.2 Experimental

High-purity Al samples (Puratronic, 99.997%) of 0.1 mm thickness, and chromic acid anodized 7075-T6 Al alloy samples (approximate minority components: 6 wt% Zn, 3 wt% Mg, 2wt% Cu, 0.5 wt% Fe, 0.4 wt% Si, 0.3 wt% Mn and 0.2 wt% Ti, supplied by Department of National Defence of Canada), 0.12 cm thick, were cut into 1 cm^2 square panels and then degreased in acetone for 30 min followed by 5 min of DI water rinse. After the rinse, various high-purity Al and 7075-Al samples underwent the FPL process for varying times. In this treatment, samples were immersed in an agitated solution consisting of 60 g/L sodium dichromate dihydrate (Sigma Aldrich) and 17 vol% concentrated sulphuric acid at the temperature of 65°C for different times. After the FPL pre-treatment, each sample was rinsed in DI water (5 min) before undergoing further surface pre-treatments or characterization procedures. In addition, observations are presented for a 7075-Al sample that underwent successive treatment of 5 min FPL and 1 h exposure to a H$_2$ plasma. For the H$_2$ plasma treatment, a stream of hydrogen at pressure 2 Torr was excited in an electrodeless discharge by means of microwave generator operated at 2.45 GHz with a total power of 60 W. The sample was placed in a reaction chamber and set 20 cm away from the front end of the hydrogen plasma luminous zone. The operating pressure was monitored by a Pirani gauge positioned 50 cm downstream from the sample. After 1 h of the hydrogen plasma exposure, the reaction chamber was

taken back to atmospheric pressure under dry N_2, and the sample was immediately immersed into the BTSE coating bath.

The 1% BTSE coating solution was prepared by mixing 1 vol% BTSE (96% purity, Aldrich), 93 vol% methanol (HPLC grade, Fisher Scientific), and 6 vol% distilled water. The solution was then stirred for 5 h at room temperature to ensure complete hydrolysis of the BTSE. Following the described pre-treatments, each sample was immediately immersed into a hydrolyzed 1% BTSE coating bath for 2 h. With the exception of samples undergoing SIMS analysis, where coated samples were immediately rinsed in distilled water for 5 min to minimize the BTSE polymerization, all coated samples were subjected to XPS analyses after drying.

X-ray photoelectron spectroscopy (XPS) was performed using a Leybold MAX200 spectrometer. Spectra were recorded using the MgKα source (1253.6 eV) operated at 10 kV and 20 mA. The operating pressure was 1.5×10^{-9} Torr and the collection area was 4×7 mm^2. The survey spectra were obtained with the analyzer pass energy set at 192 eV and the higher resolution scans for the Al 2p and O 1s spectra were obtained with a 48 eV pass energy. The high-resolution spectra were calibrated with reference to the Al 2p metal peak position, set at 72.65 eV in order to protect against effects due to charging. For 7075-Al alloy samples that were studied with XPS and received less than 5 min of the FPL treatment, the calibration of binding energy used the C 1s peak associated with adventitious hydrocarbon contamination set at 285.0 eV.

Secondary ion mass spectroscopy (SIMS) analyses were achieved using a VG MM12 – 12S quadrupole mass spectrometer equipped with a duoplasmatron ion gun for producing the Ar$^+$ primary beam (5 keV, ion dose 1.3×10^{13} ions cm^{-2}) used for the

measurements. SIMS spectra could not be detected from 7075-Al samples FPL treated for less than 5 min, due to sample charging, but for samples FPL treated for longer than 5 min, no charging problems were detected with SIMS.

SEM micrographs for high-purity Al and 7075-Al samples were measured using the Hitachi S-4100 and Hitachi S3000N scanning electron microscopes respectively. Since the 7075-Al samples started with a thick oxide layer some extra precautions were needed in relation to sample charging; specifically the SEM micrographs were recorded after coating by a thin layer of gold in order to increase the conductivity.

In order to examine how well the coated BTSE film adhered to the pre-treated aluminum surfaces, a combination of XPS and water ultrasonic rinsing test was conducted. FPL treated samples after being coated with the BTSE first underwent XPS analysis. After the XPS analysis, the samples were then subjected to the rinsing test where samples were exposed for 30 min in distilled water in a sonication bath (Solid State/Ultrasonic T14B, L&R Manufacturing). Each sample was then dried in nitrogen prior to undergoing its second XPS measurement, which immediately identified the degree of de-adhesion as a result of the sonication test.

3.3 Results and Discussion

3.3.1 Methodology Used

3.3.1.1 SIMS Analysis

The presence of Al-O-Si bonding in this work has been followed with the mass fragment at nominal mass 71 amu ($AlOSi^+$) in the positive SIMS spectrum. Recent work by Abel et al. [66, 110] with the time-of-flight SIMS (TOF-SIMS) technique has shown

that the nominal mass of 71 can be due to various sources such as hydrocarbon contamination, but that study also reported that after the outer layer had been sputtered off to reach the interface region, the peak at mass position of 71 amu was indeed due to the $AlOSi^+$ ion. The presence of the Al-O-Si bonding at the silane-aluminum interface has also been confirmed by another TOF-SIMS study by Bexell et $al.$ [67]. Even though the quadrupole SIMS used in this work has lower resolution than the TOF-SIMS technique, with the previous studies done by TOF-SIMS (and more reported in Chapter 4), we believe that it is reasonable to assign the nominal mass at 71 amu to the $AlOSi^+$ ion fragment as long as the analysis applies to the actual silane-aluminum interface. Thus after the samples had been coated with BTSE, they were rinsed immediately with distilled water to avoid formation of a thick BTSE polymer layer on the surface, and care was taken to gently sputter the outer layer to avoid ion fragments from hydrocarbon contamination. The $AlOSi^+$ signal was monitored as a ratio of peak intensities at 71 and 70 amu, where that at 70 amu corresponds to the species Al_2O^+ which is assumed to arise from the oxidized surface.

Investigation of the BTSE coated surface began by performing a depth profile for each sample, measuring the $[AlOSi]^+/[Al_2O]^+$ (I_{71}/I_{70}) ratio vs. time [111]. An example of such a depth profile is shown in Figure 3.1. It can be observed that the ratio goes through a maximum, and the time associated with the maximum ratio is taken to indicate the depth where the number of OH bonding sites was maximized for the original aluminum oxide surface (thus leading to the maximum amount of Al-O-Si bonding for that interface). Figure 3.2 plots the maximum I_{71}/I_{70} ratio values for the differently FPL-treated samples, and independent measurements from different areas of particular
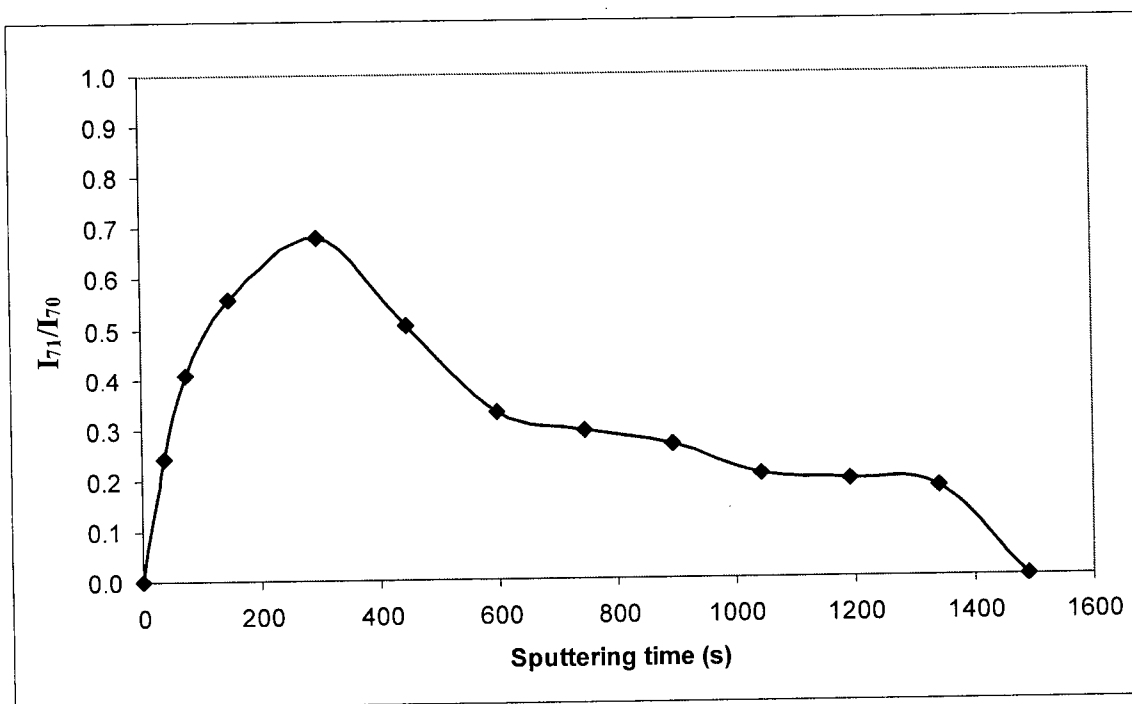
Figure 3.1. SIMS depth profile from a high-purity Al sample coated with BTSE after FPL pre-treatment for 60 min.
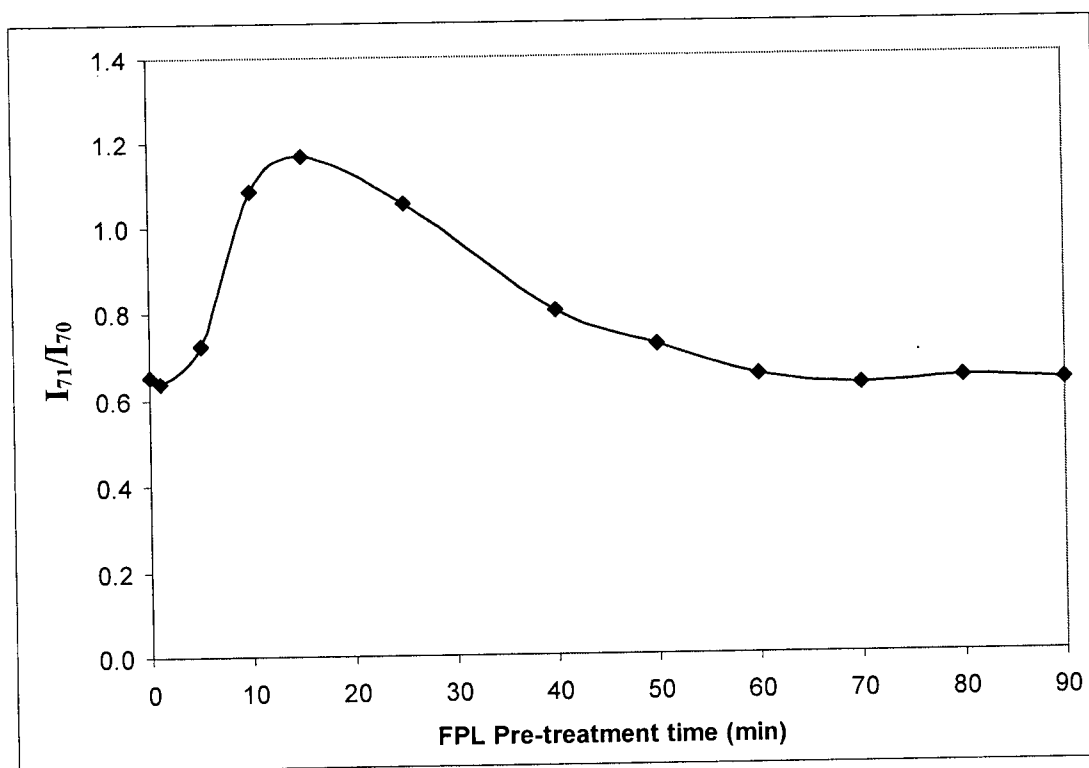
Figure 3.2. Maximal value of I_{71}/I_{70} from peaks in curves like that in Figure 3.1 plotted against FPL pre-treatment time.

samples suggest that the uncertainty in the ratio is about 0.03. A trend is seen where the I_{71}/I_{70} ratio is low when BTSE was applied for short FPL treatment times (<5 min) and the ratio increases for times 5-10 min [111]. The ratio then peaks at pre-treatment times in the 10-25 min range, and steadily decreases back to its initial value over longer times (25-90 min). Apparently the optimal chemisorption between the BTSE and high-purity Al (i.e. direct Al-O-Si bonding) occurs for the FPL treatment in the time range of 10-25 min; accordingly the untreated native oxide of Al (0 min FPL) has less active OH sites than the treated oxide surfaces. The FPL treatment time of 10-25 minutes that was used to obtain the optimal chemisorption, according to this microscopic analysis, is in close correspondence with the normal FPL recipe that has been identified by performance in macroscopic tests [42, 59].

3.3.1.2 XPS and SEM Analyses

Two examples of the use of XPS in combination with the ultrasonic rinsing test to assess the strength of BTSE adsorption on the FPL treated samples are shown in Figure 3.3, where the prominent peaks for Si 2s (binding energy 154.0 eV), Si 2p (102.5 eV), Al 2s (119.0 eV) and Al 2p (74.6 eV) are indicated. The example in Figure 3.3(a) corresponds to a FPL treatment for 1 min, and this is representative of samples that had been pre-treated for short times (e.g. 1-5 min); it is clear that this particular sample has failed the ultrasonic rinsing test (i.e. much of the silane is lost from the surface). The other example in Figure 3.3(b) has been FPL treated for 10 min, and it is representative of samples that have been pre-treated for longer times (e.g. 10-60 min). That example showed a much more strongly adhered silane [111].
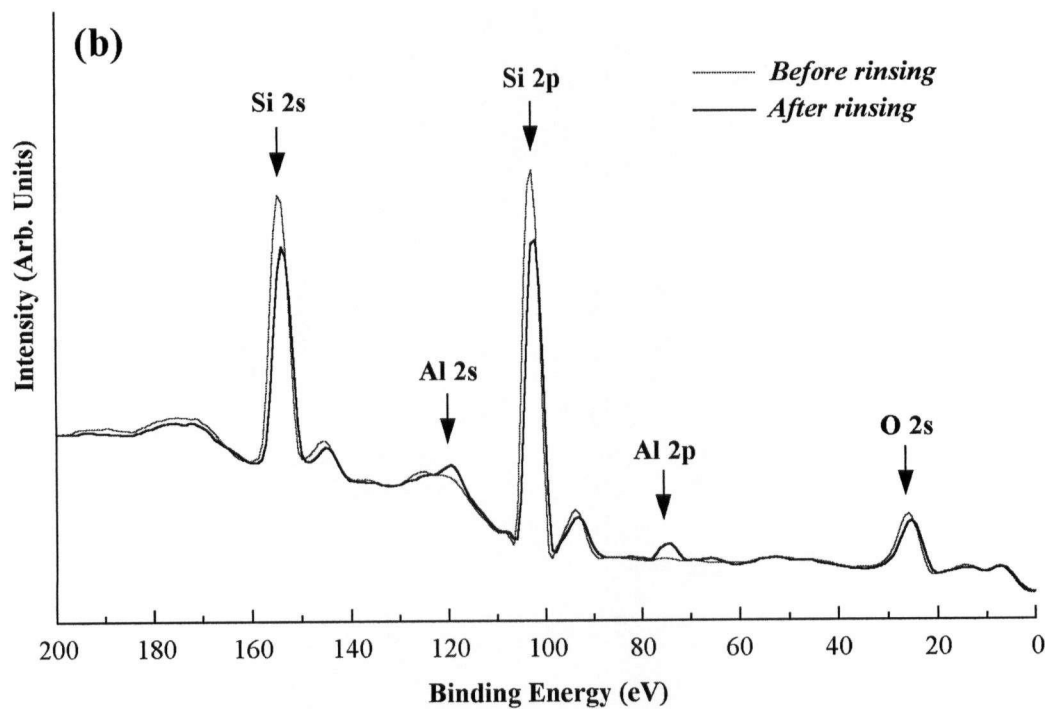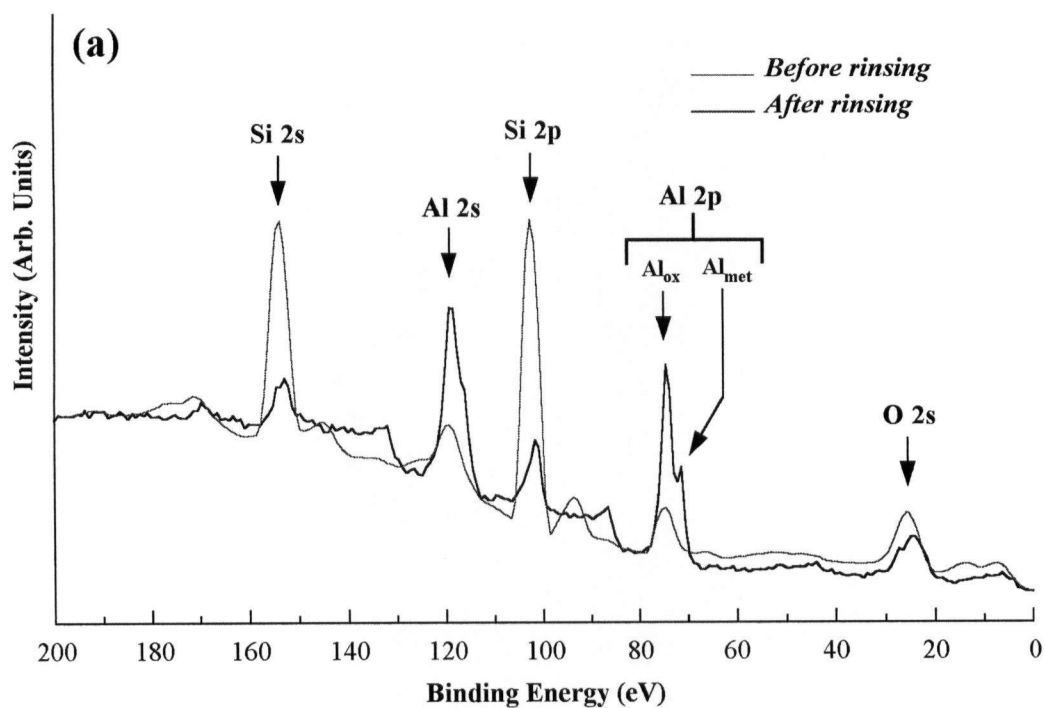
Figure 3.3. XPS survey spectra from high-purity Al samples coated with BTSE before and after the ultrasonic rinsing test. Prior to coating samples were FPL treated for: (a) 1 min, (b) 10 min.

SEM and XPS analyses of the sample prior to coating can be used to offer insights into why the samples FPL treated for shorter times failed the test in comparison to those samples treated longer times. Figure 3.4 shows SEM images of the native oxide and FPL treated surfaces. The initial native oxide (0 min) is flaky in appearance (Figure 3.4(a)) and after 1 min of FPL treatment the surface still suggests that scarring is present, but it appears flatter than the untreated case even if the changes are still fairly small. For the 5 min treatment, small circular structures start to appear and these structures are well defined by 10 min of treatment. These structures have previously been described as having a scallop form [40], and they are believed to result from the new oxide on the Al metal due to the FPL treatment. The development of the scallop like structures matches the time of FPL treatment to give samples that survive the ultrasonic rinsing test, and this topography may play a helping role in the adsorption process. A common view is that the surface morphology may influence mechanical interlocking within the adsorbed layer [2, 23-26, 109].

Figure 3.5 shows typical examples of Al 2p spectra from high-purity samples that have been FPL treated for 0, 15, and 60 min. The interpretation of these Al 2p spectra is straightforward, where the peaks at binding energies of 72.65 eV and 75.5 eV refer to the metallic and oxide components respectively. Changes are seen for the relative proportions of oxide and metallic components with increase in the FPL treatment time. For the native oxide sample (0 min), approximately 86% of Al 2p signal corresponds to the oxide form (14% as metallic form). As the FPL treatment was applied, the proportions changed with the metallic proportions becoming larger. For 1 min pre-treatment the relative amounts were 73% oxide, 27% metal; at 5 min 66% oxide, 34% metallic; 15 min 59% oxide and
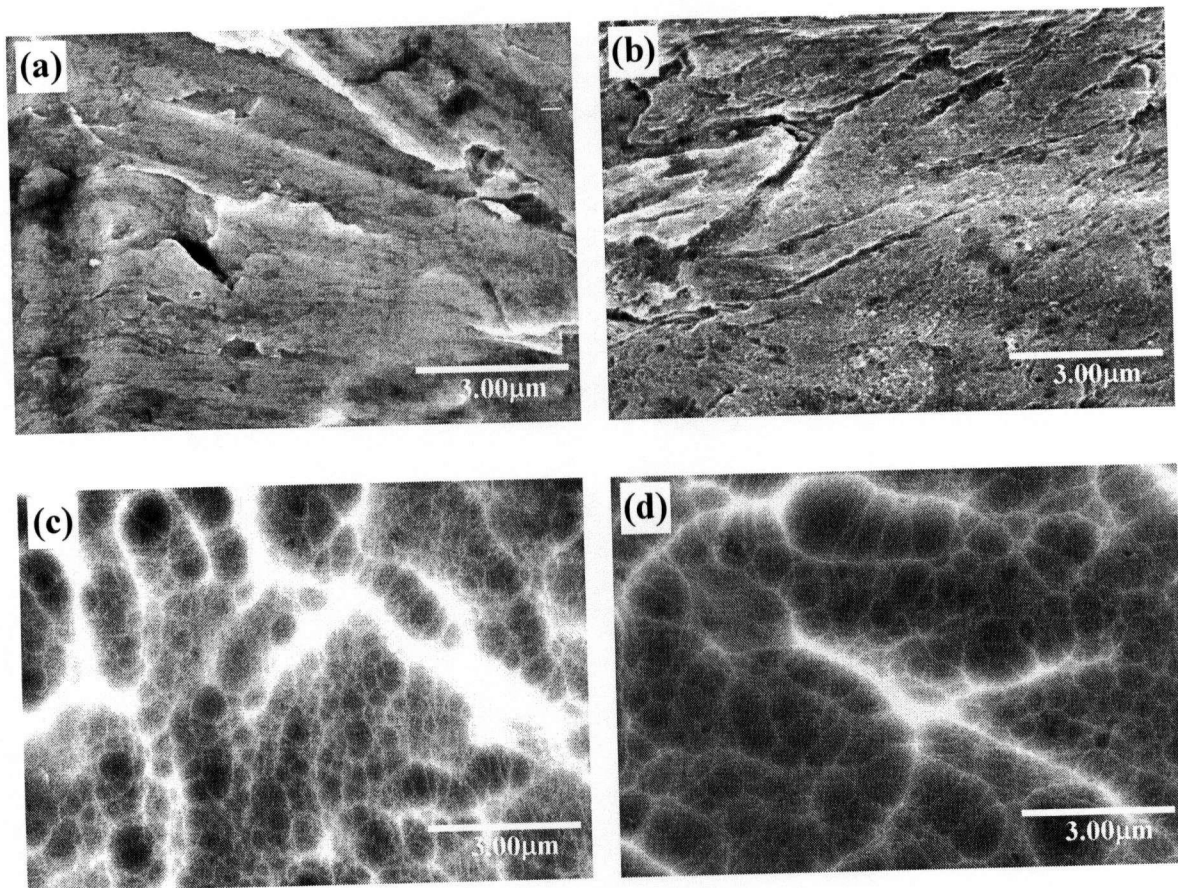
Figure 3.4. SEM micrographs of uncoated high-purity Al surfaces that were FPL treated for: (a) 0 min, (b) 1 min, (c) 10 min, and (d) 25 min.
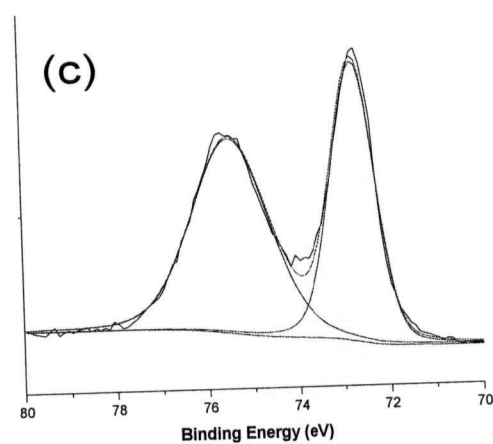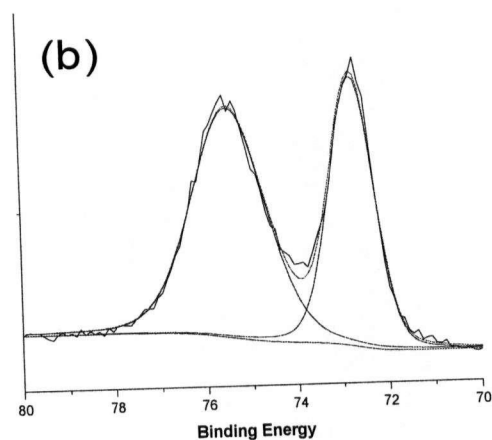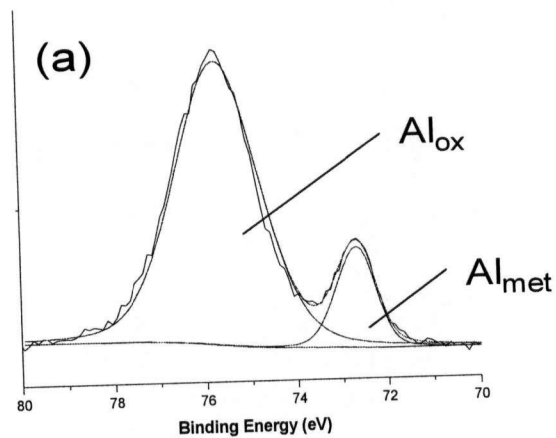
Figure 3.5. Al 2p spectra curve fitted for the oxide (Al_{ox}) and metallic (Al_{met}) components for the oxidized Al surfaces: (a) native oxide (i.e. no FPL treatment), (b) after 15 min FPL treatment, (c) after 60 min FPL treatment.

41% and by 25 min the proportions reached 56% oxide and 44% metal. For times longer than 25 min the proportions did not change. These results show etching of the oxide is dominant for the shorter treatment times, and the etching and oxidation processes reach equilibrium after around 25 min of the treatment. The strong etching that occurred for the initial FPL treatment can be seen to remove contamination as well as the less firmly anchored parts of the substrate. Thus the combination of observations where flaky surfaces were observed for shorter times of FPL treatment (SEM), and significant etching was also occurring for the same time range (XPS Al 2p), suggests that the samples that were FPL treated for short times failed the ultrasonic rinsing test because of loosely-held BTSE or poor oxide adhesion (or both).

3.3.2 BTSE Adsorption on FPL Treated 7075-Al Alloy

3.3.2.1 FPL Treatments

First assessments of the different pre-treatments applied to the anodized 7075-Al sample were made by comparing the effects of different FPL treatment times prior to the application of the BTSE coating. Table 3.1 summarizes some observations by XPS. The relative sizes of the metallic Al 2p component and the oxide Al 2p component measured for different times of the FPL treatment shows that the oxide component dominates throughout; the metallic component only becomes detectable after about 5 min of FPL treatment, but it is still a minority component after one hour. The inability of XPS to detect the metallic component from the initially anodized sample is expected given its nature, but etching occurs during the FPL process. This leads to some uncovering of the metallic Al 2p component in XPS, as well as to changes that are directly visible in the

SEM images (Figure 3.6). A micrograph for the untreated anodized 7075-Al surface is shown in Figure 3.6(a), and structure in the images develop for increasing times of the FPL treatment: after 1 min an elongated structure (Figure 3.6(b)) forms, and this followed at 3 min by the presence of round dots (Figure 3.6(c)) which subsequently develop into the larger circular (or scallop-like) structures that are seen after 5 min of the FPL treatment (Figure 3.6(d)). This structure takes longer (10 min) to develop on the high-purity Al samples [111]. However, for both types of oxidized Al sample these scallop structures increase in size for longer FPL treatments, and Figures 3.6(e) and (f) show images after the FPL treatment has been applied for 10 and 60 min respectively to the 7075-Al samples.

Table 3.1. Observations from XPS for different pre-treatments of the Al_{met}/Al_{ox}[a] (before BTSE coating) and Al/Si ratios (after BTSE coating).

Pre-treatment	Al_{met}/Al_{ox}	Al/Si
0 min FPL	0.00	10.4
1 min FPL	0.00	6.0
3 min FPL	0.00	1.8
5 min FPL	0.04	0.0
10 min FPL	0.05	0.0
15 min FPL	0.05	0.0
30 min FPL	0.07	0.0
60 min FPL	0.15	0.0
5 min FPL + 1 h H_2 plasma	0.02	1.1

[a] **This is the ratio of the metallic peak to total oxide peak in Al 2p spectra.**
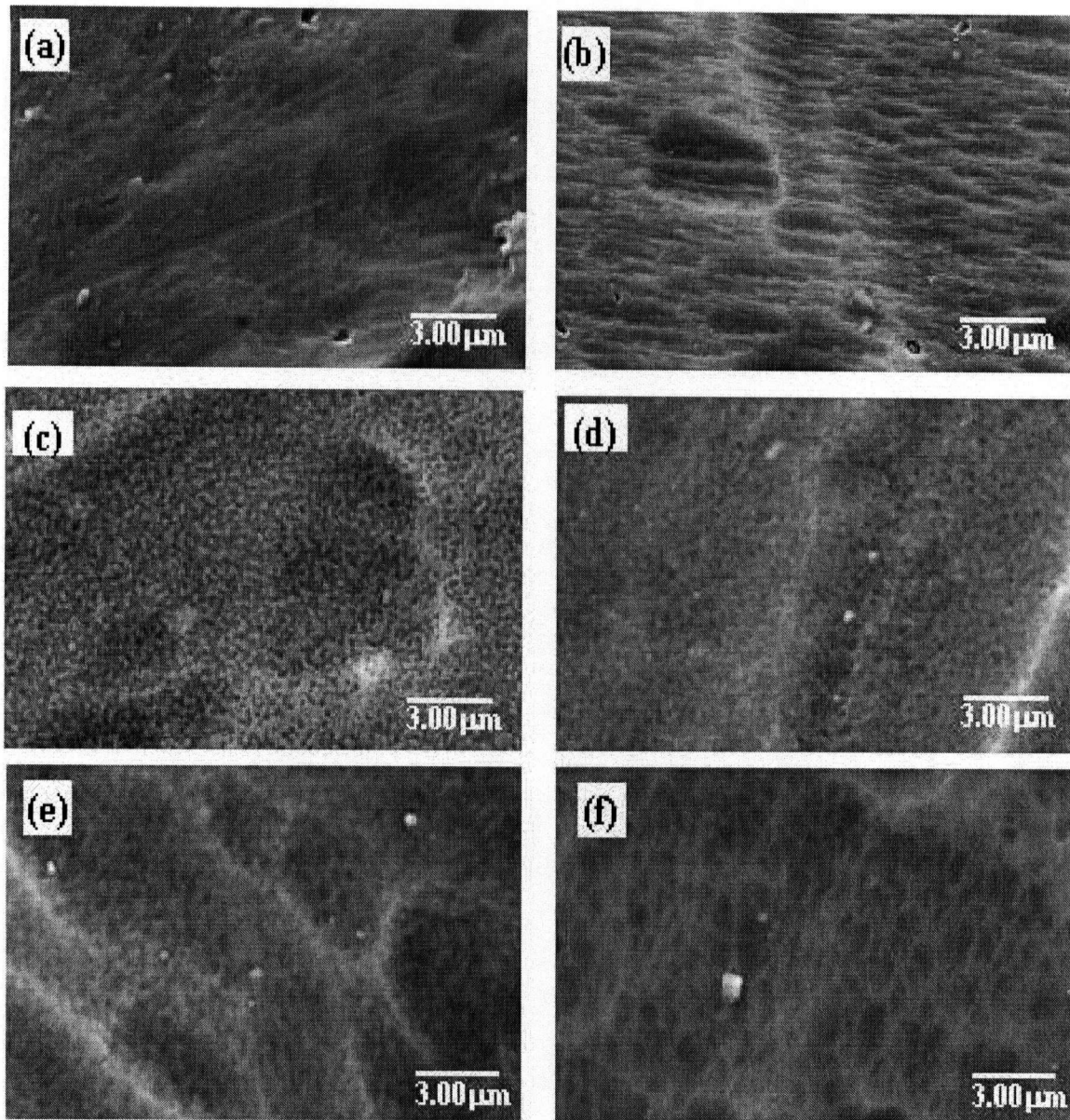
Figure 3.6. SEM micrographs from uncoated anodized 7075-Al alloy surface after different periods of FPL pre-treatment: (a) 0 min, (b) 1 min, (c) 3 min, (d) 5 min, (e) 10 min, and (f) 60 min.

Table 3.1 also reports information for the amount of organosilane adsorption when the 7075-Al samples, given varying FPL pre-treatment times, are coated with the BTSE solution. It is clear that the total BTSE adsorption increases with the time of FPL treatment, although XPS cannot detect the signal from the Al substrate for FPL times of 5 min or greater. Also, after the ultrasonic rinsing, XPS shows that the BTSE coatings on these surfaces have good retention according to the previously-used criterion [111]. This contrasts with the situation for high-purity Al samples where around 10 min of the FPL treatment is required before the BTSE attachment is sufficiently strong to survive this test.

To gain insight into the strength of the adsorption bonding for the anodized 7075-Al samples, SIMS characterizations were made by measuring the $[AlOSi]^+/[Al_2O]^+$ ratio (or I_{71}/I_{70} ratio). However, the relatively low value of 0.6 was found for all samples that had been FPL treated through the time range 0-60 min. This suggests that the amount of direct Al–O–Si bonding is not high in relation to the underlying alumina substrate, and accordingly we conclude that the ability to survive the rinse test, after applying the BTSE, is not primarily due to strong interfacial bonding interactions.

The developing model for high-purity Al is that, for the longer FPL times, the surface undergoes competing etching and reoxidation processes, and becomes more undulating/porous at the microstructural level. The latter structure is superimposed on the scallop structure noted in the SEM micrographs. For the anodized 7075-Al sample, the initial surface is believed to be porous, probably down to the nm scale, and this structure apparently allows more BTSE to adsorb and with sufficient protective adhesion to pass the ultrasonic rinse test.

3.3.2.2 Other Treatments

When heat pre-treatment was applied to the high-purity Al system, it was shown that this pre-treatment helped modify the native and the FPL treated high-purity samples to aid in subsequent adhesive bonding to BTSE. Furthermore, the H_2 plasma pre-treatment was able to chemically modify the surfaces to result in more Al-O-Si bonding after dipping in silane according to the observations by SIMS [112].

In the context of 7075-Al, heating either the anodized sample or samples after FPL treatment had no effect on the subsequent adsorption according to the observations by SIMS and XPS, including after an ultrasonic rinse. Nevertheless, application of the H_2 plasma treatment did cause changes to the subsequent BTSE adsorption, and this is discussed for an anodized 7075-Al sample that had been subjected to the FPL treatment for 5 min. This time was chosen as the shortest FPL application that reduced the oxide layer sufficiently to allow detection of the metallic Al 2p component in XPS, with no evidence of sample charging in either characterization technique.

Figure 3.7 compares Al 2p and O 1s spectra, before and after the H_2 plasma treatment, from the anodized 7075-Al sample which had been subjected to the FPL treatment for 5 min. This treatment shifts both the O 1s and Al 2p oxide peaks to higher binding energy by about 0.8 eV (to give the respective values 533.5 and 76.1 eV); the H_2 plasma treatment also gives some broadening in the peak structure. This change is accompanied by an increase in the oxide-to-metallic Al 2p ratio (Table 3.1), which suggests some overall enhancement of the oxide layer. In principle the broadening could result from charging, although no direct evidence for this was seen by applying the bias potential technique [113, 114]. Most likely the shift and broadening seen in the spectral
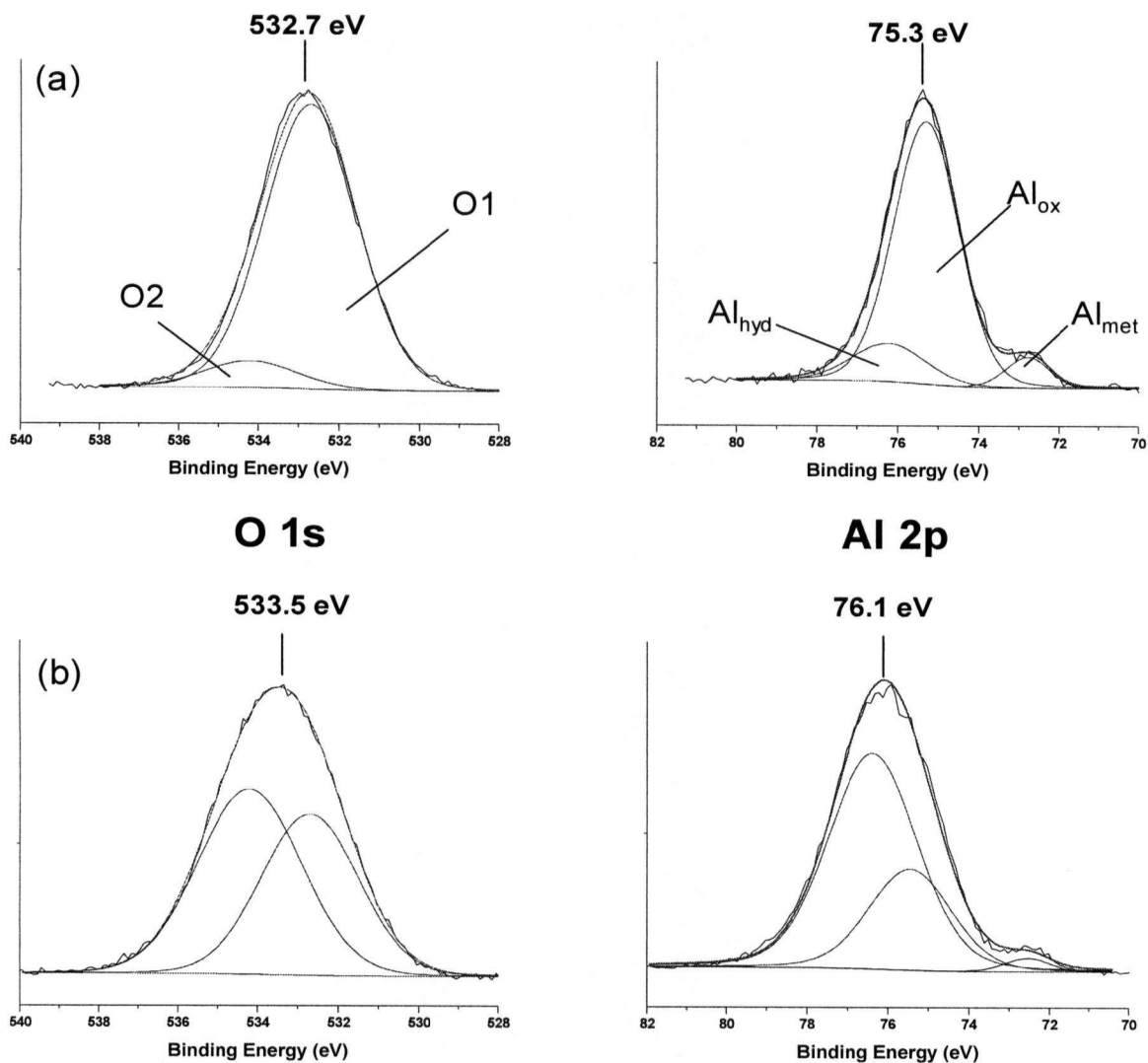
Figure 3.7. XPS curve fitting for uncoated 7075-Al alloy samples after: (a) 5 min FPL treatment and (b) 5 min FPL followed by 1 h H_2 plasma treatment. The O 1s spectra are fitted to the two components O1 (O^{2-}) and O2 (OH, H_2O, C(O)), and the Al 2p spectra are fitted to the three components Al_{met}, Al_{ox}, Al_{hyd}.

75

peaks arose from the increase in population of Al-OH sites, as has been concluded from qualitative observations when the H_2 plasma treatment is applied to other oxidized metal surfaces [115-117].

The general systematic trend for fitting the O 1s spectra has been to fit it with two components where the lower binding energy component (O1) is believed to be due to the contribution from O^{2-} and the higher binding energy component (O2) includes contributions from OH, H_2O and C(O); the two components have been found to be 1.1-1.5 eV apart in the literature [73, 112, 118-123]. The actual optimized binding energies for these peaks found in this work were 532.7 and 534.2 eV respectively, and these values agree with conclusions from a recent investigation of anodized Al surfaces by Alexander et al. [124].

Since the spectral changes in Al 2p after the H_2 plasma treatment were much greater than the high-purity case [112], a curve fitting was attempted using the metallic component (Al_{met}) and two components which contribute to the overall oxide peak, namely an oxide component (Al_{ox}) and a hydroxide component (Al_{hyd}) [125]. The present curve fitting proceeded with the Al_{ox} and Al_{hyd} component peaks separated by 0.93 eV, with the $2p_{1/2}$ and $2p_{3/2}$ contributions fixed at 0.46 eV apart while maintaining their areas in the expected 1:2 ratio [125]. This approach follows several studies on different metals which concluded that the hydroxide component is at higher binding energy than the oxide component [126-130]. For Al, the situation has been less clear [131-136], although this trend has received support over the years [126, 133, 134].

Table 3.2. Observations by XPS for an anodized 7075-Al sample after two different pre-treatments.

	FPL[a] only			FPL[a] and H_2 plasma treatment		
	Position (eV)	FWHM (eV)	Relative Area	Position (eV)	FWHM (eV)	Relative Area
O 1s						
O1	532.7	2.6	0.99	532.7	2.7	0.45
O2	534.2	2.7	0.01	534.2	2.8	0.55
Al 2p						
Al_{met}	72.65	1.1	0.06	72.65	1.2	0.02
Al_{ox}	75.15	2.0	0.81	75.27	2.2	0.30
Al_{hyd}	76.08	2.2	0.13	76.20	2.4	0.68

[a]**All FPL treatments are for 5 min.**

The results presented in Table 3.2 are consistent with the H_2 plasma treatment resulting in a marked increase in Al-OH contributions, as seen in both O 1s (O2 component increases its relative value from 0.01 to 0.55) and Al 2p (Al_{hyd} increases from 0.13 to 0.68). The examination with SIMS of the BTSE coatings further showed an increase in the $[AlOSi]^+/[Al_2O]^+$ ratio from 0.6 to 1.0 when the H_2 plasma pre-treatment was applied. This is fully consistent with the enhancement of the Al–OH groups by the pre-treatment holding into the coating solution, and hence to an increase in the coupling reaction with formation of Al–O–Si bonds via the Al–OH + Si–OH → Al–O–Si + H_2O reaction. SEM did not detect any significant changes after the sample was exposed to the H_2 plasma treatment, and hence it appears unlikely that the increase in the SIMS ratio could be associated with any modification in surface morphology resulting from the H_2 plasma treatment.

The BTSE-coated sample that was H_2 plasma pre-treated showed less total bonded silane than the sample that just received the FPL pre-treatment. For example, in the absence of the H_2 plasma pre-treatment, XPS showed that a sufficiently thick silane coating was formed to obscure detection of the Al 2p spectrum. By contrast, when the H_2 plasma pre-treatment was included, the Al 2p structure could be detected with an Al/Si ratio of 1.1. This value did not change after the sonication test, so indicating well-adhered BTSE chemisorption consistently with the observations from SIMS. It appears that this thinner coating is a consequence of the greater number of Al–OH groups on the surface. The hydrolyzed BTSE has six Si–OH groups per molecule, and at the interface more are needed to undergo the coupling reaction with the increased number of Al–OH groups after the plasma treatment. This leaves less Si–OH groups available for self BTSE polymerization at the first layer, and apparently leads to a reduction in the total amount of silane adsorption compared with when there are smaller numbers of Al–OH groups on the original surface.

3.4 Concluding Remarks

The FPL pre-treatment process carried out prior to BTSE coating on high-purity Al and 7075-Al surfaces were assessed by characterizing the natures of the coatings formed by using a combination of SIMS, XPS, SEM, and ultrasonic rinsing test. The different techniques gave complementary information, but two key aspects are emphasized for effective adhesive bonding: first the number of surface OH groups, and second the overall surface morphology prior to coating. It appears that the pre-treatment needs to optimize the surface OH for action in the coating solution and the form of

surface morphology prior to coating is important insofar as a well-anchored oxide layer is required for effective adhesive bonding by the BTSE. Such an anchoring can be accomplished by the FPL process. We use that industrial process in this work more for providing different surfaces prior to adding a BTSE coating, rather than for studying the FPL process itself. Ultimately that process needs to be replaced by other approaches that avoid the use of Cr^{6+}, but industrial practice with the standard FPL etch shows a range of treatment times (15-30 min) for different types of Al sample [42].

This program of study has shown that a 15 min FPL treatment applied to native oxide on a high-purity Al sample is effective for giving a compact oxide layer and the surface with the highest number of OH groups prior to coating. This treatment time corresponds with the optimal Al-O-Si bonding time range. On the anodized 7075-Al sample only a 5 min FPL treatment is required to optimize the BTSE adsorption and interfacial bonding is enhanced by a hydrogen plasma treatment applied just prior to the coating. The example of using the H_2 plasma for treating the anodized 7075-Al sample, shows that an increase in the Al–O–Si bonding can occur with a decrease in the BTSE polymerization, and that emphasizes the subtle competitions that occur between the two processes. In extension, the existence of a thicker coated layer does not necessarily imply more-effective adhesive bonding, but this work does aim to increase our insight into how the different pre-treatments can lead to different outcomes for BTSE adsorption, depending on the actual natures of the initial oxidized Al surfaces being considered.

This study did not identify differences which can be associated with the specific microstructures applying in the 7075-Al sample compared with the high-purity case, and

this will be considered in the next chapter to assess how the BTSE adsorption may vary over a heterogeneous alloy surface, with second-phase particles.

Chapter 4 Adsorption of BTSE and γ-GPS Organosilanes on Different Microstructural Regions of 7075-T6 Aluminum Alloy[†]

4.1 Introduction

In this chapter, further investigation into the coating of 7075-Al alloy is considered where the alloy surface shows chemical heterogeneity due to the presence of second-phase particles. The corrosion resistant oxide film that forms naturally on high-purity aluminum also occurs on surfaces of aluminum alloys, although for the latter the oxide films may be less evenly distributed, especially because of the presence of the intermetallic constituents (second-phase particles) [2]. In general, the addition of the guest elements makes the alloys more susceptible to corrosion than is the case for pure aluminum. Thus it is of importance to investigate how these intermetallic constituents react, in comparison to the main alloy matrix, when the coated surface is in a corrosive environment, but to date knowledge in this area appears quite sparse [74].

To help build more understanding for silane coatings on microstructural regions of aluminum alloy, this work deals with two type of silanes, namely BTSE and γ-glycidoxypropyltrimethoxysilane (γ-GPS), which have contrasting behaviors in their interactions with the metal as mentioned in Chapter 1. This work aims to assess the conditions where both silanes can be adsorbed on all micro-regions of a mirror-polished 7075-T6 Al alloy surface. In particular, the focus is on: (i) how the chemical heterogeneity at the alloy surface is affected by air oxidation and heating in atmosphere;

(ii) how these pre-treatments affect the silane coating; (iii) how the coating solution pH affects the adsorption; and (iv) an exploration of the nature of the bonding present at the silane-aluminum alloy interfaces.

In order to achieve the goals outlined above, a series of experiments were set up to probe the 7075-T6 Al alloy surface before and after various pre-treatments and coating treatments. X-ray photoelectron spectroscopy (XPS) provided information about the total amount of silane present on the surface after coating, but it was also used in conjunction with an ultrasonic rinsing test to give a preliminary guide to the strength of the silane adsorption [112]. SEM helped monitor changes in surface morphology prior to and after coating, as well as to identify the second-phase particles on the surface. Scanning Auger microscopy (SAM) was used to probe the varying chemistries that occur over different micro-regions of the surface, and time-of-flight secondary-ion mass spectrometry (TOF-SIMS) helped to identify the presence of metal–O–Si bonding formed on the differently-treated alloy surfaces.

4.2 Experimental

The 7075-T6 aluminum alloy samples were cut into 1 cm^2 square panels (approximate minority components: 6 wt% Zn, 3 wt% Mg, 2 wt% Cu, 0.5 wt% Fe, 0.4 wt% Si, 0.3 wt% Mn and 0.2 wt% Ti, supplied by Department of National Defence, Canada) and mechanically polished by diamond paste to a mirror polish (~1 μm surface roughness). They were then cleaned in acetone (10 min) and methanol 5 min (both solvents HPLC grade). These polished samples were subsequently given one of two treatments prior to coating with a silane: one treatment involved exposure to air for 20 h

(to give a "native oxide"), while the other involved heating at 200°C (measured with alumel-chromel thermocouple) for 15 min in atmosphere. The latter sample was quickly transferred after the heating stopped to a vacuum chamber (10^{-3} Torr) for 20 h prior to being used for the experiments described.

Silane solutions (1% BTSE and 1% γ-GPS) were prepared by mixing 1 vol% silane (Aldrich), 93 vol% methanol (HPLC grade, Fisher Scientific), and 6 vol% distilled water. The solution was then stirred for 5 h at room temperature to ensure complete hydrolysis of the silane. Following either the air oxidation or the heat treatment, each sample was immersed into hydrolyzed silane coating bath for 1 min and then dried in nitrogen. The natural pH values for 1% BTSE and 1% γ-GPS are 4.3 and 5.7 respectively. Some experiments used γ-GPS solutions with lower pH values prepared by drop-wise addition of concentrated glacial acetic acid. The silane solutions were measured with a pH meter (Orion Benchtop, model 420A) before and after each coating process.

Prior to the TOF-SIMS measurements (Section 4.3.5), the samples were rinsed in distilled water for 5 min immediately after coating to avoid formation of a thick polymeric layer. TOF-SIMS measurements were performed with an ION-TOF IV instrument (at the University of Toronto) using the $^{69}Ga^+$ gun operated at 25 keV with a current of 2.7 pA in bunched (high mass resolution) mode [107]. Sputtering was accomplished over an area 300 μm x 300 μm using the SF_6 source operated at 3 keV and 11 nA. Positive spectra were obtained with the incident beam (total integrated primary ion dose $<10^{12}$ ions cm^{-2}) rastered over an area 50 μm x 50 μm. Mass resolution (m/Δm) for the $^{28}Si^+$ ion was around 8000. Spectra were calibrated with the known masses

associated with peaks for the species H^+, CH_3^+, Mg^+, Fe^+ and Cu^+. Positions of the particles were confirmed by obtaining images in the high spatial resolution mode [107].

SAM analyses were performed using a Microlab 350 spectrometer (Thermo Electron Corp.) with field emission source and hemispherical energy analyzer. Auger point analysis was done with the primary electron beam set at 10 keV and 4 nA (sample current), and the energy analyzer was operated in the constant-retarding ratio mode with the CRR value set at 4.0. SEM micrographs were measured at various magnifications using the same instrument. XPS spectra were obtained with a Leybold MAX200 spectrometer using the Mg $K\alpha$ source (1253.6 eV) operated at 10 kV and 20 mA. The system pressure was at 1×10^{-9} Torr while measurements were obtained. Survey spectra were obtained with the pass energy set at 192 eV and binding energies were referenced to the C 1s peak for adventitious hydrocarbon contamination set at 285.0 eV.

In order to examine how well the silane films adhered to the pre-treated Al alloy surfaces, a combination of XPS and a water ultrasonic rinsing test was conducted. After samples were coated, they underwent an initial XPS analysis, and were then sonicated in distilled water for 30 min using a sonication bath from Solid State/Ultrasonic (model T14B, L&R Manufacturing). Finally the samples were dried in nitrogen prior to testing further with XPS in order to assess the degree of de-adhesion.

4.3 Results and Discussion

4.3.1 Initial Observations for 7075-Al Alloy Surface

Figure 4.1 shows a SEM image from a mirror-polished 7075-Al alloy surface which had been Ar^+ sputtered until no carbon or oxygen signals were detected in the
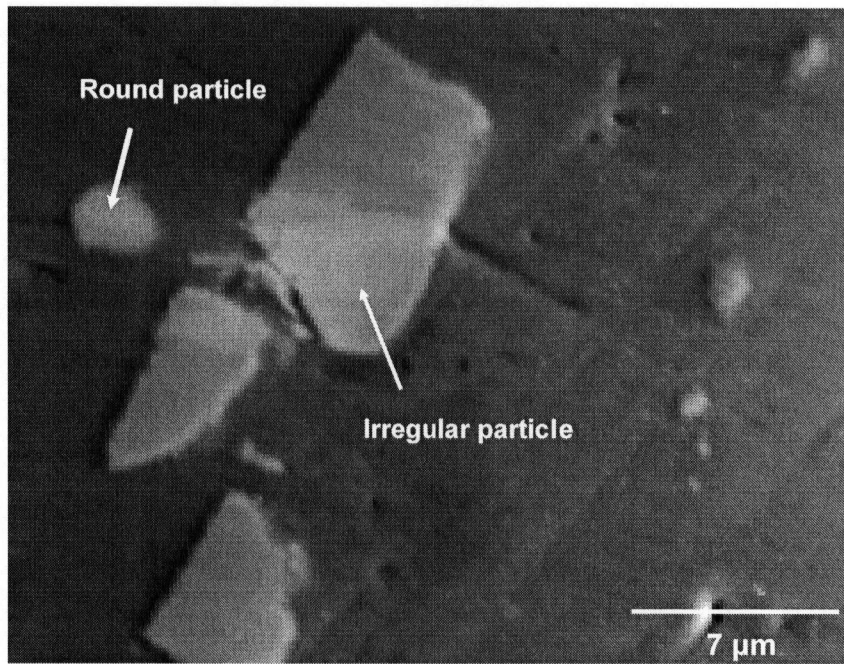
Figure 4.1. SEM micrograph from a mirror-polished surface of 7075-Al alloy after a light sputtering.

Auger spectra. This surface showed two types of second-phase particles: one type has curved sides (such a particle is referred to below as being round-shaped), while the other type of particle has straight sides (and such a particle is referred to later as being irregular-shaped). The cleaned sample allowed an identification of the chemical components at the different micro-regions of the surface without interference from surface contaminants. Auger measurements from the round-shaped particle showed the presence of the elements Al, Cu and Mg (referred to as having a Al-Cu-Mg composition), while those from the irregular-shaped particle had the Al-Fe-Zn composition. Others have found a similar match of particle shape and chemical composition, although the exact compositions of the particles can vary with the specific sample [7, 8, 74, 139].

The elemental Auger spectra obtained from the three micro-regions (round particle, irregular particle and matrix) for the cleaned alloy sample were compared with spectra measured from high-purity metals (which agreed closely with the spectra shown in the VG Auger Handbook [140]) in order to assess affects from alloying. Only the Al signal was detected by SAM from the matrix region of the cleaned 7075-Al sample, and this spectrum did not differ from that of pure metallic Al (Figure 4.2). By contrast, in the regions where more than one element was detected by Auger electron spectroscopy, differences are seen in the spectra compared with those from the individual pure metals. Measurements from the round particle showed an Al spectrum that differed from that of pure Al metal by not having a strong peak at 1378 eV kinetic energy (Figure 4.3). In addition for the round-particle region, differences were evident in the spectra for Mg (Figure 4.4) and Cu (Figure 4.5). For Mg, the Auger peak observed at 1176 eV kinetic energy for the pure metal form is not seen in the spectrum from the round particle. A
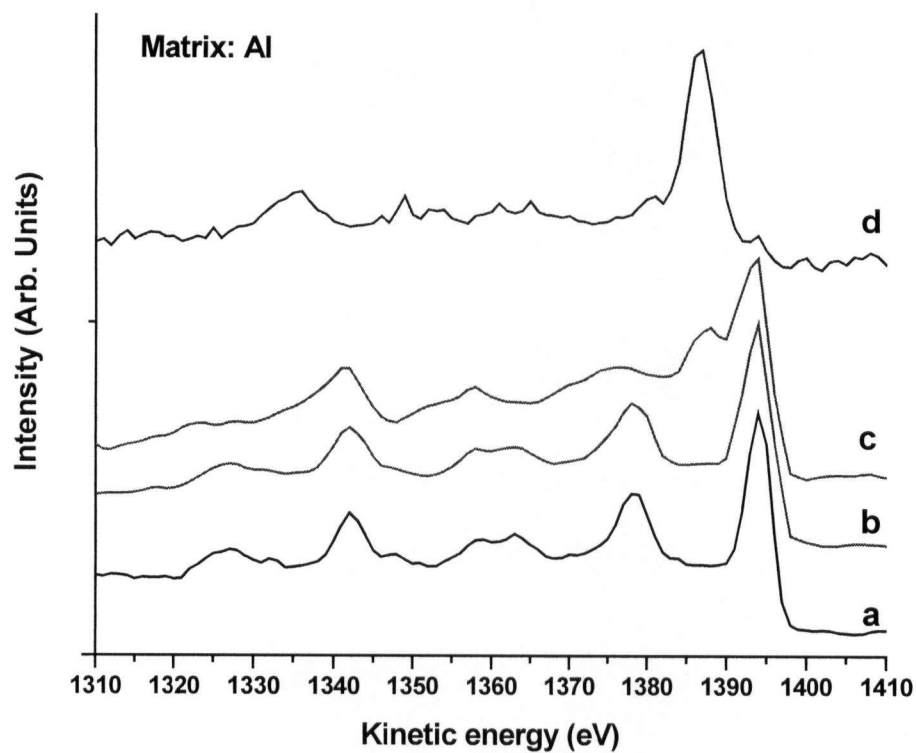
Figure 4.2. Comparison of Al KLL spectra for (a) pure Al; the matrix region of 7075-Al alloy: (b) sputter cleaned, (c) air oxidized, and (d) heated in air.
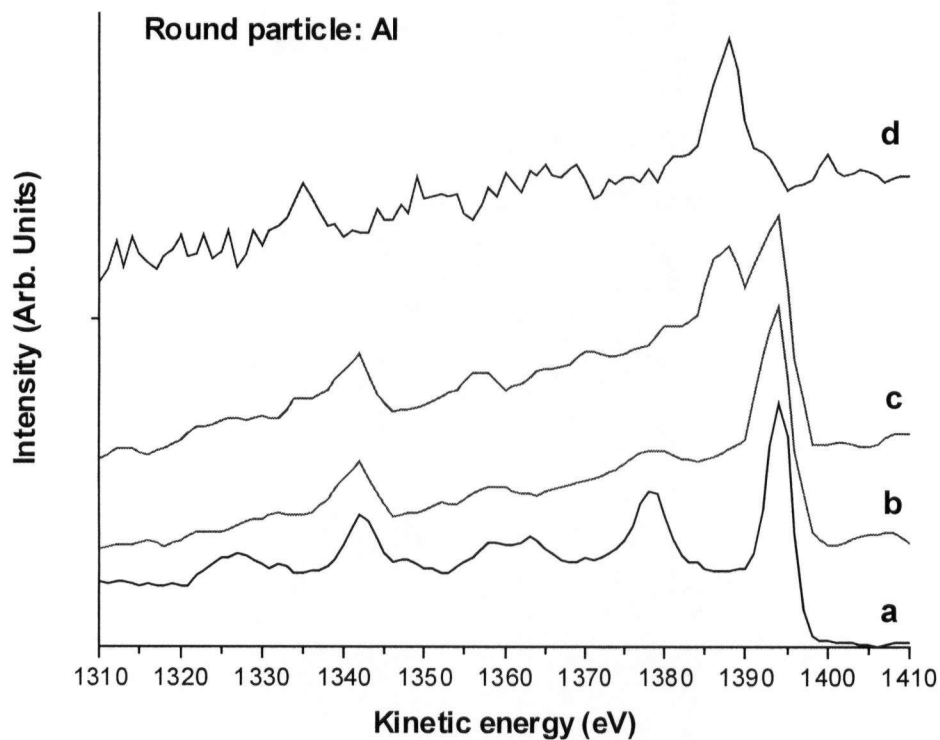
Figure 4.3. Comparison of Al KLL spectra for (a) pure Al; the round-particle region of 7075-Al alloy: (b) sputter cleaned, (c) air oxidized, and (d) heated in air.
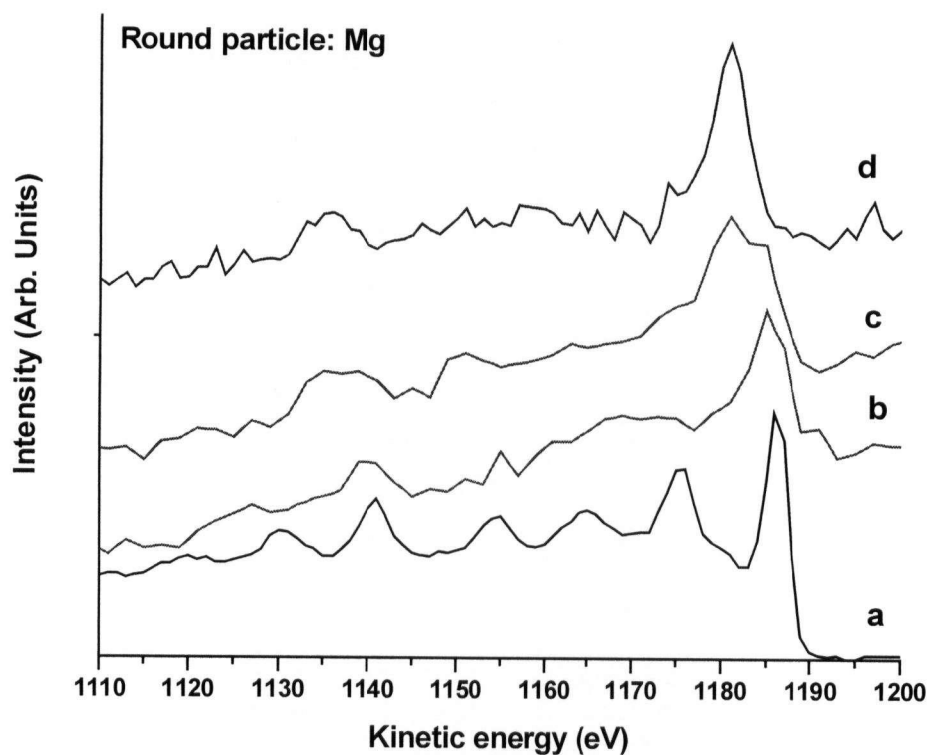
Figure 4.4. Comparison of Mg KLL spectra for (a) pure Mg; the round-particle region of 7075-Al alloy: (b) sputter cleaned, (c) air oxidized, and (d) heated in air.
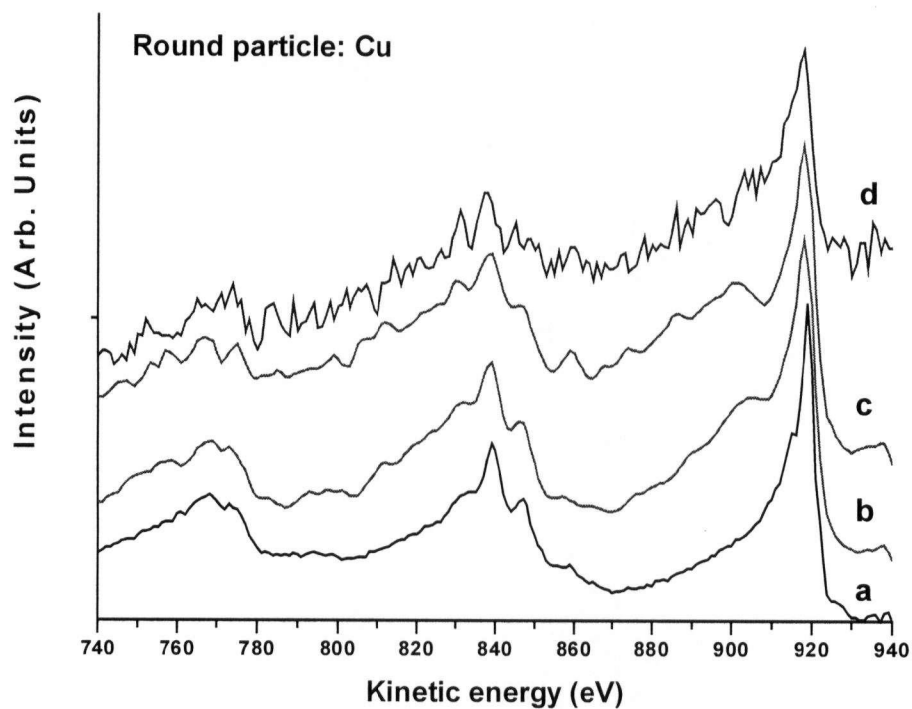
Figure 4.5. Comparison of Cu LMM spectra for (a) pure Cu; the round-particle region of 7075-Al alloy: (b) sputter cleaned, (c) air oxidized, and (d) heated in air.

similar situation applies to the Auger structure for Cu at 904 eV kinetic energy. The differences observed are fully consistent with the round particle being made up of the three elements in the form of an intermetallic compound. Corresponding observations apply to the irregular particle where spectra for Fe and Al are shown in Figures 4.6 and 4.7 respectively. Distinct differences are seen at kinetic energies 634 eV and 688 eV for the Fe spectra and 1378 eV for the Al spectra. The Zn signal obtained from the irregular particle was not strong enough to assess whether that element's character had changed significantly from that of the pure element, but the spectra for Fe and Al did indicate differences consistent with intermetallic compound formation.

To study how the various regions of the sample surface are affected by air oxidation, the mirror-polished alloy was exposed to air for 20 h prior to being introduced into the vacuum chamber. The SEM micrograph taken from that surface did not differ from the image shown in Figure 4.1 for the surface that had been sputtered clean, but differences are apparent in the Auger electron spectra. After the air exposure for 20 h, the Al spectrum from the matrix region showed a new peak at 1387 eV kinetic energy (Figure 4.2), which is mainly due to the formation of Al oxide. The peak at 1394 eV remains prominent so suggesting that the air exposure has not fully oxidized the matrix region. The Al spectrum from the round-shaped particle also shows a new peak at 1387 eV (Figure 4.3), and the metallic component still has a greater intensity than the oxide component. However, the extra peak observed at 1181 eV kinetic energy in the Mg Auger spectrum from the round particle is more intense than the metallic peak at 1186 eV (Figure 4.4). The Cu spectra measured before and after the air exposure show a small change as a new peak is seen at 860 eV after air oxidation (Figure 4.5). However,
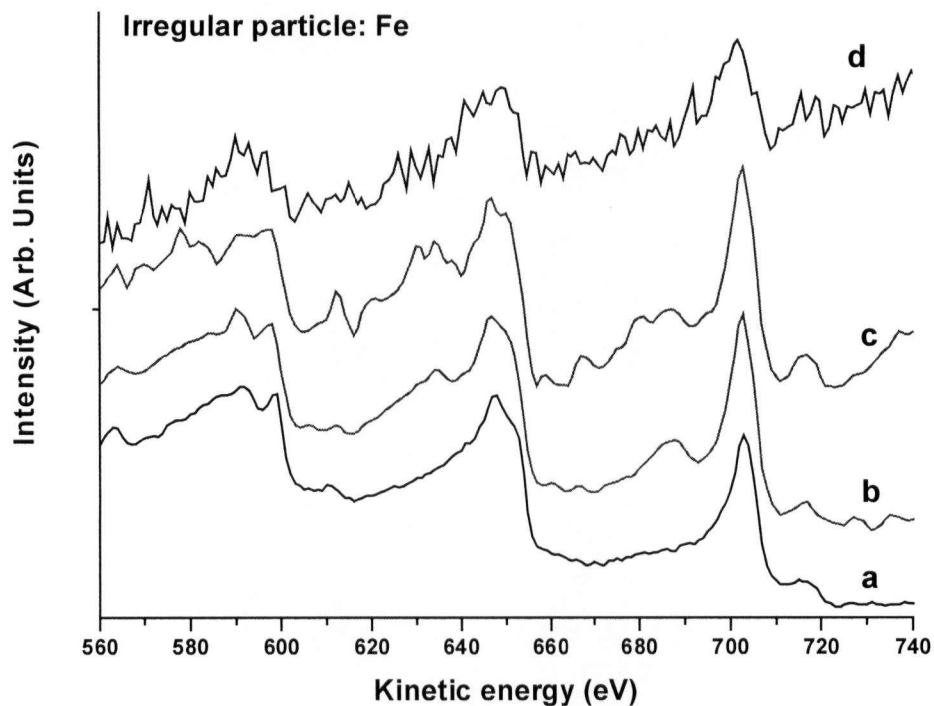
Figure 4.6. Comparison of Fe LMM spectra for (a) pure Fe; the irregular-particle region of 7075-Al alloy: (b) sputter cleaned, (c) air oxidized, and (d) heated in air.
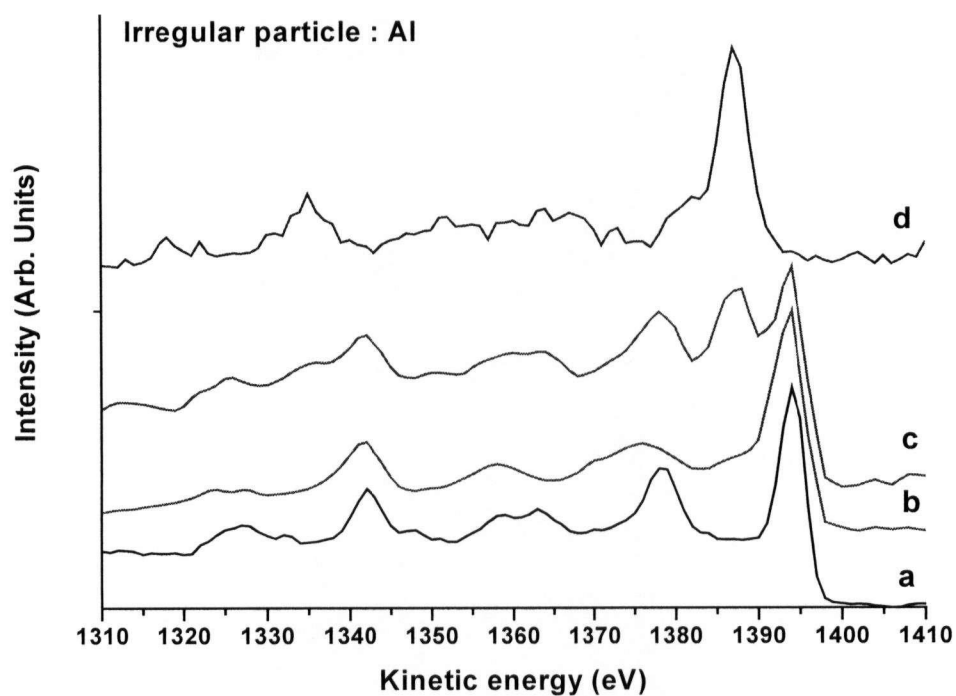
Figure 4.7. Comparison of Al KLL spectra for (a) pure Al; the irregular-particle region of 7075-Al alloy: (b) sputter cleaned, (c) air oxidized, and (d) heated in air.

90

it is difficult to tell the extent of the Cu oxidation. In order to investigate this further, the atomic percentages for the three elements from the sputtered cleaned surface were compared to the surface that was air oxidized (Table 4.1).

Table 4.1. Atomic percentages from SAM for elements in the round and irregular particles on the sputter-cleaned and air-oxidized surfaces.

	Round particle			Irregular particle		
	Mg	Al	Cu	Al	Fe	Zn
Cleaned	24.7	42.5	32.8	46.0	41.2	12.9
Oxidized	39.1	41.4	19.5	65.3	34.7	0.0

The results in Table 4.1 show that after air oxidation, the detected amount of Mg in the round particle is enhanced, whereas the Cu amount is decreased. The proportion of Al does not change significantly, but the amount relative to Cu has increased. Thus SAM indicates that the air oxidation enhances the amount of Mg in the surface region, while the amount of Cu is appreciably decreased. This apparently implies some tendency for the elements within the surface region to rearrange, as a result of oxidation, so that Mg becomes more on top, Al is intermediate, and the Cu is predominantly further below the surface. This observation matches the conventional measures of ease of oxidation (e.g. $\Delta G_f/n$ for formation of oxide [141] or oxidation potential) in that Mg should be most easily oxidized, followed by Al and then Cu.

The irregular particle shows contrasting behavior. Although Zn was detected by Auger electron spectroscopy from the sputtered clean sample, that was not the case after the air oxidation. Figure 4.6 compares spectra for Fe before and after the air oxidation, which leads to new peaks at 612 eV, 667 eV and 680 eV kinetic energy. For Al (Figure

4.7) the trend that was seen for Al in other micro-regions is observed for the irregular particle, in particular with growth of the new peak at 1387 eV kinetic energy, as well as a peak at 1378 eV. The spectrum for oxide growth on pure Al (Figure 4.2) does not show the peak at 1378 eV, and thus the growth of this peak indicates a distinctive aspect for oxidation of the Al-Fe-Zn irregular particle. Table 4.1 shows the atomic percentages from SAM for Al and Fe from the sputter-cleaned surface, as well as the air-oxidized surface, and indicates the Al enhancement after the oxidation in air. It is concluded that oxidation of the Al-Fe-Zn intermetallic particle encourages Al and Fe segregation, thereby ensuring that Zn in the surface region becomes completely covered. Therefore, it is clear that Auger electron spectra indicate that air oxidation affects the surface elemental distribution for both types of second-phase particle.

4.3.2 Coating of Air-oxidized 7075-Al with 1% BTSE

BTSE is a non-organofunctional silane which can coat without the alternative 'upside down' orientation that may occur with the organofunctional silanes [56, 142]. The silane coating process is known to be dependent on many factors including hydrolysis of the silane molecule, etching of the metal oxide layer, protonation of the oxide, coupling reaction at the metal-silane interface, and polymerization of the silane after air drying. In order to coat aluminum surfaces with strongly bonded silanes, the uppermost oxide layer needs to be protonated in order to form Al–OH groups, and the silane alkoxyl groups need to hydrolyze to give Si–OH groups which can couple with the Al–OH groups to form Al–O–Si bonding [112]. Compared to other organofunctional silanes that have a maximum of three Si–OH groups after hydrolysis, BTSE can form

more Si–OH groups, a process that is favored in the pH range of 4 to 6 [35-37]. The pH of the natural BTSE solution (no adjustment) used in this study is 4.3, a value that falls within the reported range for coating. Another factor with a role in the silane adsorption is surface morphology insofar as a rougher surface (e.g. from acid etching) may enhance the silane adsorption [61, 73, 109].

SEM micrographs of the BTSE coated surface are shown in Figures 4.8(a) and (b) for the round and irregular particles respectively. SAM measurements of the Si signal confirm that the silane adsorbs on all areas of the sample, although more Si is detected at the edges of both types of particle than on the particles themselves. This appears as an effect of galvanic coupling, where the difference in potential between a particle and the neighboring matrix accelerates etching at the particle's edge, so creating a local morphology for enhanced adsorption. After coating the Al signal was still observed by XPS, where the Si/Al ratio was found to be 0.72; this value reduced to 0.68 after the ultrasonic rinsing. That change is barely significant, but the near constancy does confirm a reasonable level of adhesion. By contrast, in other work on high-purity Al, some surfaces showed much larger loss of silane as a result of this test [112].

While most irregular-shaped particles appear relatively unchanged after the coating (Figure 4.8(b)), substantial changes are seen for the two neighboring round (Al-Cu-Mg) particles (Figure 4.8(a)), where 'black holes' have become manifested on the particle to the right. Of all the regions on the sample, the greatest concentrations of silane are detected at the black holes, where etching appears to have allowed a beneficial morphology for adsorbing the silane. The dissolving of the round-shaped particles is evidenced by Auger measurements for the various regions identified as A and B in Figure
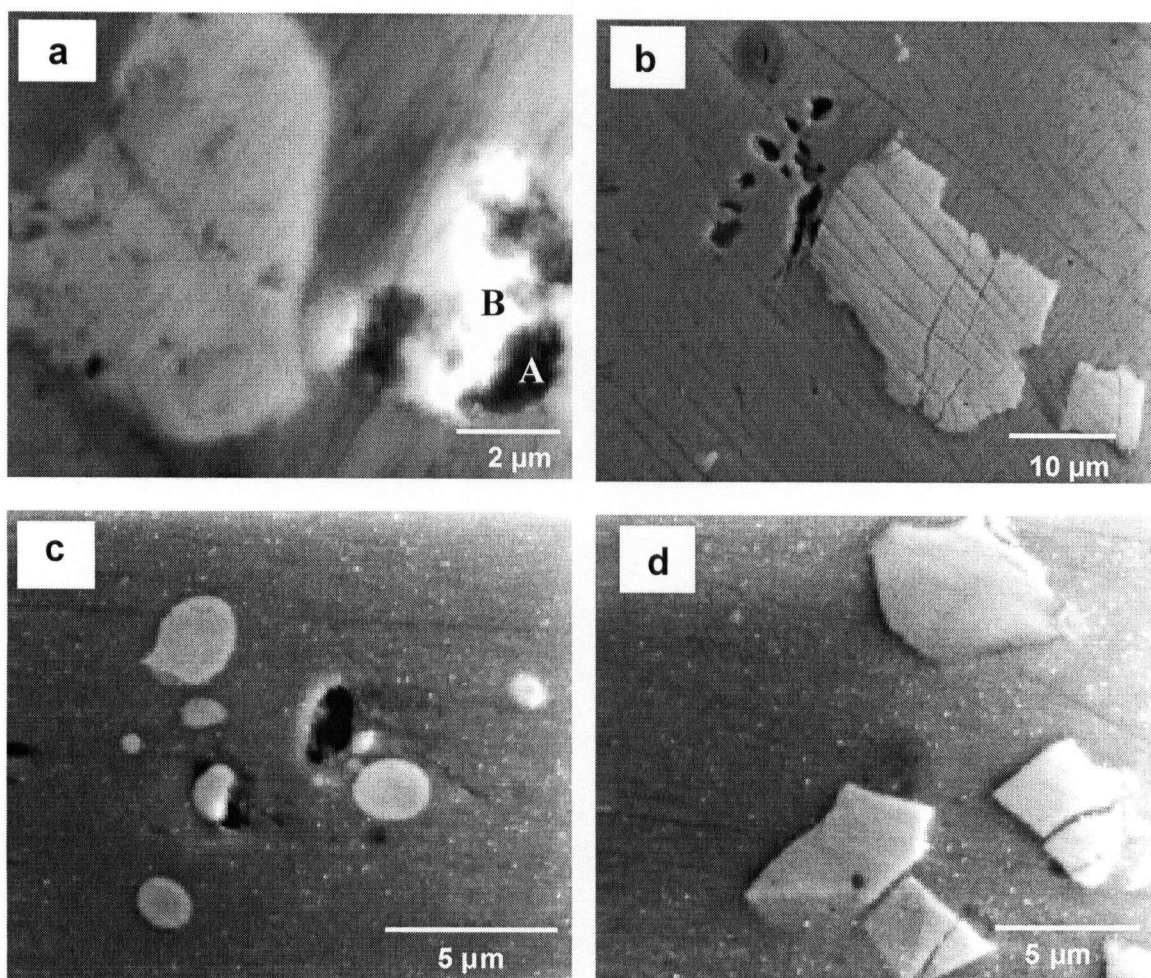
Figure 4.8. SEM micrographs from 7075-Al alloy surface after coating showing: (a) round particles and (b) irregular particles coated with 1% BTSE; (c) round particles and (d) irregular particles coated with 1% γ-GPS at pH 5.7.

4.8(a). Auger point analysis for the black region A detected only Al, O, Si and Cu, whereas Mg was detected in addition at the light region B. This suggests that the structures giving rise to the black holes were formed from Mg dissolution in the BTSE solution at pH 4.3 [17]. Such dissolution is not unexpected; others have reported that the Al-Mg-Cu particles are anodic with respect to an Al matrix, and that Al and Mg dealloying occurs from this type of particle during immersion in neutral sodium chloride solution [7].

Figure 4.8(a) shows that the black hole regions occur especially at the edges of the Al-Mg-Cu particles, and this reinforces the idea that the Mg dissolution starts at the particle-matrix interface where the galvanic coupling is strongest. Dissolution of Mg at the particle's edge depends on the proximity of Al in the matrix, which is electrochemically more stable than Mg. The left round particle in Figure 4.8(a) shows small black regions across its extent, although they are smaller than those on the particle to the right.

4.3.3 Coating of Air-oxidized 7075-Al with 1% γ-GPS

Following the observation that BTSE at its natural pH (4.3) can coat all regions of the 7075-Al alloy surface, there was interest in comparing with γ-GPS at its natural pH (5.7). Figures 4.8(c) and (d) show SEM micrographs measured after coating with 1% γ-GPS, and the main difference from the situation prior to coating was the presence of some nodules (white dots, <50 nm) seen on the surface. Although Si Auger signals were detected from the nodules, no Si content was detected on the other regions of the sample surface. Consistently, the overall amount of silane detected by XPS (Si/Al ratio 0.20)

was small in comparison to the situation with BTSE. Since Si was not detected from most of the surface, it may perhaps be concluded that the pH value used was not favorable for hydrolysis. Other studies have reported that to coat Al surfaces with 1% γ-GPS, the solution pH should be reduced to at least 5 [9, 62, 64, 137]. As well, many silanes are known to hydrolyze rapidly and polymerize slowly at pH 4, but at higher pH values both reactions can be fast [35-37]. At the pH used in this part of the project (5.7), the silane polymerization reaction may have been more prominent compared with the situation for lower values, where more etching of oxide and protonation of the surface to give Al–OH groups is expected. It is likely that the nodules are due to silane condensation and precipitation in polymeric form on local regions of the matrix. The pH of the γ-GPS solution increased from 5.7 to 5.9 during etching in the coating process, and this also emphasizes the need for a lower starting pH in order to coat the various micro-regions of 7075-Al with this silane (Table 4.2).

Table 4.2. pH measurements and Si/Al ratio for the mirror-polished samples coated with γ-GPS.

	pH measurements		Si/Al	
1% γ-GPS	Before coating	After coating	Before rinsing	After rinsing
At natural pH = 5.7	5.7	5.9	0.20	0.16
pH = 4.5	4.5	4.6	0.40	0.34
pH = 3.2	3.2	3.2	7.62	7.31
Heat pre-treated (pH = 5.7)	5.7	5.7	1.24	1.20

The study of the coating process for 1% γ-GPS on 7075-Al alloy was extended by adjusting the solution pH to the lower value of 4.5. XPS measurement for the total

amount of silane adsorbed showed that the Si/Al ratio increased to 0.40, and the pH changed from 4.5 to 4.6 during this process (Table 4.2). When the ultrasonic rising test was applied to the coated surface, the Si/Al ratio from XPS reduced to 0.34, which is still indicative of a moderate level of adhesive bonding according to this test [112].

Figures 4.9(a) and (b) show SEM micrographs of the Al surface coated with 1% γ-GPS at pH 4.5. The matrix region shows the presence of dark and grey regions (Figure 4.9(b)). SAM measurements detected Si from both the dark and grey areas of the matrix region where, on average, the dark areas showed higher amounts of Si than on the grey areas, consistently with another study for the 2024-Al alloy [74], and this indicates a non-uniform coating. Some small black holes were also observed (Figure 4.9(a)) and large amounts of Si were detected at these regions. It is of interest to note that Si was detected on the irregular-shaped particles but not on the round particles. Measurements from the latter showed that the coating resulted in a reduction in the Mg content when compared with the situation starting at the natural pH (5.7). This is fully consistent with the expected increase in Mg etching when starting at pH 4.5.

SAM measurements from the irregular particle after coating with γ-GPS showed Al and Fe signals, although the latter was in too small an amount to identify whether it was in the metallic or oxide form. However, the Auger spectrum for Al does confirm that this element is in the oxidized form at the particle's surface, consistently with conventional ideas [141]. In principle this oxidized Al could form the Al–O–Si bonding upon reaction with Si–OH, thereby leading to the silane coating on the irregular particles. No coating was observed on the round particles, possibly because at this pH the etching reaction of the Mg dominates over both protonation of the Al oxide and the coupling
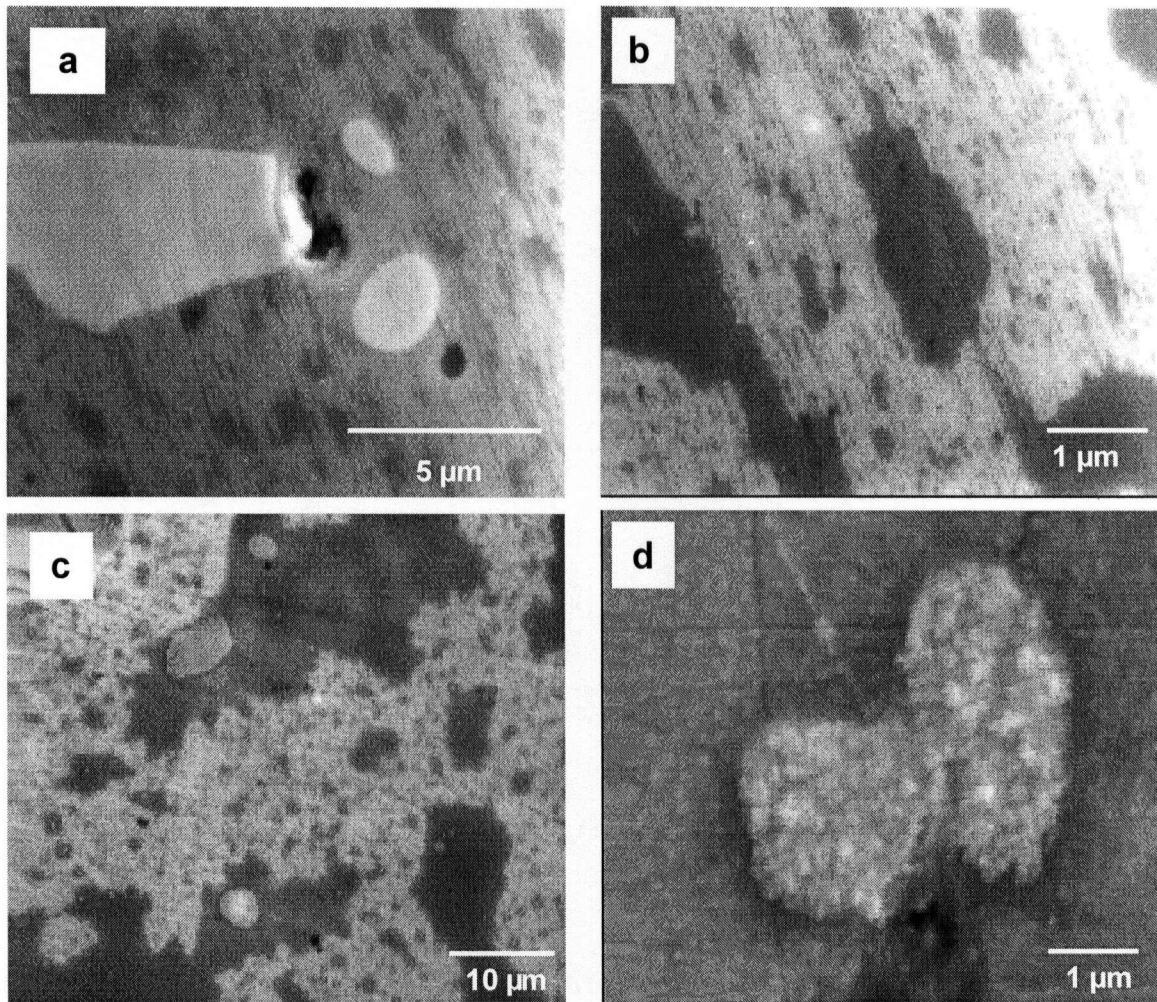
Figure 4.9. SEM micrographs from 7075-Al alloy samples: (a) air-exposed then coated with 1% γ-GPS at pH 4.5; (b) as for (a) except for focusing on a matrix region; (c) air-exposed then coated with 1% γ-GPS at pH 3.2; and (d) heated to 200°C.

reaction of Al–OH and Si–OH. This may imply that the surface Mg must first be etched away before a γ-GPS coating will form on the round particles.

The initial pH of the 1% γ-GPS solution was next lowered to 3.2. XPS measurements of the total amount of Si adsorbed on the 7075-Al sample showed an increased value for the Si/Al ratio (7.6), and this value decreased by 4% after the sonication test (Table 4.2). Furthermore, the pH measurements for the γ-GPS solution before and after the sample was immersed in the coating solution showed no detectable change. Figure 4.9(c) shows the SEM micrograph from this coated surface; the overall morphology is similar to that in Figures 4.9(a) and (b) where the dark and grey regions are observed on the matrix indicating a non-uniform coating. One notable difference was that the sample coated at pH 3.2 showed dark regions covering the round and irregular shaped particles. The Auger measurements showed that Si content was detected on all areas of the sample, even on the round particles. In addition no Al signal, or signals from other intermetallic elements, was detected by SAM, so indicating that the Si coating was thicker than the experimental probe depth (<10 nm). This process gave the thickest coating for all samples mentioned so far using γ-GPS on 7075-Al. It can be inferred that at pH 3.2, enough H^+ ions are present to be used for: (i) etching the Mg from the round particles to expose Al oxide, and (ii) protonating the oxide to give Al–OH for coupling with the Si–OH.

4.3.4 Effect of Heating 7075-Al and Coating with 1% γ-GPS

In the previous section, a variation in the pH of the 1% γ-GPS coating solution was made in order to assess conditions for coating all micro-regions of the air-oxidized

surface of 7075-Al alloy. Another possibility is to modify the pre-treatment. Exploration is given here to heating the mirror-polished sample at 200°C in air for 15 min. Compared to the air-oxidized sample, the heated sample portrayed rougher surfaces for the matrix and round particles (Figure 4.9(d)), but less change for the irregular particles.

Auger point analysis for the heated surface showed some interesting differences when compared to the polished surface that had just been exposed to air at room temperature. Prior to heating, Mg content was identified only on the round particles, but after heating Mg was detected on the matrix and the irregular particles as well. This implies Mg migration, either on the surface from the round particles to the other regions, or from the bulk. Furthermore, although most of the round particles showed the expected Cu, Al, Mg contents, the round particle in Figure 4.9(d) showed an additional Zn content. For the matrix region after heating, Al was detected as previously found, but so was Mg, Zn and Si. The last mentioned element definitely indicates that migration from the bulk has occurred. Surprisingly, no Zn content was detected from the irregular particle after heating, but clearly the heating led to an appreciable redistribution of the alloying elements compared with the situation for the air-exposed surface.

There have been many studies on the effect of heating Al alloys in relation to mechanical properties, for example solution heat treatments (e.g. salt bath and water, 500-600°C) [5, 9, 13, 14]. In contrast, the present work has the different emphasis of investigating whether lower-temperature heating may result in changes that can improve silane adsorption for protective purposes. The segregation of Mg and Zn observed here at 200°C relates to observations by Andreatta et $al.$ that, on heating to 470°C, $MgZn_2$-strengthening particles in 7075-Al alloy lead to Zn and Mg enrichment in the matrix [5].

Also, for the 2024-Al alloy, Li *et al.* noted that alloying elements such as Mg will dissolve into the Al matrix on heating [13]. However, these other observations involved heating to higher temperatures (465-495°C) than considered here, and they did not apply specifically to the surfaces involved.

To investigate further the effect of heating on the air oxidized (native oxide) surfaces, local Auger scans were measured for the elements in each of the three micro-regions, and compared with those from a polished surface that had not been heated. It is noted that the Auger signals measured for the micro-regions show less intensity compared to the previous cases due to the thicker oxide that formed (surface charging). For Al in the matrix region, one notable effect of the heating is that the spectrum shows an increase in the structure that corresponds to Al oxide (at ~1388 eV kinetic energy, Figure 4.2). In fact the peak from metallic Al (~1394 eV) is barely detected for the heated sample. It is clear that the heating treatment oxidized the surface much more than the 20 h exposure at room temperature.

For the round particles, comparison of Al spectra also points to an increase in the peak at 1388 eV for the heated sample (Figure 4.3). Also no metallic Mg structure is detected in the Auger spectrum from the heated sample, and correspondingly all Mg detected at this type of particle is in the oxidized form (Figure 4.4). Thus for the round particle, Mg oxidizes more than Al. The Cu spectrum from the round particle after heating has lower intensity, without significant change in structure (Figure 4.5), apparently supporting the idea that the formation of Mg and Al oxides acts as a protective layer for the Cu. For the irregular particles, the Al spectra give similar observations to the other micro-regions in that the oxide component is increased significantly after

heating (Figure 4.7), while the Fe spectrum shows reduced intensity (Figure 4.6). The results from both the irregular and round particles suggest that Mg and Al preferentially oxidize at the surfaces, and provide protective layers to other elements below.

When the pre-heated 7075-Al sample was treated with the 1% γ-GPS solution at the natural pH of 5.7, XPS study showed a value for the Si/Al ratio (1.2) that was increased six-fold compared with when the air-oxidized surface was exposed to the same silane solution (Table 4.2). During coating on the pre-heated sample, the solution pH increased by only 0.04 from the starting value. It is also very significant that the Auger measurements showed that Si was detected on all areas of the surface, although the alloying elements were not detected, possibly because of the predominant Al oxide below the silane. These observations show that heating can modify the mirror-polished surface such that adsorption from 1% γ-GPS can be achieved on all micro-regions at the natural pH of 5.7. Furthermore, after the ultrasonic test, the Si/Al ratio from XPS dropped by only 3%. Apparently the increase in oxide from the heating enhanced the silane adsorption compared with the air-exposed mirror-polished sample treated at pH 5.7, although the total adsorbed silane on the pre-heated sample remained less than when the γ-GPS was applied at pH 3.2 to the non-heated sample. More silane adsorption in the latter case follows from the increased concentration of H^+ ions for protonation of the oxide surface (to form Al–OH); also the increased etching possible will give more roughness which may increase adsorption by the mechanical interlocking mechanism.

4.3.5 TOF-SIMS Study for Covalent Bonding at the Silane-alloy Interface

Although SAM provides a surface sensitive technique for studying the distribution of silane on different micro-regions of the alloy surface, it does not distinguish silane adsorbed via direct metal–O–Si covalent bonding from adhesion based on physical bonding within a rougher surface morphology. In principle, insight into the nature of the adsorption can be provided by TOF-SIMS measurements. For example, the presence of $AlOSi^+$ among ions sputtered from a silane-oxide interface, after the outermost layers have been sputtered off, provides a very strong indication that the Al–O–Si bonding arrangement is present at the interface, as required for direct covalent bonding between the silane and an oxidized surface of Al [67, 110].

For these SIMS measurements, the silane-coated samples were first sputtered, over a 300 μm x 300 μm area, using SF_5^+ ions to remove the outer layer of coating and to expose the interface region. The use of the SF_5^+ source is chosen to sputter the surface while minimizing surface damage [143]. After sputtering, spectra in the high-mass resolution (bunched) mode were obtained from a 50 μm x 50 μm area within the sputtered region, and additional images were obtained for ions associated with the elements of interest (specifically Mg, Cu, Fe and Zn) from the same area in order to confirm the location of the particles (Figure 4.10). The Cu- and Fe-rich regions shown in the ion images served as an indicator of the round and irregular second-phase particles respectively, whereas regions without these elements identified the matrix region. Analyses were performed on sputtered species that originated from each of the Cu and Fe rich regions, and the matrix region, in order to investigate specific fragments indicative of direct metal–O–Si bonding in each of these local regions.
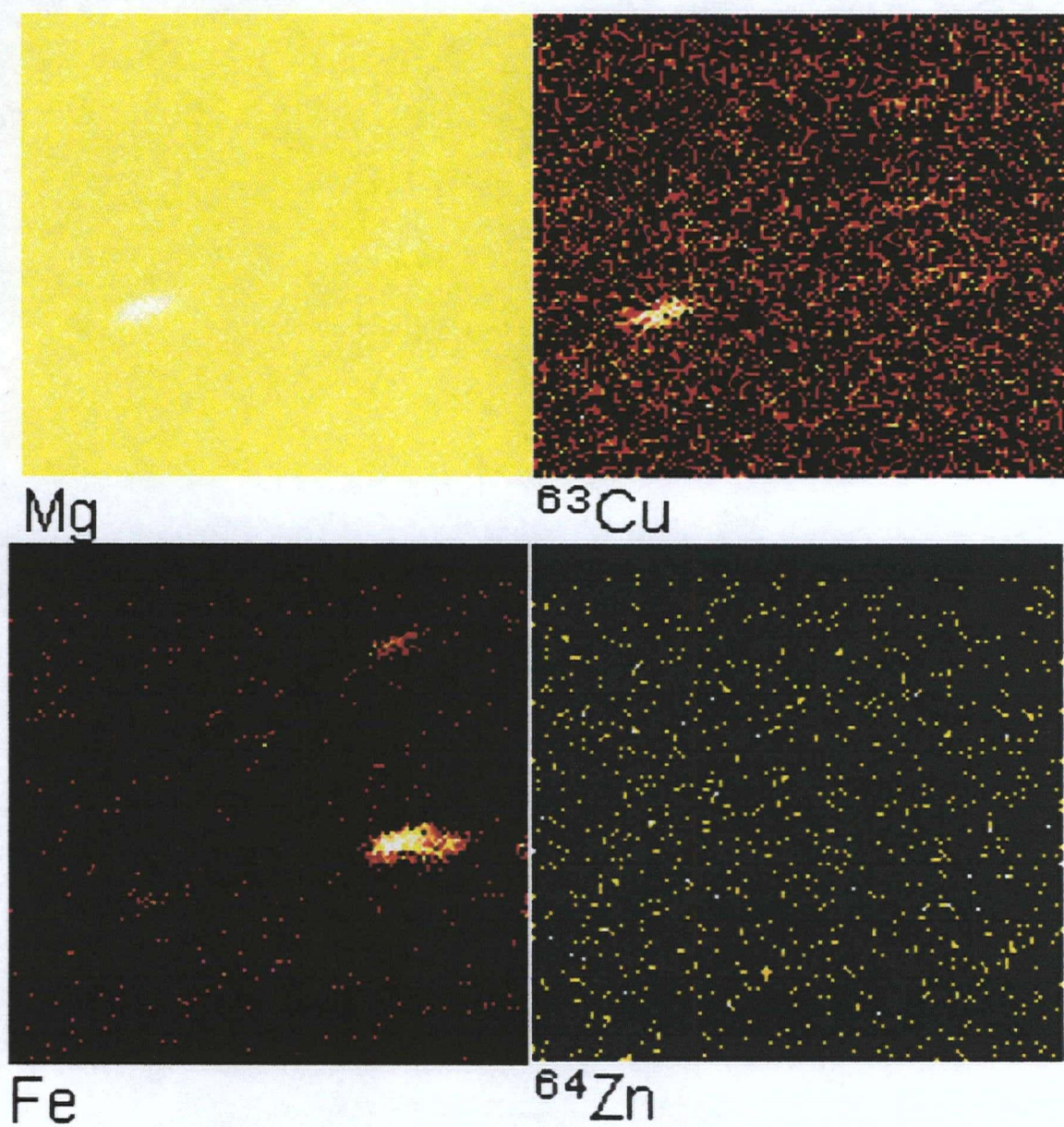
Figure 4.10. Ion images from heat-treated 7075-Al sample coated with 1% γ-GPS at pH 5.7.

Three samples, for which the earlier-described work showed silane adsorption on all micro-regions, were chosen for study by TOF-SIMS. These specific samples for the 7075-Al alloy were: (i) coated with BTSE (pH 4.3), (ii) coated with γ-GPS (pH 3.2), and (iii) heated prior to coating with γ-GPS (pH 5.7). For each sample, a search was made in the mass spectrum, from each micro-region, for the presence of ion fragments indicative of the possible metal–O–Si interfacial bonding. Peak identification was done on the basis of the theoretical mass of the ion fragments and a structure was accepted only if the difference between the observed and theoretical masses was less than 0.003 amu [67], and if the masses of other fragments that could possibly be present, with the same nominal mass, matched noticeably less well.

For the BTSE-coated samples of 7075-Al, TOF-SIMS measurements for the matrix region indicated the presence of Al–O–Si bonding, although no evidence was detected for other metal–O–Si bonding interactions. The observed experimental mass for $AlOSi^+$, 70.9530 (Figure 4.11), differs from the theoretical mass (70.9534) by only 0.0004 amu, and it is well separated (by more than 0.01 amu) from other species with the same nominal mass of 71 amu, namely $AlSiCH_4^+$ (70.9898) and Al_2OH^+ (70.9658). The Al–O–Si bonding was also detected on the irregular particle. In addition that particle showed a comparatively weak signal at mass 99.9055 (Figure 4.12); this can be attributed to $FeOSi^+$ with a theoretical mass of 99.9068. The discrepancy of 0.0013 amu is small compared with those for other fragment ions associated with a nominal mass of 100, namely FeO_2C^+ (99.9248) and Si_3O^+ (99.9256), which differ by about 0.02 amu from $FeOSi^+$, thereby supporting the presence of Fe–O–Si bonding to the irregular particles. This is consistent with Fe being detected by SAM prior to the coating, but apparently
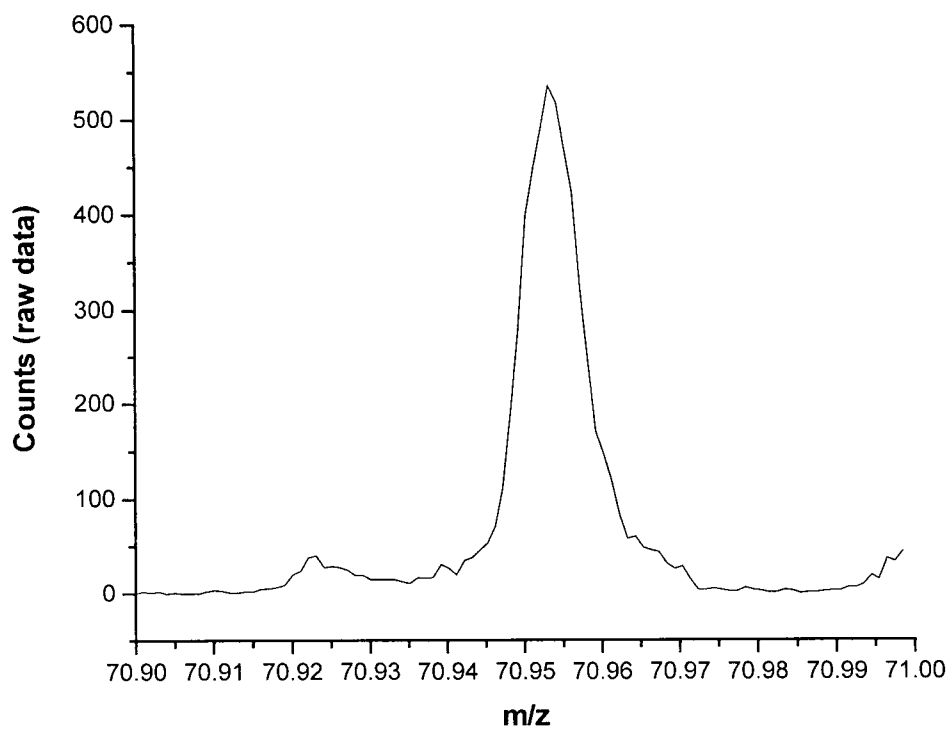
Figure 4.11. TOF-SIMS measurement of $AlOSi^+$ fragment near nominal mass m/z equal to 71.
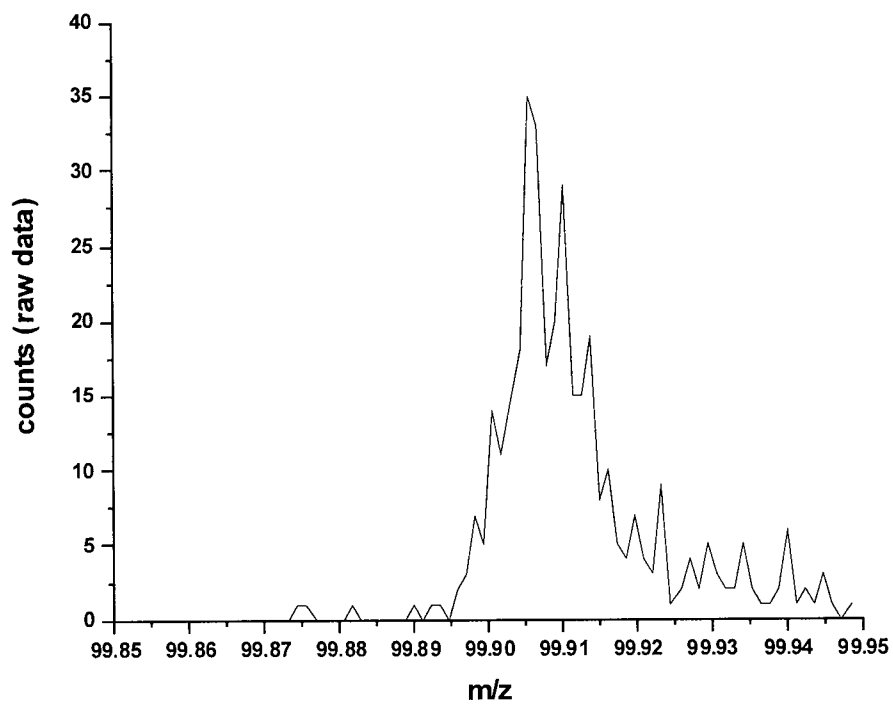
Figure 4.12. TOF-SIMS measurement of $FeOSi^+$ fragment near nominal mass m/z equal to 100.

Al–O–Si bonding dominates to the irregular particles. On the round particles, SAM showed the presence of Cu, Mg and Al prior to coating, but the SIMS analysis for this region after BTSE coating showed only the AlOSi$^+$ fragment. The corresponding MgOSi$^+$ species was not detected, presumably because, during immersion in the silane solution, the etching of Mg dominated over the coupling reaction between Mg–OH and Si–OH. Further, the non-observance of CuOSi$^+$ ions from this region supports the idea in Section 4.3.1 that after air oxidation, but before the silane treatment, Al oxide forms a protective layer on the particle. Then during the etching associated with the silane coating process, the Al oxide likely protected the Cu from being directly exposed to the acidic solution, thereby limiting chances for the Cu–O–Si bond formation. To summarize for the air-oxidized sample that had been coated by BTSE, covalent Al–O–Si bonding existed on all three micro-regions of the 7075-Al surface, with a small contribution of Fe–O–Si bonding to the irregular-particle region.

For the sample that had been coated with γ-GPS at pH 3.2, all three micro-regions showed the presence of AlOSi$^+$, but no analogous fragments were detected for the other metals. The presence of Al–O–Si bonding to the matrix and the round-particle regions is expected, but the absence of Mg–O–Si and Cu–O–Si bonding to the latter region is not unexpected at that pH, where the surface Mg has probably been etched away and the Cu may be covered by Al oxide. In principle Fe–O–Si bonding could exist on the irregular-particle region, but its detection probability may have been reduced by enhanced surface roughness [110] from etching at the low pH.

The sample that has been heated prior to being coated by γ-GPS solution (natural pH of 5.7) showed Al–O–Si bonding and Mg–O–Si bonding at all three micro-regions.

Figure 4.13 shows the detection of $MgOSi^+$ (mass fragment at 67.9578) from the matrix region. This differs by 0.0009 amu from the theoretical mass (67.9569), but by 0.02 amu or more from other potential fragments for nominal mass 68 amu, namely $Mg_2OH_4^+$ (67.9963) and MgO_2C^+ (67.9749). The detection of Mg–O–Si in the matrix region is not unexpected since the heated surface showed Mg in the matrix region prior to coating and in this experiment etching will be reduced at pH 5.7. The intensity of $MgOSi^+$ is less than that of $AlOSi^+$, and that may suggest that most of the silane bonding is via Al–O–Si interactions. The detection of Mg–O–Si bonding on both the irregular and round particles is consistent with the (oxidized) Mg content indicated by SAM in these two regions. The absence of other types of metal–O–Si direct bonding is probably a consequence of the Mg and Al forming an uppermost protective layer.

4.4 Concluding Remarks

The work reported in this Chapter aims to probe more fundamental aspects of the adsorption of organosilanes on surfaces of 7075-Al alloy, and accordingly mirror-polished samples were used since that enables the basic microstructure to be imaged with SEM. The emphasis has been particularly on comparing behaviors at the Al-Cu-Mg (round) and Al-Fe-Zn (irregular) second-phase particles with those at the alloy matrix, which is dominantly composed of Al. Evidence has been presented to show that these different regions can behave quite differently. Further, those differences extend also to the particular pre-treatment applied prior to the exposure to the silane. Scanning Auger microscopy (SAM) has been shown to be powerful for identifying these variations, and that includes for the virgin surface which can be assessed by a gentle sputtering to
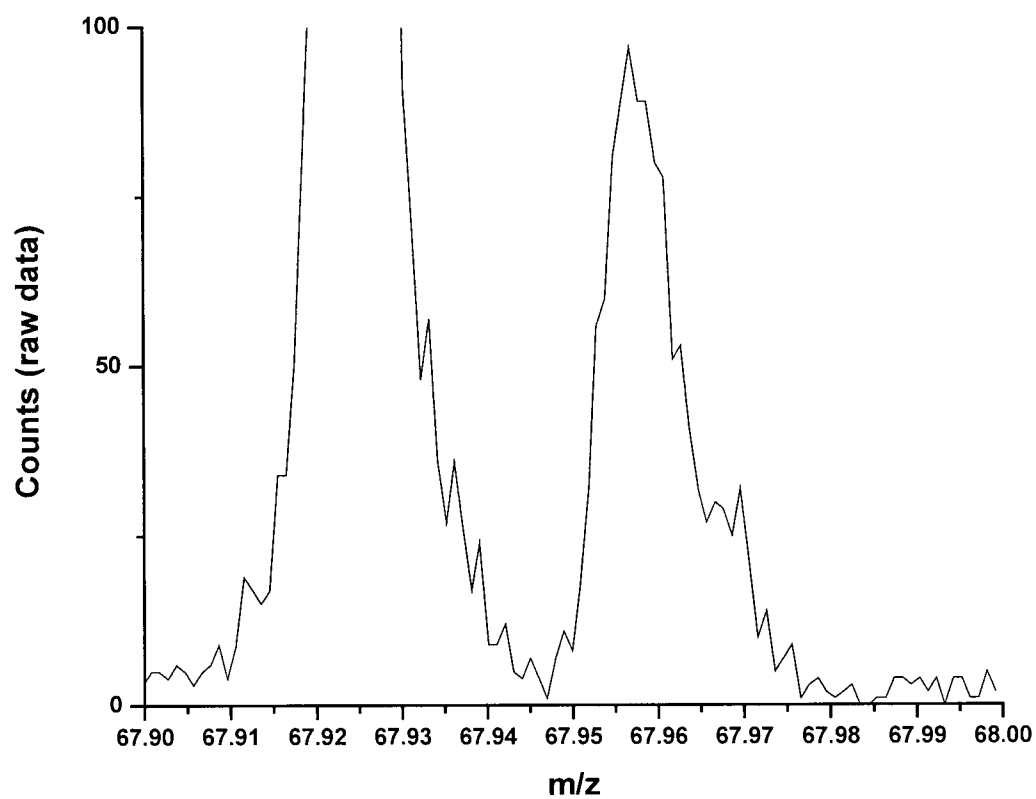
Figure 4.13. TOF-SIMS measurement of $MgOSi^+$ fragment near nominal mass m/z equal to 68.

remove any extra elements (e.g. O or C contamination) prior to the Auger analysis. Such a surface provides reference points for assessing the natures of the different regions after the various pre-treatments considered. Air exposure at room temperature results in oxidation of all micro-regions. On the round particle, the Cu is apparently protected by the Mg and Al oxides formed above, while on the irregular particle the oxidation of Al is sufficient to prevent detection of the underlying Zn to the SAM probe depth (<10 nm).

This work identified examples where the details of the organosilane used affected the degree of coverage on the various microstructural regions of the 7075-Al alloy surface. For BTSE solution at its natural pH (4.3), complete coverage occurred with no detectable dependence on the chemical composition of the different regions of the surface. The situation differed for γ-GPS, where the coverage depended not only on the chemical composition of the micro-regions but also on the pH of the coating solution. With γ-GPS solution at the natural pH (5.7), coating was observed only at isolated nodules (<50 nm dimension), apparently due to polymerization at some particular areas of the surface. For γ-GPS at the lower pH of 4.5 etching of the surface was increased, particularly for Mg, and that led to coating of the matrix and irregular particle regions, but not on the round particles. For γ-GPS at pH 3.2, the etching of Mg from the round particle appeared to be sufficient to ensure a complete silane coverage over the whole surface. Even though other studies have reported that coating requires the γ-GPS pH to be adjusted to 5 [17, 61, 109], the present work provides evidence that lower values are needed for coating all micro-regions of the 7075-Al surface investigated. Also, there are indications that selective coating may be feasible.

The sample that had been heat treated (200°C for 20 min) prior to coating showed significant oxide growth on all micro-regions, and this was accompanied both by Mg and Zn segregation on the surface and by an increase in surface roughness. A complete γ-GPS coating could be achieved on this surface without any adjustment to the natural pH, and the increase in Mg content (at the higher pH) played a role in forming the interfacial metal–O–Si covalent bonding. This was probed by TOF-SIMS, and we believe it provides the first assessment of such bonding at the local micro-regions of an Al alloy surface. Adsorbed BTSE showed Al–O–Si bonding over the whole of the surface, with some Fe–O–Si bonding on the irregular second-phase particles. For γ-GPS at pH 3.2, only Al–O–Si bonding was recognized from all regions, while when that silane was applied at its natural pH (5.7) to the heat-treated sample, evidence was presented for both Al-O-Si and Mg-O-Si types of interfacial bonding.

Chapter 5 Characterization of AZ91 Magnesium Alloy and Organosilane

Adsorption on its Surface†

5.1 Introduction

The discussion in Chapter 1 suggested that the low density and high specific stiffness of magnesium-based alloys make them potentially attractive for the automobile industry, although that must be balanced by their susceptibility to corrosion. This Chapter is involved with the characterization of one particular alloy of this type, namely that known as AZ91 whose nominal composition is 9 wt% Al, 1 wt% Zn, small amounts of other elements and approaching 90 wt% Mg.

Prior to assessing various coatings on the AZ91 surface, it is important to have knowledge for its basic oxidation behavior, including the native oxide that forms in air. While much research has been done on the oxidation of pure Mg and Al metals [120, 144-150], to date there are few reports on the formation of oxide on the AZ91 alloy [150, 151] and how the oxidation is affected by the presence and distribution of Al and Zn. Scanning Auger microscopy (SAM) has an important role to provide this type of information, and thereby to complement the less surface sensitive work that has been done using energy dispersive X-ray (EDX) spectroscopy [16, 75]. Also, coating studies involving organosilanes on the Mg alloys are scarce [63, 72], and to the best of our knowledge such studies have not yet been undertaken on AZ91 alloy with the more surface specific techniques.

The first objective of the investigation reported here is to learn more about the nature of the surface oxide on the AZ91 alloy. This involves two parts: (i) oxidation of

---

† The work in this Chapter is currently being prepared for publication.

the alloy surface in an ultra-high vacuum (UHV) environment, and (ii) thermal stability of oxide formed on this alloy surface. The second objective is to investigate chemical composition of a AZ91 alloy surface, including across its microstructure, as well as in cross section, and to characterize silane-coated samples. Three organosilanes were used, namely bis-1,2-(triethoxysilyl)ethane (BTSE), γ-glycidoxypropyltrimethoxysilane (γ-GPS) and γ-aminopropyltriethoxysilane (γ-APS). Analyses with SAM and X-ray photoelectron spectroscopy (XPS) are used to characterize the AZ91 surfaces before and after application of the silane coatings, and that is complemented by the use of energy dispersive X-ray (EDX) spectroscopy and scanning electron microscopy (SEM), in order to make progress in relation to the objectives mentioned above.

5.2 Experimental

The AZ91 alloy used in this work was standard test plate provided by Professor J. Metson (University of Auckland) who received from a commercial supplier. Samples of dimension 1 cm x 1 cm were mirror polished (~1 μm roughness) prior to any treatment. For the oxidation study, this alloy surface was first cleaned in the ultrahigh vacuum (UHV) chamber by cycles of Ar^+ bombardment, followed by annealing at 200°C, until no O and C signals were detected by XPS. The surface was then dosed for 5 min with high-purity O_2 gas (Matheson) at different pressures ($10^{-8}, 10^{-7}, 10^{-6}$ and 760 Torr) while the sample was held at room temperature, and each oxygen dose was followed by cleaning and annealing at 200°C. To study the thermal stability of the native oxide, the mirror-polished surface, which had subsequently been exposed to air for 20 h, was heated in the ultrahigh vacuum (UHV) chamber for 5 min to different pre-determined temperatures

(100°C, 150°C, 200°C, and 240°C), and cooled back to room temperature before XPS measurements were made. For the cross section analysis of the sample, the AZ91 panel was immersed in liquid nitrogen for 5 min, then fractured and immediately transferred to the UHV chamber.

Silane solutions (1% BTSE , 1% γ-GPS and 1% γ-APS) were prepared by mixing 1 vol % silane (Aldrich), 93 vol % methanol (HPLC grade, Fisher Scientific) and 6 vol % distilled water (correspondingly the 4% BTSE solution was formed by mixing BTSE, methanol and distilled water in the volume ratios 4:90:6). After the initial mixing, each solution was stirred for 5 h at room temperature to ensure complete hydrolysis. Each coating was applied by immersing a mirror-polished sample, which had been exposed to air for ~20 h, into the freshly-hydrolyzed silane coating bath for 1 min, removed and dried in nitrogen. Solution pH values were measured with a pH meter (Orion Benchtop, model 420A), and the natural values for 1% BTSE, 1% γ-GPS, 1% γ-APS and 4% BTSE were 4.3, 5.7, 10.4 and 3.9 respectively. An initial assessment of the silane adhesion to the AZ91 surface was indicated by a simple rinsing test. After samples were coated, they underwent an initial XPS analysis, and were then subjected to an ultrasonic rinse in distilled water for 30 min using a sonication bath from Solid State/Ultrasonic (model T14B, L&R Manufacturing). On removal from the bath, each sample was dried in nitrogen prior to testing further with XPS.

XPS spectra were measured with a Leybold MAX200 spectrometer (base pressure 2×10^{-9} Torr) using the Al Kα source (1486.6 eV) operated at 10 kV and 20 mA emission current. Survey spectra were measured with the pass energy set at 192 eV, while a pass energy of 48 eV was used for measuring the Al 2p, O 1s, Mg 2p, Mg 1s, C 1s

photoelectron spectra, as well as the Mg KLL Auger spectra. For the oxidation study in UHV, XPS binding energies were referenced to the Mg 2p metallic peak at 49.75 eV to avoid issues with differential charging that can occur during this project. For the thermal stability study, the binding energy calibration used structure from the adventitious hydrocarbon contamination that is still present, and its C 1s was set to 285.0 eV. SAM and SEM analyses were performed with the Thermo Electron Microlab 350 spectrometer equipped with field emission source and hemispherical energy analyzer. Auger point analysis was done using a primary electron beam at 10 kV and 4 nA (sample current) with the energy analyzer operated in the constant retarding ratio mode, with the ratio set at 4. EDX (and some SEM) measurements were made using a Hitachi S3000N microscope using 20 keV incident electron beam, and elemental amounts were compared on an atomic percentage basis after making standard sensitivity factor corrections.

5.3 Results and Discussion

This whole section divides into two main parts. In Part I (Sections 5.3.1 and 5.3.2) XPS is used to give an overall view of the oxidation behavior of a cleaned AZ91 alloy surface its stability on heating, while in Part II (Sections 5.3.3 and 5.3.4) SAM is used to probe chemical analysis at the micro-structural level for the AZ91 surface, including after silane coating.

5.3.1 Oxidation of a Cleaned AZ91 Alloy Surface

Figure 5.1 shows the O 1s, Al 2p, Mg 2p and X-ray induced Mg KLL Auger spectra of the AZ91 alloy surface when cleaned and after a 5 min dose of O_2 at various
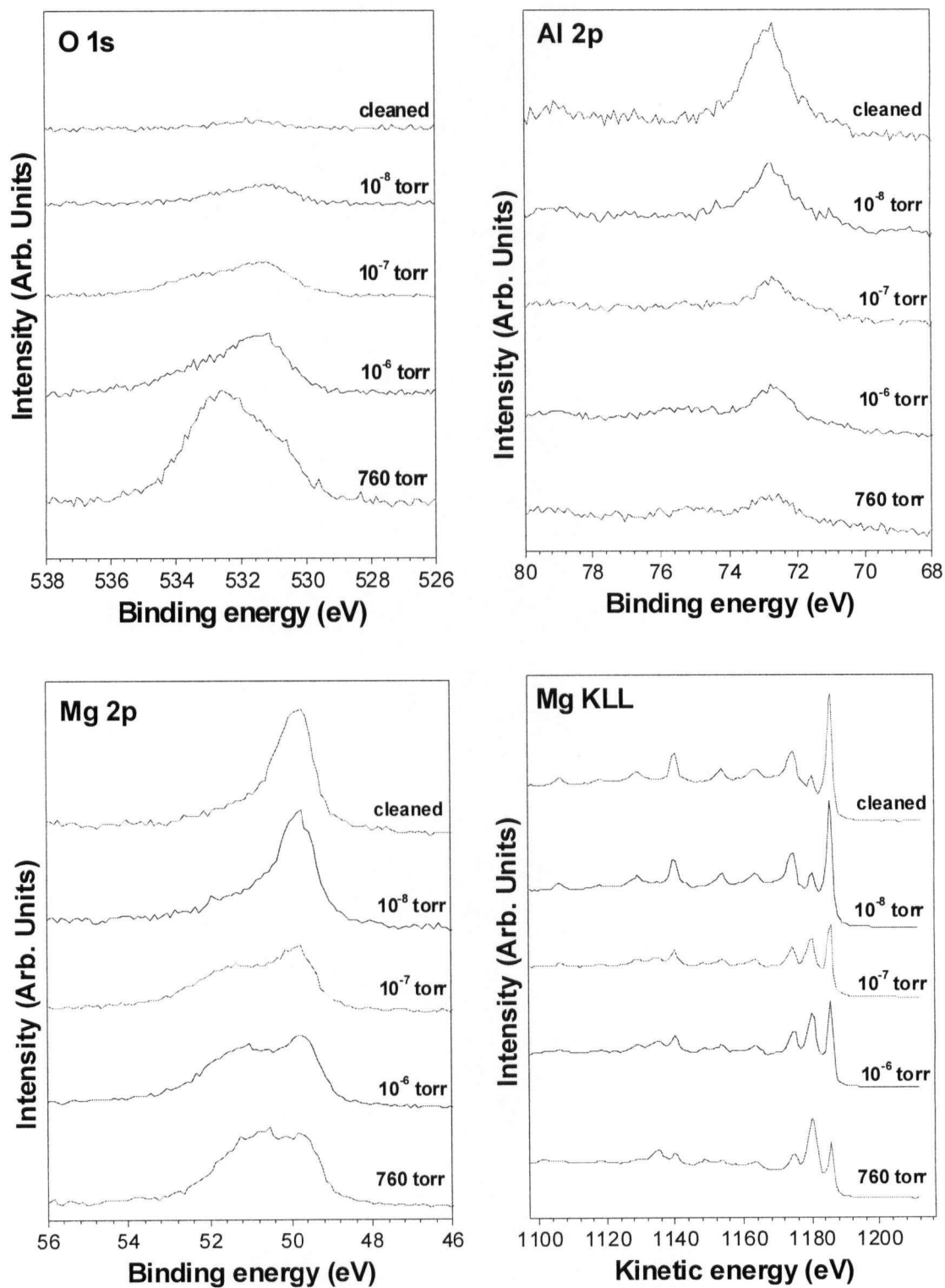
Figure 5.1. O 1s, Al 2p, Mg 2p and Mg KLL spectra from AZ91 alloy surface after exposure to O_2 for 5 min at different pressures.

pressures ranging from 10^{-8} to 760 Torr. The XPS spectra from the sputter-cleaned surface are free of O and C contamination, and the Mg 2p and Al 2p photoelectron spectra show single peaks at binding energy 49.8 eV and 72.8 eV respectively. The first is set by the binding energy reference, which is taken to equal that of pure Mg, while Al in the AZ91 alloy is shown to have a binding energy very close to that of pure metallic Al [120, 150]. The X-ray induced Auger KLL spectrum has multiple peaks, and evidence will be presented to show that the relative intensities vary with the O_2 exposure, and that they provide a good indication of the chemical state of Mg.

After the exposure to O_2 for 5 min at 10^{-8} Torr, the O 1s spectrum shows a small peak at 531.3 eV which is accompanied by growth of a shoulder at 51.2 eV in the Mg 2p spectrum. The intensities of these two structures become more prominent after the O_2 dose at 10^{-7} Torr, and these observations are consistent with surface oxide growth even at such comparatively low doses. These two peaks are interpreted as indicative of O^{2-} and Mg^{2+} species arising from MgO formed by the oxidation of the alloy surface; the latter structure is close to the binding energy of MgO (~51.0 eV) reported by others [120, 146, 149, 150]. These two peaks increase further after the dose at 10^{-6} Torr, by which point the O 1s spectrum has a second component at 533.3 eV which is believed to be due to the presence of $Mg(OH)_2$ [120, 144, 146]. The binding energy values for the two components in O 1s agree well with the values reported by others who have studied surfaces of high-purity metallic Mg [120, 144, 146].

The formation of $Mg(OH)_2$ in this work presumably arises from residual water in the UHV environment or from its trace presence in the O_2 gas. After exposing the AZ91 alloy surface to 760 Torr of O_2, the O 1s signal has grown significantly because of the

increased oxidation and the OH component becomes more dominant than that for O^{2-}. Even at this highest dose, the Mg 2p photoelectron spectrum still has a significant contribution from the metallic component which indicates that the oxide layer thickness formed at 1 atm of O_2 is less than the probe depth of XPS (~8 nm). This value is estimated as three times the inelastic mean free path, which for MgO at kinetic energy 1435 eV is taken as 2.6 nm [5].

Figure 5.1 also shows that as the exposure of O_2 increases, the Mg KLL spectrum indicates changes in relative intensity for the various peaks. For example, while metallic Mg has structure at kinetic energy 1186 eV, its intensity gradually decreases with the oxidation, a change that is accompanied by an increase in intensity for the peak at 1180 eV, and this observation is consistent with results reported by Bouvier et al. [152] for high-purity Mg. While the oxide growth on the AZ91 surface is accompanied by substantial changes in the Mg 2p, O 1s and Mg KLL spectra, no significant change occurred to the main Al 2p structure, which has a peak at binding energy 72.8 eV, as for high-purity Al. This suggests that the oxidation of the AZ91 alloy by O_2 preferentially oxidizes the Mg, while leaving the Al component relatively unreacted, an observation consistent with Mg being the more easily oxidized metal [120]. The gradual attenuation of the Al 2p signal with increasing oxidation suggests that the Mg oxide growth occurs over the Al, thereby helping to protect it. No XPS signal for Zn signal was detected on any of the cleaned or oxidized AZ91 alloy surfaces.

An example of curve fitting for a measured Mg 2p profile is shown in Figure 5.2(a), in which the Mg 2p signal is decomposed into two peaks at 49.8 eV and 51.2 eV with widths 0.9 and 2.3 eV for the metallic and oxide components respectively. The
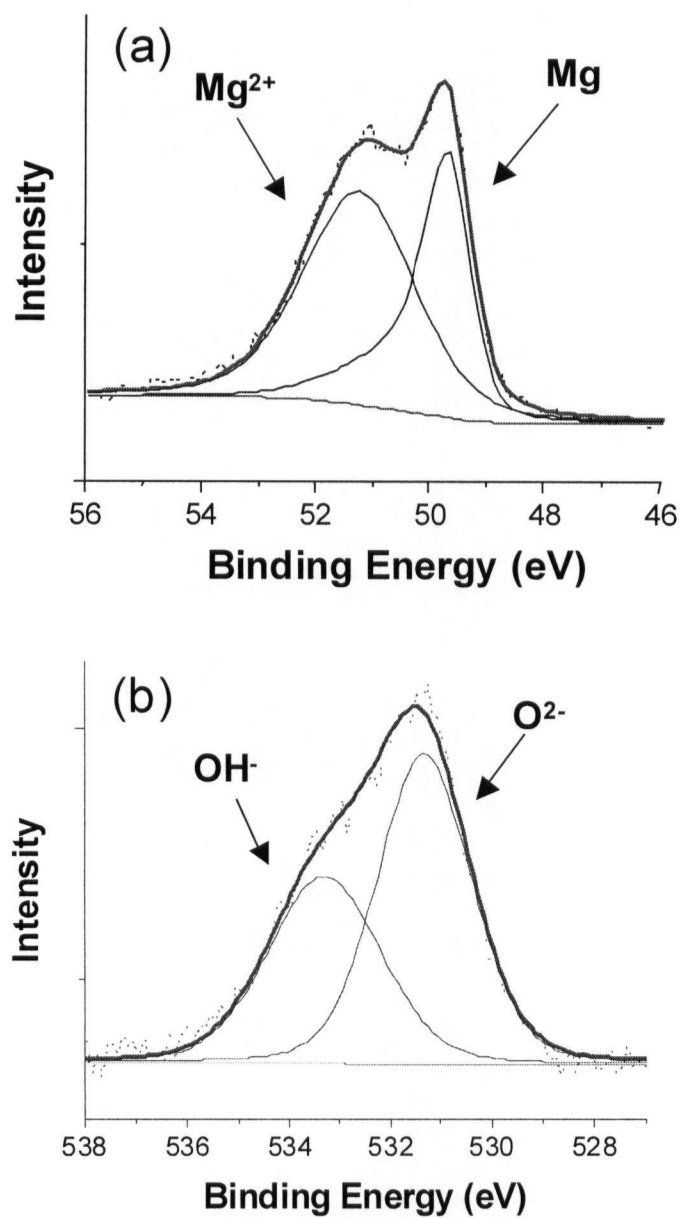
Figure 5.2. Curve fitting for an AZ91-Mg alloy after dosed with O_2 of 10^{-6} Torr for 5 min: (a) Mg 2p spectrum, (b) O 1s spectrum.

larger width for the latter component apparently indicates more than one form contributing to the oxide component. The relative oxide-to-metallic intensity ratio, from this curve fitting, can be used with Equations (2.10) and (2.11) to deduce the oxide film thickness, assuming the different inelastic mean free paths in the equations all equal to 2.6 nm. The calculated thicknesses in Table 5.1 show that the oxide layer grows rapidly in the initial stage but slows down for exposures to higher O_2 pressures. The oxide thickness plateaus at about 4.2 nm, which is close to the native oxide thickness (3.9 nm) reported after exposing Mg-8.5% Al alloy to atmosphere for a day [150].

Table 5.1. Thickness (Å) and relative proportions of O^{2-} and OH^- from XPS study of oxide formed on AZ91 after exposure to O_2 for 5 min at different pressures (Torr).

Pressure	Thickness	O^{2-}	OH^-
10^{-8}	18	0.81	0.19
10^{-7}	30	0.66	0.34
10^{-6}	34	0.58	0.42
760	42	0.52	0.48

Figure 5.2(b) reports a curve fitting for an O 1s spectrum after exposing the AZ91 surface to O_2; the O^{2-} and OH^- components are fitted to binding energies at 531.3 eV and 533.3 eV respectively, in very close correspondence with reports by Yao *et al.* [146] and Chen *et al.* [120] for the oxidation of high-purity Mg. In general, no significant difference has been detected between the O 1s signal from the AZ91 alloy surface and pure Mg. Table 5.1 reports the relative amounts of the O^{2-} and OH^- components from the AZ91 alloy after exposing to O_2 at the different dosing pressures. At 10^{-8} Torr, the O^{2-} component is dominant (81%), but this steadily decreases with increasing dosing pressure,

so that at 760 Torr the O^{2-} and OH^- components are closely similar (52% and 48% respectively).

5.3.2 Thermal Stability of Native Oxide

This part of the study focuses on assessing the thermal stability of a mirror-polished AZ91 sample that was first exposed to air for ~20 h at room temperature, and was then studied in the UHV environment of the XPS system. Figure 5.3 shows the C 1s, O 1s, Mg 1s, Mg 2p, and Al 2p spectra detected from this surface on entry (curves marked "room temp") and after heating to both 200°C and 240°C for 5 min in vacuum.

In Figure 5.3, the C 1s spectrum from the sample without heating shows two peaks: one is due to hydrocarbon contamination at 285 eV (used for referencing binding energies) and the other peak at around 289 eV is likely due to the formation of the carbonate ($MgCO_3$) [83]. The Mg 2p and Mg 1s spectra show single peaks positioned around 50.5 eV and 1034 eV respectively which correspond to Mg^{2+}, and are consistent with all the Mg being fully oxidized. In contrast, the Al 2p region shows two weak (poorly resolved) peaks at ~73 eV and ~79 eV indicating a small presence of both oxidized and metallic Al in this surface region.

After heating in UHV for 5 min at 200°C, and then at 240°C, the main peaks in the XPS spectra remain in the same positions as for the room temperature sample, but intensity changes occur as summarized by the atomic composition measurements in Table 5.2. It is noted that while the Al to Mg ratio changes only slightly (from 0.044 to 0.036), the relative proportion of carbonate C shows a small decrease, and the hydrocarbon contribution is reduced by about 36% from its initial value. The significant
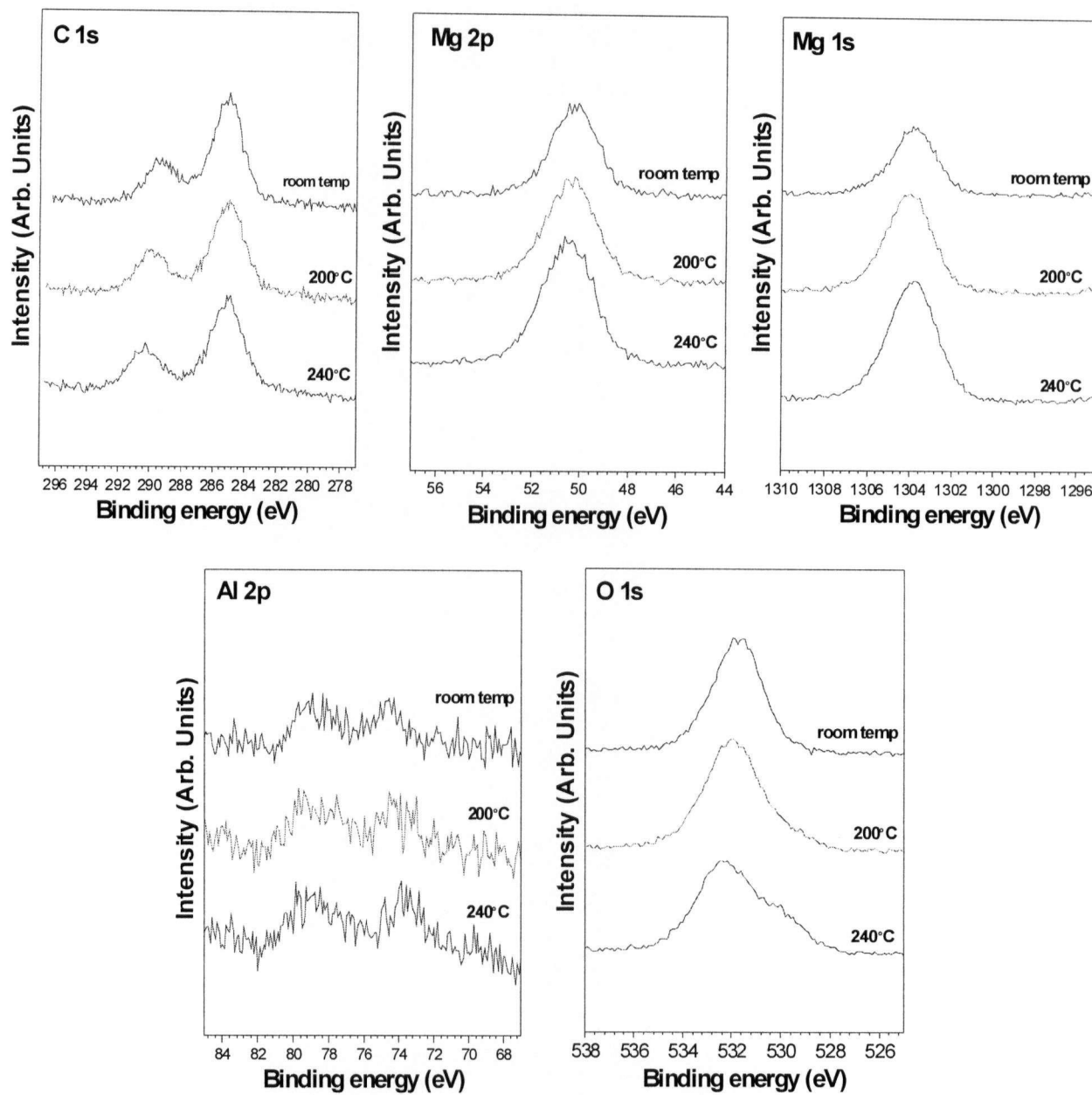
Figure 5.3. C 1s, Mg 2p, Mg 1s, Al 2p and O 1s spectra from a mirror-polished AZ91 sample at room temperature and after heating to 200°C and 240°C for 5 min in vacuum.

decrease of the hydrocarbon contribution with increasing temperature suggests that some contamination is pumped away, although it is not clear how that is binding to the oxidized surface to 200°C and above. In any event, the surface carbonate may just be beginning to decompose by 240°C. $MgCO_3$ is reported to be stable to 300°C under atmospheric conditions [52], but changes could conceivably start at lower temperatures at the surface under UHV conditions.

Table 5.2. Atomic percentage measurements by XPS for a mirror-polished AZ91 surface at room temperature and after heating in UHV for 5 min at 200°C and 240°C.

	Mg	Al	Carbonate C	Hydrocarbon
Room temperature	52.2	2.3	9.6	35.9
200°C	61.2	2.3	9.3	27.2
240°C	65.8	2.4	8.7	23.1

Peak shape analysis for the C 1s, Mg 2p, Mg 1s, and Al 2p spectra show no significant chemical state change during the heating treatment, but that for O 1s is affected by 240°C where a shoulder around 533 eV binding energy is apparent with another at around 531 eV. A curve fitting was attempted for the spectrum taken at room temperature where the spectrum was fitted with three components (Figure 5.4). A reasonable fit is obtained with two regular components at binding energies 531.3 eV (O^{2-} 49%) and 533.3 eV (OH^- 10%), and a third component at 532.1 eV (41%) which is assumed to be associated with carbonate. This already appears to be pushing the curve fitting analysis for O 1s to the limit, but a fourth binding energy component (at around 530 eV) is necessary to get a good fit for the spectrum after heating to 240°C. It is
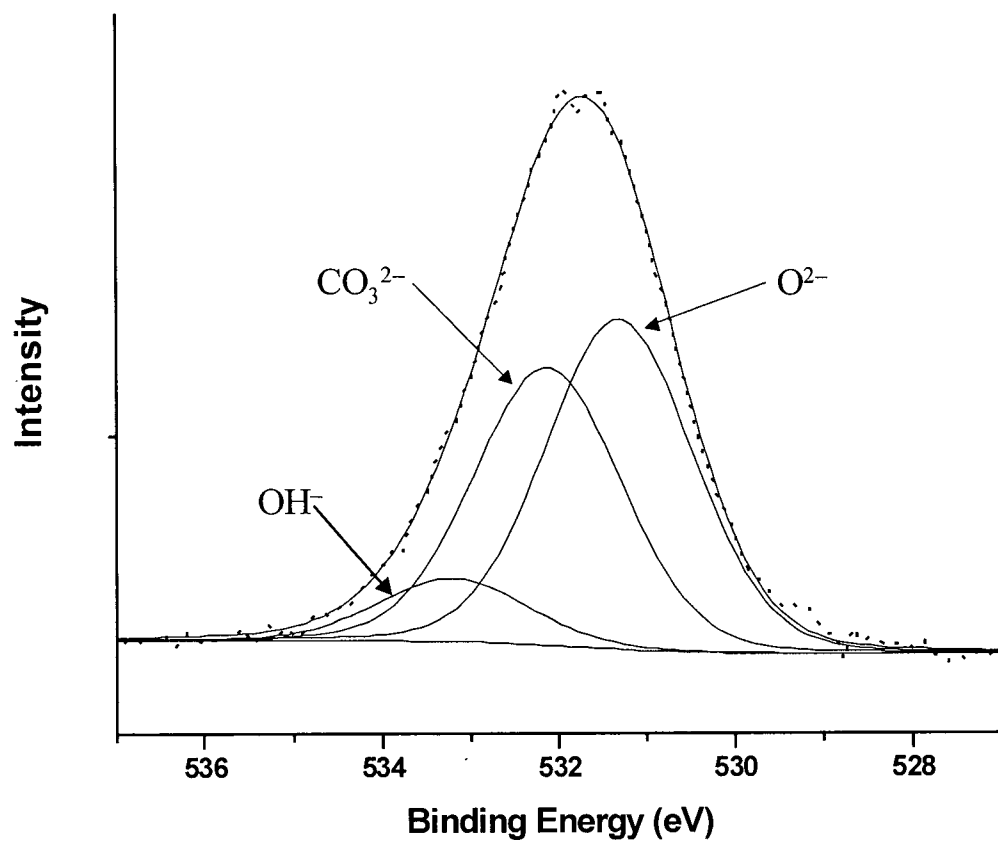
Figure 5.4. An interpretation for the O 1s spectrum measured from a mirror-polished AZ91-Mg alloy at room temperature assuming regular contributions from OH⁻ and O^{2-} and an assumed contribution from CO_3^{2-}.

possible that decomposition products from the hydrocarbon contamination are involved but a more detailed systematic study would be needed to establish exactly how the O 1s spectrum evolves with temperature, including temperatures higher than 240°C. However, there are some practical issues since by 240°C the vapor pressure of Mg is getting high for the UHV chamber [153].

To summarize for this section, the mirror-polished AZ91 surface appears stable on heating in UHV to close to 240°C, when still no Zn is detected, and the surface dominantly involves Mg in its fully oxidized state as carbonate, oxide, and perhaps a decomposition product from hydrocarbon contamination. Little Al is present in the surface region and it is only partially oxidized.

5.3.3 Chemical Analysis of AZ91 Magnesium Alloy

The first chemical analysis of the AZ91 surface was applied to the mirror-polished alloy since this enables the basic microstructure to be imaged with SEM and, furthermore, the mirror-polished surface serves as the starting point for studying silane coatings in the following sections. The low-magnification SEM image of the mirror-polished sample (Figure 5.5(a)) indicates that the surface is relatively smooth, and at higher magnification (Figure 5.5(b)) three types of micro-regions are apparent: (i) grain boundaries (lighter colored), (ii) the matrix, and (iii) particles. The overall bulk composition was characterized by EDX analysis made over a 100 x 100 μm^2 area. Different measurements were made over different regions to ensure a reasonable sampling. The bulk composition reported Mg 90.7%, Al 8.6% with trace amounts of Zn
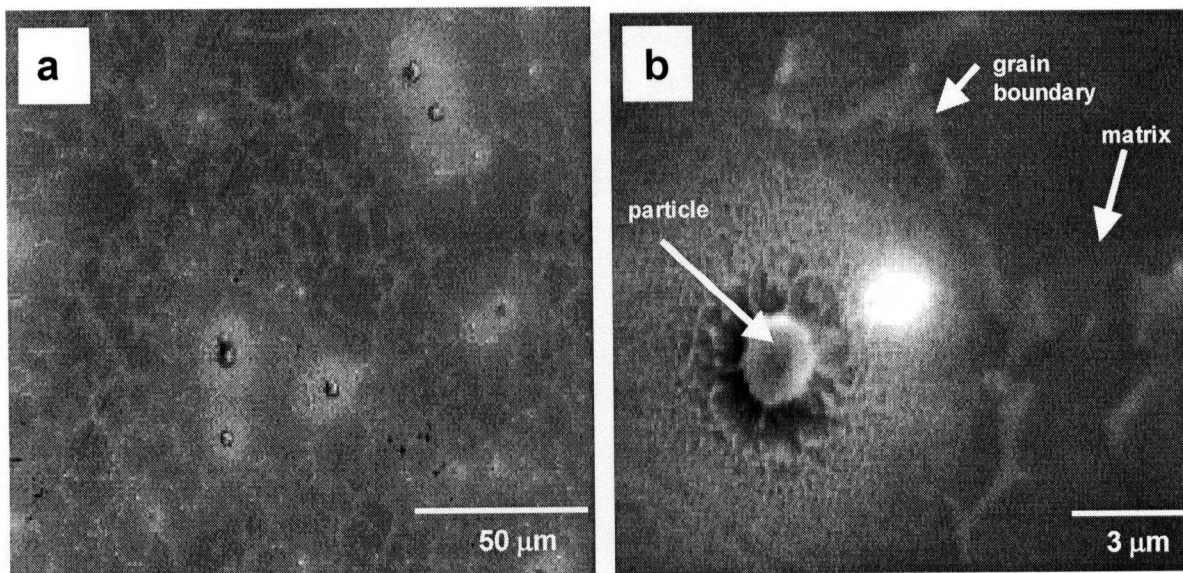
Figure 5.5. SEM micrographs of a mirror-polished surface of AZ91 to show microstructure at different magnifications.

and Mn are close to expectation for a AZ91 alloy (Table 5.3). Zn is a regular additive for

the alloy, while Mn is added to improve corrosion resistance [76].

Table 5.3. Atomic percentage measurements by EDX and XPS for alloying elements in a mirror-polished AZ91 surface.

Element	EDX	XPS
Mg	90.7	95.8
Al	8.6	4.2
Zn	0.4	–
Mn	0.3	–

Independent measurements indicate the uncertainties for Mg and Al are ± 1.0 % for EDX and 0.5 % for XPS.

The probe depth of EDX for Mg using an electron beam of 20 keV energy can be

up to 6 μm [154]. In contrast, XPS is much more surface sensitive, where the probe

depth is less than 10 nm based on the calculation for MgO (electron energy 1435 eV).

Compositions from this surface region, where the analysis area is 4 x 7 mm^2, are

compared with the EDX results in Table 5.3. A clear tendency is apparent for Mg to

show a relative concentration at the surface, with a small amount of Al (4%), while no Zn

or Mn is detected with XPS.

Further analysis of the mirror-polished sample was done to investigate the

different microstructural regions observed on the surface. EDX was first utilized with

measurements over an analysis area 3 x 3 μm^2 to probe bulk compositions below the

different types of micro-region. Results are presented in Table 5.4, where the

measurements are compared with surface measurements made with SAM (over 10 nm

dimension). Values of composition measured by EDX for different regions of the grain-

boundary region vary somewhat from area to area; the values quoted in Table 5.4 are average values with the variation for Mg and Al being at the ±3.0% level. Nevertheless the trend is seen where the grain boundary regions show relatively high Al content in comparison with the matrix region; this has been observed by others, and it has been reported to originate with the presence of $Mg_{17}Al_{12}$ [75, 77]. The values quoted in Table 5.4 for the matrix region are for measurements at central locations where uncertainties in the compositions for Mg and Al are at the ±2.0% level. More variation is indicated for Al in the matrix depending on the proximity to a grain boundary, where the amount of Al can apparently be increased by up to 10%; similar variations have been reported in other studies [16, 75-77]. However, it is not clear whether these variations indicate real changes in local composition on the matrix, or whether the large analysis volume of EDX [154] results in some inclusion of contributions from the grain boundary region, where the Al content is definitely higher.

Table 5.4. Atomic percentage measurements by EDX and SAM for alloying elements in a mirror-polished AZ91 surface.

	Central matrix		Particle		Grain boundary	
	EDX	SAM	EDX	SAM	EDX	SAM
Mg	93.8	88.8	58.6	100.0	79.8	89.3
Al	5.8	11.2	25.5	–	19.5	10.7
Zn	0.3	–	0.2	–	0.6	–
Mn	0.1	–	15.7	–	0.1	–

The atomic percentages from SAM are after removal of signals from surface carbon and oxygen.

Although EDX detects Mg, Al, Zn and Mn contents from all the micro-regions of the polished surface, the contributions from Zn are small everywhere; those for Mn are at the barely detectable level for the grain-boundary and matrix regions, but a significantly higher value is found for the particles (15.7% reported in Table 5.4). This value represents an average over three different particles, where the content of Mn can vary by ±5.0% for individual particles. Mn has a low solubility in Mg [17], and others have noted that a Mn-rich phase can exist in the AZ91 alloy, perhaps in combination with Fe impurity [16, 76, 77]. However, this is the first study where separate Mn-containing particles are seen on the polished surface of AZ91. While the particles quoted in Table 5.4 have bulk compositions Mg 58.6%, Al 25.5% and Mn 15.7%, SAM detects 100% Mg from the surface region. Likewise the grain boundaries show increased Mg and decreased Al at the surface, but this trend is reversed for the central region of the matrix where the Mg content has decreased slightly at the surface, and the Al content increased, compared with the bulk.

Another approach to investigating the compositional structure of the AZ91 alloy was taken by fracturing the sample after immersing in liquid nitrogen, and then studying the surface after rapidly introducing into the vacuum chamber. Figure 5.6(a) gives a view of the sample cross section; this surface is rough and the overall EDX measurement (100 x 100 μm^2 area) gave the chemical compositions Mg 90.2%, Al 7.8%, Zn 1.6% and Mn 0.4%. These values are within the uncertainties for the bulk composition obtained with the mirror-polished sample, although the amount of Zn detected from the cross section is higher than that from the polished sample.
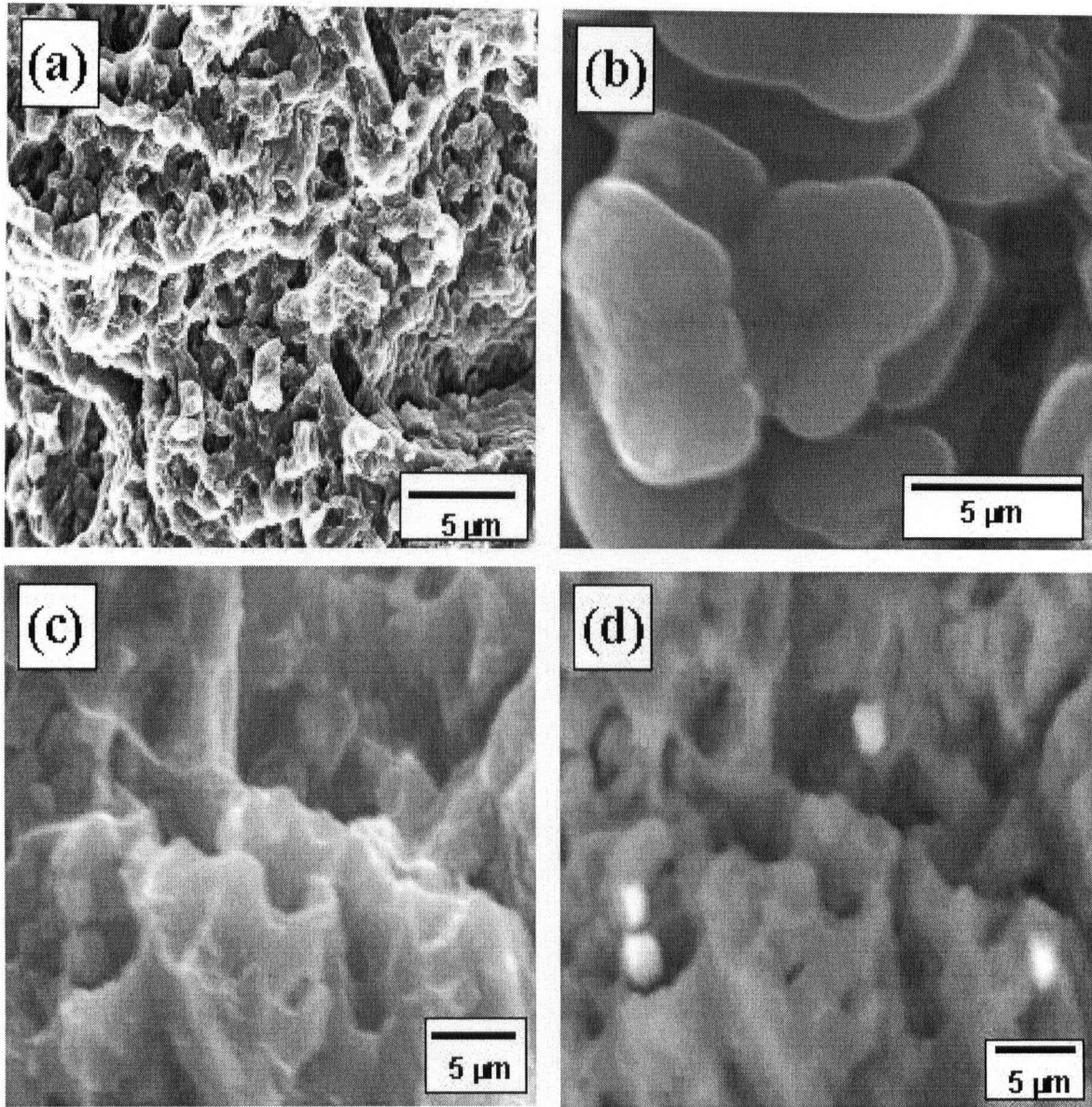
Figure 5.6. SEM images of cross section of AZ91 alloy: (a) overall, at lower magnification, (b) region A, (c) region B, (d) particles in region B seen with backscattered electrons.

An initial view of SEM micrographs from the cross section at higher magnification showed two distinct regions. Region A (Figure 5.6(b)) was distinguished by the presence of ball-like structures which were randomly distributed on the cross section, particularly in the deeper regions. EDX measurement, from a 1 x 1 μm^2 area, for the ball-like structure was impeded a bit by the deeper location, but on average these ball-like structures showed high Zn content (Table 5.5). EDX analysis from region B (Figure 5.6(c)) detected a significant Mn content, but more information was obtained from SEM images using backscattered electrons. An example is shown in Figure 5.6(d), where the atomic number contrast [94] allows the particles to be imaged. EDX from these particles (1 x 1 μm^2 area) showed a high Mn content (Table 5.5) with the atomic composition matching reasonably well with the particles on the polished surface. Further EDX measurements in region B, from the areas that avoided the particles, showed the presence of Mg, Al, and trace amounts of Zn and Mn. Their compositions are included in Table 5.5, where comparisons are made for each region with results from the measurements with SAM.

Table 5.5. Atomic percentage measurements by EDX and SAM for different regions on fractured surface of AZ91.

	Region A		Region B (particle)		Region B (no particle)	
	EDX	SAM	EDX	SAM	EDX	SAM
Mg	95.1	88.4	52.3	100.0	85.6	89.2
Al	3.2	11.6	32.6	–	14.2	10.8
Zn	1.7	–	–	–	0.2	–
Mn	–	–	11.5	–	0.1	–

EDX compositions from the ball-like structures in region A (fractured surface) match well with those from the central matrix region of the polished surface, and a similar relation is apparent between region B (avoiding particle) with the grain boundary on the polished surface. Further, the surface compositions given by SAM correspond closely between the matched regions on the differently prepared surfaces. The amounts of Mg at the different surfaces (100% on particles, ~89% on the regions A, matrix, B (no particle) and grain boundary) possibly suggests the role of alloy formation. Others have associated the grain boundaries with the presence of $Mg_{17}Al_{12}$, and apparently that surface region would have extra Mg in order to get the overall surface composition. The similar surface compositions determined for the A region and the matrix region suggests that a similar model may apply to these surfaces too, even though EDX does show differences for the bulk compositions. The particles are associated with an enhanced amount of Mn. This element has a low solubility in Mg, but it can combine with Al to form Al-Mn intermetallic compounds [17]. At the particle surface, an excess of Mg must apparently cover any intermetallic phases to give the local 100% Mg composition that is observed by SAM.

5.3.4 Coating of Air-oxidized AZ91 Alloy with γ-GPS

The air-oxidized mirror-polished surface of AZ91 alloy was coated with three separate organosilanes (γ-GPS, γ-APS and BTSE) at their natural pH values (10.4, 5.7 and 4.3 respectively) in order to gain initial knowledge for the amounts and robustness of coatings on this surface, and to relate to the underlying alloy composition.

This section describes observations for the coating by 1% γ-GPS solution at pH 5.7. Table 5.6 reports compositions by XPS for the sample as coated, and after the ultrasonic rinsing test, in order to get an initial sense for the strength of the coating adhesion [112]. The small value of the Si/Mg ratio (0.12) prior to the ultrasonic rinse indicates that the coating is thin or non-uniform (that will be investigated with SAM later). The thin coating may be due to the fact that for γ-GPS at its natural pH of 5.7, only the hydrolyzed end (Si-OH) is available for the coating process; the oxirane group is reported to not open until the pH is reduced to 2.15 [57]. Interestingly, prior to rinsing, no Al was detected by XPS from the surface although, after the rinse test, when the amount of Si reduces markedly (to 32% of its initial value), Al is detected (at the 8.5% level) with negligible change in the amount of Mg detected (89.3% reduced to 88.1%). This indicates that the ultrasonic rinse strongly affects the underlying surface.

Table 5.6. Atomic percentage measurements by XPS for an AZ91 surface coated with 1% γ-GPS before and after applying the ultrasonic rinsing test.

	Before	After
Si	10.7	3.4
Al	–	8.5
Mg	89.3	88.1

Figure 5.7(a) and (b) show SEM images of the coated AZ91 surface before and after the rinse test. In the initially coated state the alloy surface shows particles, grain boundaries and matrix regions, as for the mirror-polished uncoated surface. However, after the rinsing test (Figure 5.7(b)) changes are observed, with the grain boundary regions no longer detected and the matrix regions show evidence for etching. These
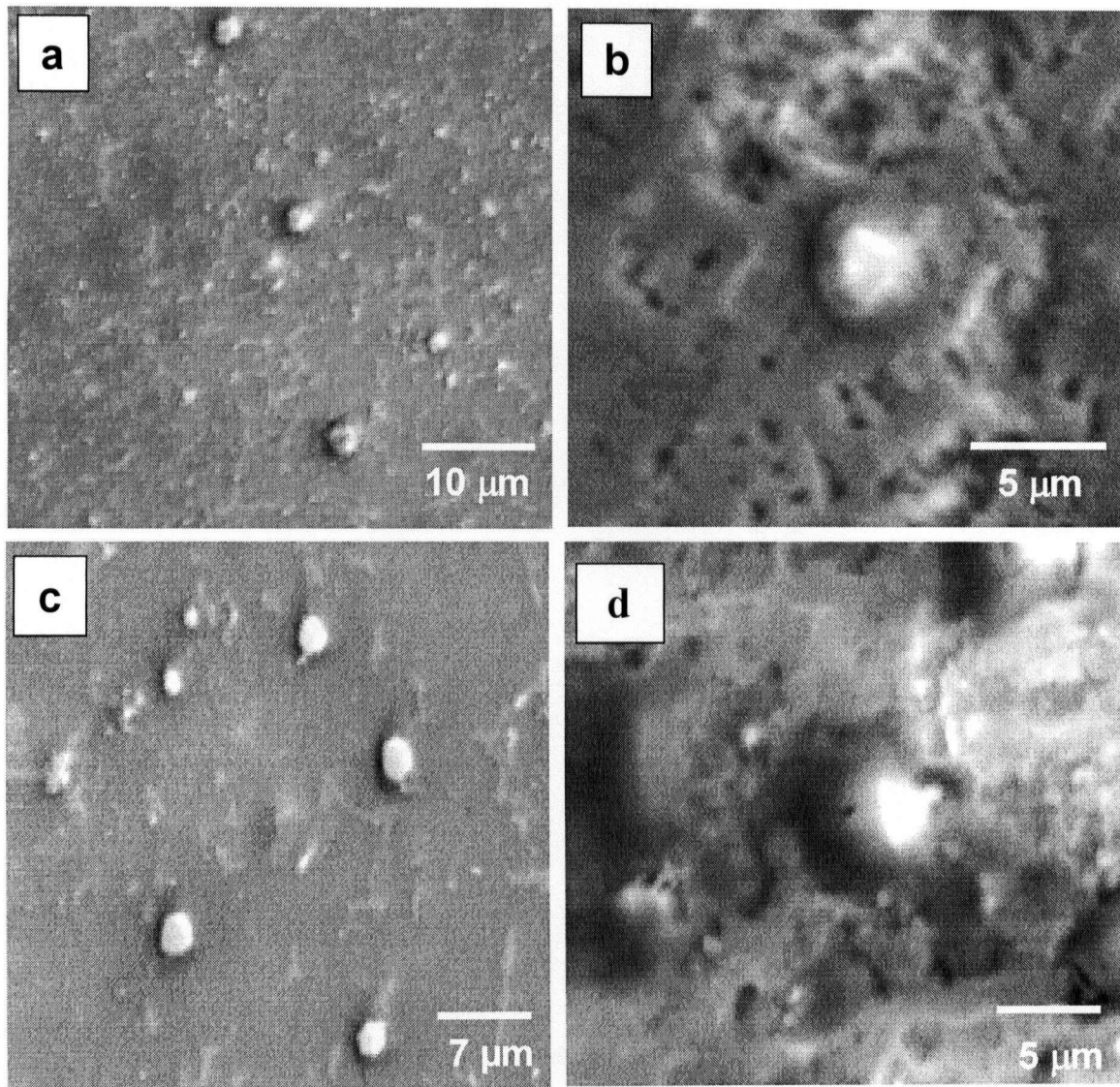
Figure 5.7. SEM micrographs of AZ91 alloy surfaces coated with 1% γ-GPS: (a) prior to and (b) after the ultrasonic rinsing test; and coated with 1% γ-APS: (c) prior to and (d) after the ultrasonic rinsing test.

differences seem to directly involve the rinsing procedure, where some of the loosely-bonded γ-GPS is removed with exposure of the underlying surface to water.

SAM measurements for the γ-GPS-coated surface, reported in Table 5.7, indicated similar amounts of Si for all three regions, and hence it appears that their different chemical compositions did not have a major role in the coating process. After the sonication rinse, no silane was detected from the particle and the remaining adhered silane was restricted to the matrix regions, and even there the total adsorption had been reduced appreciably. Clearly the conditions used for adsorbing the γ-GPS did not lead to a well-adhered coating, and after the rinsing the coating was highly non-uniform. Also charging was apparent after the rinsing test, apparently due to formation of a thicker Mg oxide layer after removal of the silane.

Table 5.7. Atomic percentage measurements by SAM for different regions of a mirror-polished AZ91 surface after coating with 1% γ-GPS.

	Mg	Al	Si
Particle	79.5	–	20.5
Grain boundary	81.6	–	18.4
Matrix	80.4	–	19.6

5.3.5 Coating of Air-oxidized AZ91 Alloy with γ-APS

This section describes observations for the coating of the air-oxidized mirror-polished AZ91 surface by 1% γ-APS solution at pH 10.4. Table 5.8 reports compositions determined by XPS for the γ-APS coated sample and after it had undergone the

sonication test, when the amount of Si showed a drastic change (to 7% of its initial value). The initial amount of Si adsorbed is high, and this may have resulted in part from hydrogen bonding through the organofunctional amine group [36, 55, 56, 58, 142]. Other studies have reported that γ-APS is only loosely bound to metals, such as iron or aluminum, and that it can detach on exposure to water [55, 63]. Although a small amount of Si is still present after the rinse (Table 5.8), the relative proportions of Al and Mg become very similar to the values holding for the mirror-polished sample, on regions except for the particle (i.e. close to 89% Mg). The SEM image of the γ-APS coated surface of AZ91 in Figure 5.7(c) shows the particle, grain boundary and matrix regions, but changes are observed after the rinse test (Figure 5.7(d)) when the grain boundary region is no longer clear. This is consistent with both loss of the silane and change to the substrate as a result of attack by water, and hence reinforces the observations from XPS.

Table 5.8. Atomic percentage measurements by XPS for an AZ91 surface coated with 1% γ-APS before and after applying the ultrasonic rinsing test.

	Before	After
Si	80.4	5.5
Al	–	8.8
Mg	19.6	85.7

Measurements by SAM for the γ-APS coated surface showed that the amount of Si detected in relation to Mg varied from site to site (for some areas both Mg and Si were detected whereas elsewhere only Si was seen). It has been reported that a γ-APS coating

on iron may be porous [36], and similar behavior for adsorption on AZ91 may allow more Mg to be detected from some regions. After the rinsing test, SAM failed to detect Si from any region tested, but the spectra are somewhat noisy due to surface charging. Although some charging was apparent from thicker silane coatings prior to the rinsing, charging was more serious after this test. That apparently followed from increased oxidation of the substrate after the loosely-attached silane was removed.

5.3.6 Coating of Air-oxidized AZ91 Mg Alloy with BTSE

This section deals with coating by BTSE which has the maximum number of Si-OH groups after hydrolysis, but it lacks other functional groups. Figure 5.8(a) shows a SEM image of the surface that had been coated with 1% BTSE (pH 4.3), and which still allows identification of the three micro-regions that were seen for the uncoated surface. However, some grain-boundary regions, which originally appeared lighter-colored, now appear dark. This is possibly a result of galvanic coupling between the grain boundary and the surrounding regions, where at pH 4.3, etching around the grain boundary occurs with some undercutting of it from the alloy surface [76].

SAM measurements detected the presence of Si on all three micro-regions, and the relative amounts of Mg, Al and Si are reported in Table 5.9. The amounts of Si on the different regions are similar, and the same statement can be made for the amounts of Al detected relative to Mg. The relative amounts of Al and Mg from the three regions indicate that during the coating process Mg dissolution occurs with exposure of Al compared to the situation for the uncoated surface. Apparently for the BTSE coating process, the chemical differences detected by SAM for the three regions prior to coating
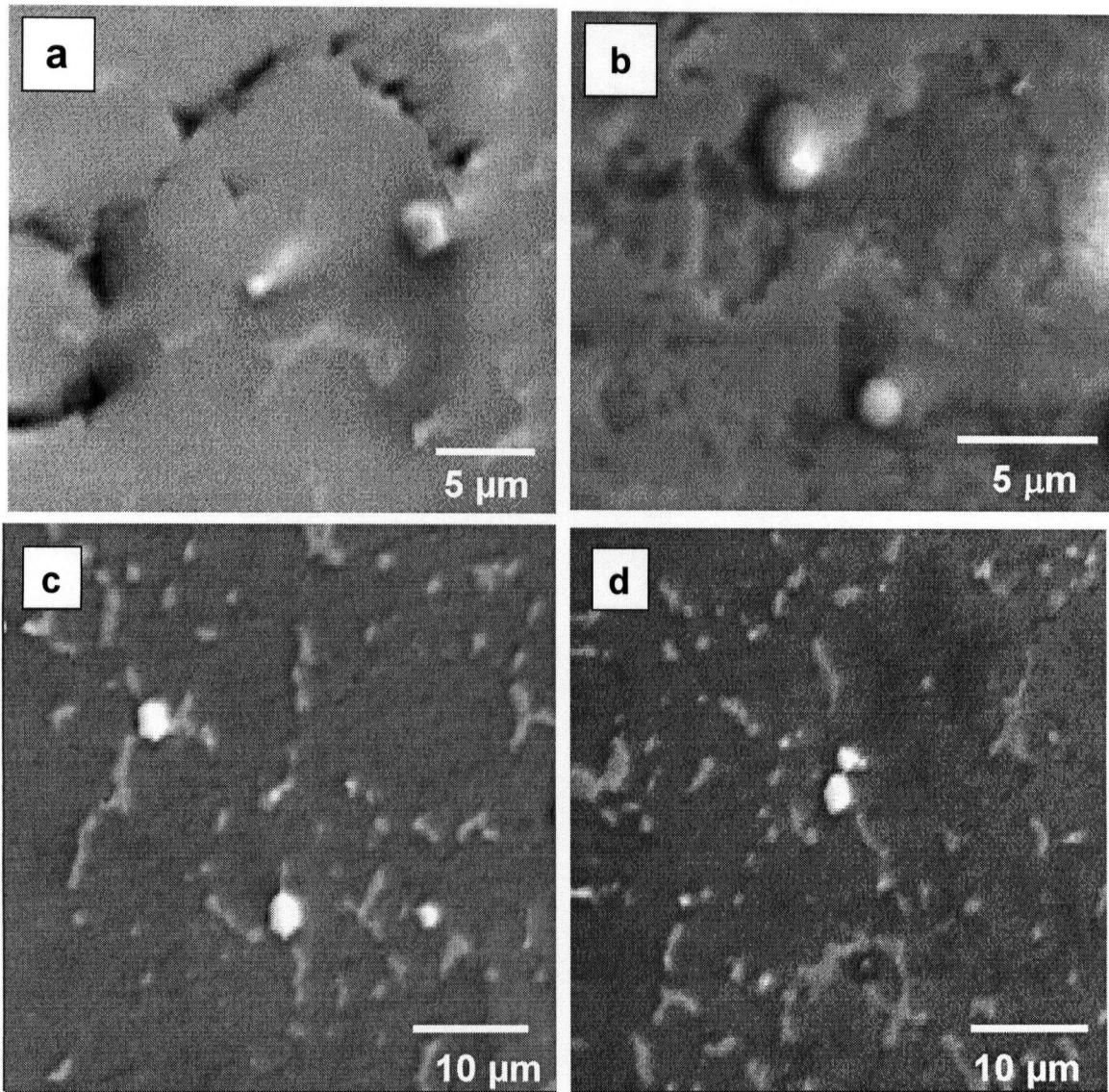
Figure 5.8. SEM micrographs of AZ91 alloy surfaces coated with 1% BTSE: (a) prior to and (b) after the ultrasonic rinsing test; with 4% BTSE: (c) prior to and (d) after the ultrasonic rinsing test.

did not significantly affect the coating outcome, which gave a basically uniform BTSE coating.

Table 5.9. Atomic percentage measurements by SAM for different regions of a mirror-polished AZ91 surface after coating with 1% BTSE.

Before rinsing				
Region	Mg	Al	Si	Al/Mg
Particle	68.0	6.5	25.6	0.10
Grain boundary	67.2	8.1	24.7	0.12
Matrix	67.6	7.8	24.7	0.12

After rinsing				
Region	Mg	Al	Si	Al/Mg
Particle	63.9	19.6	16.5	0.31
Matrix	63.3	19.5	17.2	0.31

To assess the adhesive strength of the BTSE coating, the coated sample underwent the ultrasonic rinsing test in water. Table 5.10 reports XPS measurements before and after this test. The overall Si content is reduced to 36% of its original value, which indicates poor adhesion. But it is clear that the underlying surface is also affected; the Al/Mg ratio changes from 0.06 before the rinse to 0.16 after the rinse. Figure 5.8(b) shows a SEM image from the surface after the ultrasonication test and, consistently with observations by XPS, the surface appearance has changed from that prior to the rinsing.

Table 5.10. Atomic percentage measurements by XPS for an AZ91 surface coated with 1% and 4% BTSE before and after applying the ultrasonic rinsing test.

	Before rinsing			After rinsing		
	Si	Al	Mg	Si	Al	Mg
1%	21.6	4.2	74.1	7.7	12.6	79.6
4%	63.8	–	36.2	62.8	–	37.2

The particles are still identified in Figure 5.8(b), but the grain-boundary regions are no longer seen; as well the matrix region appears to have undergone etching. The particles in Figure 5.8(b) are more round and defined compared with those in Figure 5.8(a). The rinsing appears to have led to etching around the particles, possibly connected with the underlying Mn content. Others have noted that these particles are cathodic compared to the matrix and so can cause the surrounding matrix to undergo anodic dissolution [76, 77]. The grain-boundary regions may no longer be visible because the rinsing process may have detached weakly-bound fragments in their vicinity. Table 5.9 reports SAM measurements for the particle and matrix regions after the rinsing, and it is seen that Si is detected from both regions in similar amounts, although both are reduced compared with prior to the rinsing. Also, after the rinse test, the Al/Mg ratio have similar values for both regions, with values that are increased compared with before the test. Apparently fragments of the underlying substrate, as well as BTSE, have detached during the water rinse to expose Al.

Since BTSE provides the most positive coating among the organosilanes tested at their natural pH values, initial investigations were made for use of a higher concentration for the BTSE coating solution, specifically at 4%. Figure 5.8(c) shows SEM images

measured after this coating, where the three micro-regions remain clearly defined, and after the ultrasonic rinse test (Figure 5.8(d)), where no significant changes are seen from before the test (Figure 5.8(c)). This is supported by XPS measurements, where the relative compositions detected before the rinse test, Si (63.8 %) and Mg (36.2 %), remain constant to within 1.0 % of the values measured after the rinse test (Table 5.10). Also no Al is detected by XPS after the rinsing. This constancy of composition before and after the sonication process strongly suggests that a denser BTSE film, compared with use of the 1% BTSE coating solution, has been able to retard water penetration thereby preventing attack of the underlying Mg oxide surface.

5.4. Concluding Remarks

The first part of this project used XPS to investigate oxide growth on the cleaned AZ91 surface, and the evidence indicated that Mg was preferentially oxidized while leaving the Al component relatively unchanged, an observation consistent with Mg being more easily oxidized than Al. The attenuation of the Al 2p signal with increasing oxidation suggests that the Mg oxide growth occurs over the Al, thereby helping to protect it. Mg oxide formed from oxygen dosed at atmospheric pressure showed similar amounts of oxide and hydroxide in the Mg 2p spectrum. The alloying elements (other than Al) in the AZ91 sample do not seem to have any noticeable effect on the nature and behavior of the native oxide layer, whose nature seems similar to that on pure Mg. Heating the mirror-polished AZ91 sample in UHV showed that the surface oxide and carbonate are stable to close to 240°C.

The mirror-polished AZ91 sample showed the presence of Mg and Al in the surface region according to XPS and SAM, whereas EDX analysis of the bulk indicated the additional presence of Mn and Zn. SEM identified three types of micro-regions on the polished surface, namely the particle, grain boundary, and the matrix, and microanalysis showed different surface and bulk compositions associated with these regions. Significant Mn content was detected only for the particles, which was believed to depend on a Al-Mn alloy phase, and the grain-boundary region showed relatively high Al content compared to the matrix. The fractured surface was different topographically, but chemical compositions for the different regions correlated well with regions seen on the mirror-polished surface. Thus while the polishing process gave a smoother surface, which was advantageous for direct identification of the different regions, there is no evidence that process distorts to any great extent the chemical composition compared with an intrinsic surface.

Preliminary investigation into the extent to which three organosilanes (BTSE, γ-GPS and γ-APS) at their natural pH values could coat the AZ91 alloy surface showed generally poor stability in terms of the ultrasonic rinsing test. The decreases in Si content after the rinsing test were greater than for 7075-Al, when coated with BTSE and γ-GPS at their natural pH values, so emphasizing that the AZ91 alloy surface provides a greater challenge for coating. As an organosilane coating is removed from AZ91, it seems that exposure of the substrate to water leads to more oxidation and an intrinsically less stable surface in many environments. Neither of the two organofunctional silanes mentioned (γ-GPS and γ-APS), for the natural pH values used, showed benefit for coating the AZ91 surface. On the other hand, 1% BTSE showed coating adhering to the micro-regions

after the sonication test, although the rinsing did lead to a net decrease in the amount of adsorbed Si. This appears to depend partly on the structure of BTSE, with its potential for six silanol groups per molecule, which in principle can optimize the bonding. Also the natural pH of 4.3 is likely to be favorable for the initial etching, which allows Al to be detected. Initial work with a 4% solution of BTSE showed a greatly increased protection for the AZ91 surface; apparently the higher concentration gave both a thicker and denser coating compared with 1% BTSE. The denser coating is particularly important to avoid attack through local porous regions.

Chapter 6   Concluding Remarks

6.1 New Results

The first objective of the work presented in this thesis was to increase knowledge, at the microscopic (molecular) level, for BTSE coating on different Al surfaces, particularly on how the actual nature of the starting oxidized Al surfaces can lead to different outcomes. These BTSE coating are affected by both the Al-O-Si chemisorption bonding at the interface as well as by the morphology of the starting surface. The Forest Product Laboratory (FPL) treatment applied for 15 min to native oxide on a high-purity Al sample was shown by quadrupole SIMS to be effective for maximizing the chemisorption bonding, and SEM showed that this pre-treatment also gave a surface morphology (scallop-like structure) that appeared to lead to a strengthened BTSE coating. This treatment time was consistent with the conventional recipe that the FPL pre-treatment should be carried out for 15-30 min, a recommendation that comes almost entirely from performance in macroscopic tests. But this work for the anodized 7075-Al sample, whose surface had a different nature to the native oxide on high-purity Al, showed that the FPL treatment for 5 min was sufficient to maximize the BTSE adsorption, according to XPS and the ultrasonic rinsing test, when time of FPL treatment was the sole variable. However, it turned out that the amount of Al-O-Si interfacial bonding could be increased further by extending the pre-treatment to include exposure to a hydrogen plasma.

This work reinforced ideas that the coating process in the BTSE solution is dynamic with simultaneous etching, protonation and coupling to form the Al-O-Si

interfacial bonding, and condensation for BTSE polymerization. The Al-O-Si bonding should be increased when OH formation and coupling dominates over etching, but the presence of surface OH comes both from the pre-treatment and from protonation of oxide during the coating process. Competition of the coupling reaction with the BTSE polymerization was observed for the 7075-Al case. SIMS indicated an increase in the Al-O-Si interfacial bonding when that sample was further pre-treated with the hydrogen plasma, but the total bonded silane (Al/Si ratio of 1.1 detected by XPS) decreased compared with the sample that just received the FPL pre-treatment (that sample had a sufficiently thick coating that no Al signal could be detected). The thinner coating for the sample that had the hydrogen plasma treatment resulted from less Si-OH groups available for self BTSE polymerization, since more Si-OH groups reacted with Al-OH groups after the plasma treatment.

Other experiments were designed to build understanding for the way the organosilane coatings varied with the different microstructural regions of the alloy, specifically including the second-phase particles (of Al-Cu-Mg (round) and Al-Fe-Zn (irregular) types), and the matrix regions (dominantly composed of Al), after different pre-treatments were applied. SAM gives a powerful characterization for this purpose. For example, it was shown that air exposure of the 7075-Al sample at room temperature resulted in oxidation of all the micro-regions, with change in the relative proportions for the metallic elements. The trend established by this work is that the more easily oxidized element (Mg on round particle, Al on irregular particle) concentrate at the surface of the second-phase particle, with the oxide formed acting to protect the other elements below.

BTSE at its natural pH (4.3) was able to coat all micro-regions of the 7075-Al alloy after air oxidation (~20 h), although differences were observed for the round particles where Mg was etched away during the coating process. With γ-GPS (pH 5.7), for the air oxidized 7075-Al surface, coating was limited to discrete nodules from silane polymerization. It was concluded that the pH did not give a favorable balance for the hydrolysis of γ-GPS, etching of oxide, and protonation of the surface to give Al-OH groups. At pH 4.5, coating was observed for the matrix and the irregular particle regions, but not on the round particles, where the etching reaction of Mg apparently dominated over both protonation of the alloy oxide and the coupling reaction of Al-OH and Si-OH. A complete coating was achieved by lowering the pH to 3.2, where it was suggested that enough H^+ ions were present for etching the Mg from the round particles and protonating the oxide to give -OH for coupling with the Si-OH. Although not developed, these observations gave clues that selective coating may be feasible, where different silanes are adsorbed at different regions according to the pH used in each case.

A new observation was that a complete coating could be achieved with γ-GPS at its natural pH (5.7) by heating the 7075-Al surface to 200°C for 15 min prior to coating. The heating pre-treatment led to an increase in oxide at all micro-regions, with significant segregation of alloying elements, and especially for Mg, whose oxide can be protonated at higher pH compared with Al [17]. The heating also gave an increase in roughness, and both effects enhanced the silane adsorption compared with the air-exposed mirror-polished sample.

TOF-SIMS measurements probed interfacial bonding within the three samples of 7075-Al for which SAM showed silane adsorption on all micro-regions: (i) coated with

BTSE (pH 4.3), (ii) coated with γ-GPS (pH 3.2), and (iii) heated prior to coating with γ-GPS (pH 5.7). For the air-oxidized sample that had been coated by BTSE at pH 4.3, covalent Al-O-Si bonding was present on all three micro-regions, with a small contribution of Fe-O-Si bonding to the irregular-particle region. MgOSi$^+$ fragments were not detected from the round particle, presumably because during the coating process etching of Mg dominated over the coupling of Mg-OH with Si-OH. The absence of CuOSi$^+$ fragments likely resulted from the overlayer of Al oxide protecting Cu from being directly exposed to the coating solution. For the air-oxidized sample coated with γ-GPS at pH 3.2, only AlOSi$^+$ fragments were detected from all micro-regions, due to the low pH of the coating solution. For the heat pre-treated sample coated with γ-GPS at the natural pH (5.7), it was seen that segregation of Mg on the surface played a role in forming the interfacial Mg-O-Si covalent bonds that (along with Al-O-Si bonds) were detected from all micro-regions.

Surface analysis investigations of the mirror-polished AZ91-Mg alloy prior to coating showed that the surface was composed of Mg in its fully oxidized state (with the presence of oxide and carbonate) and that this surface was stable to close to 240°C. SEM identified three types of micro-regions on the surface of this alloy which were referred to as the grain boundary, matrix, and the particle regions. XPS and SAM measurements showed that Mg and Al were always in the surface region (but the Al/Mg ratio was below expectation for the bulk composition), whereas bulk analysis with EDX was necessary to identify the additional elements, Mn and Zn. The analysis of the particle showed significant Mn content and this gave support for the presence of an Al-Mn alloy phase. Additional analysis of the AZ91 alloy after fracturing indicated surface compositions for

different regions that correlated well with compositions for regions seen on the mirror-polished sample.

Investigation into the extent to which three organosilanes (BTSE (pH 4.3), γ-GPS (pH 5.7), and γ-APS (pH 10.4)) at their natural pH values could coat the AZ91 alloy surface showed generally poor stability in terms of the ultrasonic rinsing test, where the decreases in Si content after rinsing were much greater than what was found for 7075-Al (when that alloy was coated with BTSE and γ-GPS at their natural pH values). This result for AZ91 was attributed to the unstable Mg oxide substrate that gets exposed to water during the rinsing test. Neither of the two organofunctional silanes mentioned (γ-GPS and γ-APS) showed benefit for coating whereas BTSE offered more promise, in part because of its greater number of silanol groups available for the coupling process as well as polymerization. Increase in the concentration of the BTSE solution to 4% gave both a thicker and denser coating when compared with the solution at 1% concentration. The total amount of Si adsorbed for the 4% BTSE was three times greater than that for the 1% case. In addition, at the higher concentration, the silane layer was more firmly attached according to the ultrasonic rinse test (where the Si content decreased by only 1% after the rinsing).

6.2 Future Directions

This work has contributed new knowledge for the varying chemistries occurring at different microstructural regions of alloys surfaces. Knowledge from SAM is still very limited in this area, and TOF-SIMS was applied for the first time. The combination of SAM and TOF-SIMS is likely to be extremely useful in the future for studying

organosilane adsorption and bonding on different regions of the various Mg and Al alloys, particularly as a function of different pre-treatments. As well, more research should be carried out for the organosilane adsorption on pure Mg in order to strengthen understanding for the coating on the Mg alloy systems. The ultimate aim will be to find measures for saturation coverages and to test for stability in corrosive environments (e.g. by electrochemical polarization tests).

For both the 7075-Al and AZ91-Mg alloys, BTSE showed the most promise for achieving a complete coating on the different micro-regions at the natural pH. For practical use, so that a silane coated surface can be painted, an uppermost organofunctional coating would be needed. Thus to develop BTSE coatings further, a two step coating process [36] would be required wherein the BTSE coating is applied first to the substrate followed by an organofunctional silane. Throughout, work on organosilane coatings for the light metal alloys must be compared against the corrosion protection that can be obtained by conversion coatings such as for chromating and phosphating.

References

1. D.G. Altenpohl, Aluminum: Technology, Applications, and Environment, A Profile of A Modern Metal, 6th ed., The Minerals, Metals & materials Society (TMS), Pennyslvania, 1998.

2. J.R. Davis, Corrosion of Aluminum and Aluminum Alloys, ASM International, Materials Park, OH, 1999.

3. J.R. Davis, Ed., Aluminum and Aluminum Alloys, ASM International, Materials Park, OH, 1993.

4. L.F. Mondolfo, Aluminum Alloys: Structure and Properties, Butterworth, London, 1976.

5. F. Andreatta, H . Terryn, J.H.W. de Wit, Corros. Sci. 45 (2003) 1733.

6. P. Leblanc, G.S. Frankel, J. Electrochem. Soc. 149 (2002) B239.

7. D. Zhu, W.J. van Ooij, Corros. Sci. 45 (2003) 2163.

8. T. Suter, R. C. Alkire, J. Electrochem. Soc. 148 (2001) B36.

9. G. Mrówka-Nowotnik, J. Sieniawski, J. Mater. Process. Technol. 162 (2005) 367.

10. N. Birbilis, R.G. Buchheit, J. Electrochem. Soc. 152 (2005) B140.

11. W.G. Callister, Jr. Materials Science and Engineering: An Introduction, 5th ed., John Wiley & Sons, Inc. New York, 2000.

12. ASM Handbook Online: http://products.asminternational.org/hbk/index.jsp.

13. Y.Y. Li, W.W. Zhang, J. Fei, D.T. Zhang, W. P Chen, Mater. Sci. Eng. A 391 (2005) 124.

14. P. Cavaliere, E. Cerri, P. Leo, Mater. Charact. 55 (2005) 35.

15. W.J. D. Shaw, M.A. Fraser, T.S. Nijjar, Microstr. Sci. 26 (1998) 269.

16. G. Ballerini, U. Bardi, R. Bignucolo, G. Ceraolo, Corros. Sci. 47 (2005) 2173.

17. M.M. Avedesian, H. Baker, Ed., Magnesium and Magnesium Alloys, ASM International, Materials Park, OH, 1999.

18. L.M. Pidgeon, Encyclopedia of Materials Science & Engineering, Vol. 4, Pergamon Press, 1986.

19. I.J. Polmear, Light Alloys, Metallurgy of the Light Metals, 3rd ed., Hodder Headline PLC, London, 1995.

20. Chinese Mechanical Engineering Academy, Foundry Manual, Vol. 3, Engineering Industry Press, Beijing, 1993.

21. M. Pourbaix, Atlas of Electrochemical Equilibria in Aqueous Solutions, NACE, Houston, 1974.

22. M.S. Hunter, P. Fowle, J. Electrochem. Soc. 103 (1956) 482.

23. J.S. Solomon, D.E. Hanlin, Appl. Surf. Sci. 4 (1980) 307.

24. W. McGarel, H.A. Farnham, R. McGuckin, Int. J. Adhes. Adhes. 6 (1986) 89.

25. G.D. Davis, T.S. Sun, J.S. Ahearn, J.D. Venables, J. Mater. Sci. 17 (1982) 1807.

26. G.D. Davis, J.D. Venables, in: A.J. Kinloch, Ed., Durability of Structural Adhesives, Applied Science, London, 1983, p. 43.

27. A. Froats, T.K. Aune, D. Hawke, W. Unsworth, J. Hillis, in Metals Handbook, 9th ed., Vol. 13, ASM International, Metals Park, OH, 1987, p.740.

28. W.P. Innes, in: Electroplating and Electroless Plating on Magnesium and Magnesium Alloys, Modern Electroplating, Wiley-Interscience, New York, 1974, Chapter 25, p. 601.

29. J.B. Hajdu, E.F. Yarkosky, P.A. Cacciatore, M.H. Suplicki, Electroless Nickel Processes for Memory Disks, Symposium of Magnetic Materials, Processes and Devices 90 (1990) 685.

30. A.K. Sharma, R. Uma Rani, K. Giri, Metal Finishing 95 (1997) 43.

31. C.E. Habermen, D.S. Garrett, Anticorrosive Coated Rectifier Metals and their Alloys, US Patent 4668347 (1987).

32. X. Sun, R. Li, K.C. Wong, K.A.R. Mitchell, T. Foster, J. Mater. Sci. 36 (2001) 3215.

33. P. Campestrini, H. Terryn, J. Vereecken, J.H.W. de Wit, J. Electrochem. Soc. 151 (2004) B359.

34. Agency for Toxic Substances, US Public Health Service, Toxological Profile for Chromium, Report No. ATSDR/TP-88/10, July 1989.

35. T.F. Child, W.J. van Ooij, Trans. IMF 77 (1999) 64.

36. W.J. van Ooij, T.F. Child, Chem. Tech. 28 (1998) 26.

37. V. Subramanian, W.J. van Ooij, Surf. Eng. 15 (1999) 168.

38. E.P. Plueddemann, Silane Coupling Agents, Plenum Press, New York, 1991.

39. P.E. Cassidy, B.J. Yager, J. Macromol. Sci. D1 (1) (1971) 1.

40. I. Pires, L. Quintino, C.M. Rangel, G.E. Thompson, P. Skeldon, X. Zhou, Trans. IMF 5 (2000) 78.

41. R.P. Digby, D.E. Packham, Int. J. Adhes. Adhes. 15 (1995) 61.

42. L. Kozma, I. Olefjord, Mater. Sci. Technol. 3 (1987) 860.

43. B.A. Waldman, Modern Paint and Coatings, February, 1996.

44. A. Franquet, C. Le Pen, H. Terryn, J. Vereecken, Electrochim. Acta 48 (2003) 1245.

45. W.J. van Ooij, D. Zhu, Corros. 57 (2001) 413.

46. A.M. Beccaria, L. Chiaruttini, Corros. Sci. 41 (1999) 885.

47. Z. Pu, W.J. van Ooij, J.E. Mark, J. Adhes. Sci. Technol. 11 (1997) 29.

48. V. Subramanian, W.J. van Ooij, Corros. 54 (1998) 204.

49. A.M Beccaria, C. Bertolotto, Electrochim. Acta 42 (1997) 1361.

50. R. Tremont, H. De Jesus-Cardona, J. Garcia-Orozco, R.J. Castro, C.R. Cabrera, J. Appl. Electrochem. 30 (2000) 737.

51. T. Van Schaftinghen, C. Le Pen, H. Terryn, F. Hörzenberger, Electrochim. Acta 49 (2004) 2997.

52. D. Shriver, P. Atkins, Inorganic Chemistry, 3rd ed., W.H. Freeman and Company, New York, 1999.

53. D. Zhu, W.J. van Ooij, Corros. Sci. 45 (2003) 2177.

54. W.J. van Ooij, C. Zhang, J.Q. Zhang, W.Yuan, Electrochemical Society Proceedings, 97 (1998) 222.

55. W.Yuan, W.J. van Ooij, J. Colloid Interface Sci. 185 (1997) 197.

56. Y.L. Leung, Y.P Yang, P.C. Wong, K.A.R. Mitchell, T. Foster, J. Mater. Sci. Lett. 12 (1993) 884.

57. E.R. Pohl, F.D. Osterholtz, in: Molecular Characterization of Composite Interfaces, Ed. H. Ishida,G. Kumar, Plenum Press, New York, 1985, p.157.

58. J.S. Quinton, P.C. Dastoor, Surf. Interface Anal. 30 (2000) 21.

59. L. J. Matienzo, D.K. Shaffer, W.C. Moshier, G.D. Davis, J. Mater. Sci. 21 (1986) 1601.

60. P. Poole, J.F. Watts, Int. J. Adhes. Adhes. 5 (1985) 33.

61. O.D. Hennemann, W. Brockmann, J. Adhes. 12 (1981) 297.

62. P.R. Underhill, G. Goring, D.L. DuQuesney, Int. J. Adhes.Adhes. 18 (1998) 307.

63. W.J. van Ooij, D.Q. Zhu, G. Prasad, S. Jayaseelan, Y. Fu, N Teredesai, Surf. Eng. 16 (2000) 386.

64. B.B. Johnsen, K. Olafsen, A. Stori, Int. J. Adhes. Adhes. 23 (2003) 155.

65. J. Fang, B.J. Flinn, Y.L. Leung, P.C. Wong, K.A.R. Mitchell, J. Mater. Sci. Lett. 16 (1997) 1675.

66. M.L. Abel, J.F. Watts, R.P. Digby, J. Adhes. 80 (2004) 291.

67. U. Bexell, M. Olsson, Surf. Interface Anal. 31 (2001) 223.

68. F.J. Boerio, C.A. Gosselin, Adv. Chem. Ser. 203 (1983) 541.

69. F.J. Boerio, C.A. Gosselin, R.G. Dillingham, H.W. Liu, J. Adhes. 13 (1981) 159.

70. J.D. Miller, H. Ishida, Vol.1 of the Proceedings of the Silanes, Surfaces and Interfaces Symposium, D.E. Leyden, Ed. Snowmass, Colorado, June 1985, Gordon and Breach Science Publishers, London, 1985.

71. Y.L. Leung, M.Y. Zhou, P.C. Wong, K.A.R. Mitchell, T. Foster, Appl. Surf. Sci. 59 (1992) 23.

72. F. Zucchi, V. Grassi, A. Frignani, C. Monticelli, G. Trabanelli, Surf. Coat. Technol. 200 (2006) 4136.

73. M. Kono, X. Sun, R. Li, K.C. Wong, K.A.R. Mitchell, T. Foster, Surf. Rev. Lett. 8 (2001) 43.

74. D. Susac, X. Sun, K.A.R. Mitchell, Appl. Surf. Sci. 207 (2003) 40.

75. G. Song, A. Atrens, X. Wu, B. Zhang, Corros. Sci. 40 (1998) 1769.

76. O. Lunder, T. Kr. Aune, K. Nisancioglu, Corros. 43 (1987) 291.

77. O. Lunder, J.E. Lein, T.Kr. Aune, K. Nisancioglu, Corros. 45 (1989) 741.

78. D.Briggs, M.P. Seah, Ed., Practical Surface Analysis; John Wiley & Sons Ltd., West Sussex, 1990.

79. J.C. Vickerman, Surface Analysis; The Principal Techniques, John Wiley & Sons, West Sussex, 1997.

80. D. Briggs, J.T. Grant, Ed. Surface Analysis by Auger and X-ray Photoelectron Spectroscopy, IM Publications, Chichester, 2003.

81. G.A. Somorjai, Introduction to Surface Chemistry and Catalysis, John Wiley & Sons, Inc. 1994.

82. M.P. Seah, W.A. Dench, Surf. Interface Anal. 1 (1979) 2.

83. J.F. Moulder, W.F. Stickle, P.E. Sobol, K.D. Bomben, Handbook of X-ray Photoelectron Spectroscopy, Physical Electronics, Inc. Minnesota. 1995.

84. D.A. McQuarrie, Quantum Chemistry, University Science Books, Sausalito, 1983.

85. D.A. Shirley, Phys. Rev. B 5 (1972) 4709.

86. MAX200 Manual, Leybold, Koln, Germany, 1990.

87. J.C. Riviere, S. Myhra, Ed., Handbook of Surface and Interface Analysis, Marcel Dekker, Inc., New York, 1998.

88. C.R. Brundle, M.W. Roberts, Proc. R. Soc. A331 (1972) 383.

89. L.C. Feldman, J.W. Mayer, Fundamentals of Surface and Thin Film Analysis, Elsevier Science Publishing Co., Inc., New York, 1986.

90.　　Thermo VG Scientific, Microlab 350 Operating Manual, West Sussex, 2002.

91.　　L. Reimer, Scanning Electron Microscopy; Physics of Image Formation and Microanalysis, Springer-Verlag, Berlin, 1985.

92.　　B.L. Gabriel, SEM: A User's Manual for Materials Science, American Society for Metals, Metals Park, 1985.

93.　　J.C. Russ, Fundamentals of Energy Dispersive X-ray Analysis, Butterworths Ltd., 1984.

94.　　J. J. Bozzola, L.D. Russell, Electron Microscopy: Principles and Techniques for Biologist, 2nd ed., Jones & Bartlett Publishers, Sudbury, 1998.

95.　　D.B. Williams, Practical Analytical Electron Microscopy in Materials Science, Electron Optics Publishing Group, Deerfield Beach, Florida, 1984.

96.　　www.moxtek.com

97.　　P. Sigmund, Phys. Rev. 184 (1969) 383.

98.　　J.C. Vickerman, D. Briggs, Ed., TOF-SIMS – Surface Analysis by Mass Spectrometry, IM Publications, Chichester, 2001.

99.　　A.W. Czanderna, D.M. Hercules, Ion Spectroscopies for Surface Analysis, Plenum Press, New York, 1991.

100.　D. Briggs, M.P. Seah, Ed., Practical Surface Analysis, Vol. 2, Ion and Neutral Spectroscopy, John Wiley & Sons, Chichester, 1992.

101.　J.C. Vickerman, A. Brown, N.M. Reed, Secondary Ion Mass Spectrometry, Principles and Applications, Claredon Press, Oxford, 1989.

102.　R.G. Wilson, F.A. Stevie, C.W. Magee, Secondary Ion Mass Spectrometry; A Practical Handbook for Depth Profiling and Bulk Impurity Analysis, John Wiley & Sons, Inc., 1989.

103.　A. Benninghoven, Surf. Sci. 53 (1975) 596.

104.　A. Benninghoven, F.G. Rudenauer, H.W. Werner, Secondary Ion Mass Spectrometry, John Wiley & Sons, New York, 1987.

105.　VG Scientific DP5 Duoplasmatron Ion Gun Manual, West Sussex, 1982.

106.　P.H. Dawson, Quadrupole Mass Spectrometry and Its Applications, Elsevier, New York, 1976.

107. R. N. S. Sodhi, The Analyst, 129 (2004) 483.

108. J.S. Ahearn, G.D. Davis, T.S. Sun, and J. D. Venables, in: K.L. Mittal, Ed., Adhesion Aspects of Polymeric Coatings, Plenum Press, New York, 1983, p.281.

109. J. D Venables, D.K. McNamara, J. M. Chen. T.S. Sun and R. L Hopping, Appl. Surf. Sci. 3 (1979) 88.

110. M. L. Abel, R. P. Digby, I. W. Fletcher, J. F. Watts, Surf. Interface Anal. 29 (2000) 115.

111. M. Teo, J. Kim. P.C. Wong, K.C. Wong, K.A.R. Mitchell, Appl. Surf. Sci. 221 (2004) 340.

112. M. Teo, J. Kim, P.C. Wong, K.C. Wong, K.A.R. Mitchell, Appl. Surf. Sci. 252 (2005) 1293.

113. N.J. Havercroft, P.M.A. Sherwood, Surf. Interface. Anal. 29 (2000) 232.

114. G. Ertas, S. Suzer, Surf. Interface. Anal. 36 (2004) 619.

115. P.C. Wong, Y.S. Li, M.Y. Zhou, K.A.R. Mitchell, Appl. Surf. Sci. 89 (1995) 261.

116. Y.S. Li, P.C. Wong, K.A.R. Mitchell, Appl. Surf. Sci. 89 (1995) 263.

117. Y.S. Li., K.C. Wong, P.C.Wong, K.A.R. Mitchell, Appl. Surf. Sci. 103 (1996) 389.

118. A. Nylund, I. Olefjord, Surf. Interface. Anal. 21 (1994) 283.

119. I. Olefjord, A. Nylund, Surf. Interface. Anal. 21 (1994) 290.

120. C. Chen, S.J. Splinter, T. Do, N.S. McIntyre, Surf. Sci. 382 (1997) L652.

121. M.R. Alexander, G. Beamson, P. Bailey, T.C.Q. Noakes, P. Skeldon, G.E. Thompson, Surf. Interface Anal. 35 (2003) 649.

122. E. McCafferty, J.P. Wightman, Surf. Interface Anal. 26 (1998) 549.

123. J. van den Brand, W.G. Sloof, H. Terryn, J.H.W. de Wit, Surf. Interface. Anal. 36 (2004) 81.

124. M.R. Alexander, G.E. Thompson, X. Zhu, G. Beamson, N. Fairley, Surf. Interface Anal. 34 (2002) 485.

125. B.V. Crist, Handbook of Monochromatic XPS Spectra Series, Vol.1, The Elements and Native Oxides, XPS International, Inc., Kawasaki, 1999.

126. T.L. Barr, J. Phys. Chem. 82 (1978) 1801.

127. L.S. Dake, D.E. King, A.W. Czanderna, Solid State Sci. 2 (2000) 781.

128. N.S. McIntyre, M.G. Cook, J. Anal. Chem. 47 (1975) 2208.

129. A.M. Beccaria, G. Poggi, G. Castello, Br. Corros. J. 30 (1995) 283.

130. B. Stypula, J. Stoch, Corros. Sci. 36 (1994) 2159.

131. B.R. Strohmeier, Surf. Sci. Spectra 3 (1995) 135.

132. J.A. Rotole, P.M.A. Sherwood, Surf. Sci. Spectra 5 (1998) 25.

133. P.M.A. Sherwood, Surf. Sci. Spectra 5 (1998) 1.

134. J.A. Rotole, P.M.A. Sherwood, J. Vac. Sci. Technol. A. 17 (1999) 1091.

135. J.A. Rotole, P.M.A. Sherwood, Surf. Sci. Spectra 5 (1998) 18.

136. O. Bose, E. Kemnitz, A. Lippitz, W.E.S. Unger, Fresenius J. Anal. Chem. 358 (1997) 175.

137. R.P. Digby, S.J. Shaw, Int. J. Adhes. Adhes. 18 (1998) 261.

138. H. Kollek, Int. J. Adhes. Adhes. 5 (1985) 75.

139. M. Gao, C.R. Feng, R. P. Wei, Metall. Mater. Trans. A, 29A (1998) 1145.

140. E. Adam, VG Scientific XPS and AUGER Handbook, West Sussex, England, 1989.

141. H. Habazaki, K. Shimizu, P. Skeldon, G.E. Thompson, G.C. Wood, X. Zhou, Trans. IMF 95 (1997) 18.

142. F.J. Boerio, C.A. Gosselin, J.W. Williams, R.G. Dillingham, J.M. Burkstrand, in: H. Ishida, G. Kumar (Eds.), Molecular Characterization of Composite Interfaces, Plenum Press, New York, 1985, p. 171.

143. F. Kotter and A. Benninghoven, Appl. Surf. Sci. 133 (1998) 47.

144. J.C. Fuggle, L.M. Watson, D.J. Fabian, S. Affrossman, Surf. Sci. 49 (1975) 61.

145. V. Fournier, P. Marcus, I. Olefjord, Surf. Interface Anal. 34 (2002) 494.

146. H.B. Yao, Y. Li, A.T.S. Wee, Appl. Surf. Sci. 158 (2000) 112.

147. S.J. Splinter, N.S. McIntyre, P.A.W. van der Heide, T. Do, Surf. Sci. 317 (1994) 194.

148. T. Do, S.J. Splinter, C. Chen, N.S. McIntyre, Surf. Sci. 387 (1997) 192.

149. S.J. Splinter, N.S. McIntyre, W.N. Lennard, K. Griffiths, G. Palumbo, Surf. Sci. 292 (1993) 130.

150. N.S. McIntyre, C. Chen, Corr. Sci. 40 (1998) 1697.

151. S.J. Splinter, N.S. McIntyre, Surf. Sci. 314 (1994) 157.

152. Y. Bouvier, B. Mutel, J. Grimblot, Surf. Coat. Technol. 180-181 (2004) 169.

153. Components for MBE Product Guide, EPI Chorus Corporation, Minnesota, 1993.

154. Electron Flight Simulator Software, Version 2.0, Small World, CA, 1995.